Triviality bound on lightest Higgs mass in next to minimal supersymmetric model

S R CHOUDHURY, MAMTA and SUKANTA DUTTA
Department of Physics and Astrophysics, University of Delhi, Delhi 110 007, India
E-mail: src@ducos.ernet.in; mamta@ducos.ernet.in; sukanta@ducos.ernet.in

MS received 1 April 1997; revised 18 October 1997

Abstract. We study the implication of triviality on Higgs sector in next to minimal supersymmetric model (NMSSM) using variational field theory. It is shown that the mass of the lightest Higgs boson in NMSSM has an upper bound $\sim 10 M_{\mathrm{W}}$ which is of the same order as that in the standard model.

Keywords. Higgs; NMSSM; triviality; variational

PACS Nos 14.80; 11.15; 12.60; 11.30

1. Introduction

It is now widely believed that the ϕ^4-scalar theory in four space-time dimensions is trivial. Consider the Lagrangian density

$$\mathcal{L} = \frac{1}{2}(\partial_\mu \phi)(\partial^\mu \phi) - \frac{1}{4} m_0^2 \phi^2 - \frac{1}{4!}\phi^4 \tag{1}$$

relevant to the scalar sector of standard model (SM). The evolution of the renormalized coupling constant $\lambda(M)$ at the scale M for large M, in the one loop approximation [1] is given by the equation

$$\frac{1}{\lambda(M)} = \frac{1}{\lambda(m)} - \frac{3}{16\pi^2}\ln\left(\frac{M}{m}\right), \tag{2}$$

where m is some low energy reference scale. From (2), it is clear that $\lambda(M)$ diverges at the scale $M = \Lambda_{\mathrm{L}}$, where

$$\Lambda_{\mathrm{L}} = m\exp(16\pi^2/3\lambda(m)). \tag{3}$$

This is the 'Landau catastrophe'. The occurence of Landau catastrophe at any finite energy can thus be avoided only if $\lambda(m) = 0$, which is the standard triviality scenario. One can however regard the Lagrangian (1) as an effective one; for a given $\lambda(m)$, the Lagrangian (1) then is a good description of the theory at most up to the energy scale Λ_{L} as given by (3). The coupling constant $\lambda(m)$ can be related to Higgs mass M_{H}. It is reasonable to expect that for a consistent effective theory M_{H} should not exceed the scale

R.N. 24935/73
Regd. No. KRN-A 64

Pramana journal of physics Vol. 50 (No. 3), March 1998

Contents

A computer simulation study of ionic conductivity in polymer electrolytes . . . . *Aninda Jiban Bhattacharyya, T R Middya and S Tarafdar* 205

Spectroscopic study of β-Ni(OH)$_2$ under pressure. . . . . *Chitra Murli, V Sugandhi, Nandini Garg, Surinder M Sharma and S K Sikka* 213

Studies on the electrical conductivity, optical absorption and x-ray diffraction in bismuth thin film . . . . *K Jayachandran and C S Menon* 221

Hyperfine interaction study of electric field gradient in hafnium phosphide using ^{181}Ta probe . . . . *Vivek Mandot, S N A Jaaffrey, S S Sharma and J Varma* 227

Mean lifetime measurements of F II and F III levels using beam-foil technique . . . . *B N Raja Sekhar, S Padmanabhan, Aparna Shastri, P Meenakshi Raja Rao, M B Kurup and K G Prasad* 231

Third harmonic generation in layered media in presence of optical bistability of the fundamental . . . . *Jolly Jose and S Dutta Gupta* 239

Generation of squeezed atomic states in cavity QED. . . . . *Aditi Ray and R R Puri* 253

Brief Report

Proton NMR in CeNiInH$_{0.53}$ down to liquid helium temperature . . . . *R Ray, A Ghoshray, K Ghoshray and N Chatterjee* 263

Indexed in CURRENT CONTENTS ISSN 0304–428

Edited and published by N Mukunda for the Indian Academy of Sciences, Bangalore 560 080.
Typeset and printed at Thomson Press (I) Ltd., Faridabad 121 007.

Editor

R Nityananda
Raman Research Institute, Bangalore

Associate Editor

H R Krishnamurthy
Indian Institute of Science, Bangalore

Editorial Board

G S Agarwal, *Physical Research Laboratory, Ahmedabad*
V Balakrishnan, *Indian Institute of Technology, Chennai*
J K Bhattacharjee, *Indian Assoc. for the Cultivation of Science, Calcutta*
D N Bose, *Indian Institute of Technology, Kharagpur*
B M Deb, *Panjab University, Chandigarh*
Rohini M Godbole, *Indian Institute of Science, Bangalore*
S Kailas, *Bhabha Atomic Research Centre, Mumbai*
R K Kaul, *The Institute of Mathematical Sciences, Chennai*
A V Khare, *Institute of Physics, Bhubaneswar*
T Padmanabhan, *Inter-Univ. Centre for Astronomy and Astrophysics, Pune*
R Ramaswamy, *Jawaharlal Nehru University, New Delhi*
A K Raychaudhuri, *National Physical Laboratory, New Delhi*
K C Rustagi, *Centre for Advanced Technology, Indore*
E V Sampathkumaran, *Tata Institute of Fundamental Research, Mumbai*
Abhijit Sen, *Institute for Plasma Research, Gandhinagar*
S K Sikka, *Bhabha Atomic Research Centre, Mumbai*
Y Singh, *Banaras Hindu University, Varanasi*

Editor of Publications of the Academy

N Mukunda
Indian Institute of Science, Bangalore

Annual Subscription Rates

All countries except India (Price includes AIR MAIL charges)	US$ 200
India	Rs. 200

Annual subscriptions for individuals for India and abroad are Rs. 100/- and $50 respectively.

All correspondence regarding subscription should be addressed to the Circulation Department of the Academy

---

Editorial Office

Indian Academy of Sciences, C V Raman Avenue,
P.B. No. 8005, Bangalore 560 080, India

Telephone: 334 2546
Telefax: 91-80-334 6094

Email: pramana@ias.ernet.in

© 1998 by the Indian Academy of Sciences. All rights reserved.

“Information for contributors” is printed in the last issue of every volume.

PRAMANA
—journal of
physics

© Printed in India

Vol. 50, No. 2,
February 1998
pp. 95–103

Relativistic fluid sphere on pseudo-spheroidal space-time

RAMESH TIKEKAR and V O THOMAS*
Department of Mathematics, Sardar Patel University, Vallabh Vidyanagar 388 120, India
* Department of Mathematics, The Faculty of Science, The Maharaja Sayajirao University of Baroda, Baroda 390 002, India

MS received 13 June 1996; revised 15 January 1998

Abstract. A new exact closed form solution of Einstein's field equations is reported describing the space-time in the interior of a fluid sphere in equilibrium. The physical 3-space, $t =$ constant of its space-time has the geometry of a 3-pseudo spheroid. The suitability of this solution for describing the model of a relativistic superdense star is discussed and the stability of the model under radial pulsations is examined.

Keywords. General relativity; static fluid sphere; superdense stars.

PACS No. 04.20

1. Introduction

The non-linear nature of the Einstein's field equations is a consequence of the self-interaction of the gravitational field. This makes it difficult to obtain relativistic models of spherical stars based on exact solution of Einstein's field equations describing spherical distributions of matter. The actual properties in the central region of a relativistic compact star are not precisely known and so assumptions of general nature to obtain exact solutions of Einstein's field equations become necessary. It is desired that solutions should be physically plausible and at the same time simple in form. This problem has been considered by several authors [1–6].

Here we have investigated the gravitational significance of space-times whose physical space obtained as $t =$ constant section has the geometry of 3-pseudo spheroid and it is shown that it can describe spherical compact distributions of matter. The form of the space-time metric and its general features are discussed in § 2. It is shown that the geometry of the space-time is governed by two parameters R and K. The space-time metric corresponding to a new exact closed form solution of Einstein's field equations is written in § 3. The suitability of this solution for describing the model of a superdense star is explored following the approach of [4, 5, 9] in the subsequent sections.

2. Static pseudo spheroidal space-time

$$d\sigma^2 = dx^2 + dy^2 + dz^2 + dw^2, \tag{1}$$

will have the cartesian equation

$$\frac{w^2}{b^2} - \frac{x^2 + y^2 + z^2}{R^2} = 1, \tag{2}$$

where b and R are constants. The section $w =$ constant of the 3-pseudo spheroid are pseudo spheres, while sections $x =$ constant, $y =$ constant and $z =$ constant represent, respectively hyperboloids of two sheets.

The parametrization

$$x = r\sin\theta\cos\phi, \quad y = r\sin\theta\sin\phi, \quad z = r\cos\theta, \quad w = b(1 + r^2/R^2)^{1/2} \tag{3}$$

of the 3-pseudo spheroid leads to

$$d\sigma^2 = \frac{1 + Kr^2/R^2}{1 + r^2/R^2}\, dr^2 + r^2(d\theta^2 + \sin^2\theta d\phi^2), \tag{4}$$

where

$$K = 1 + b^2/R^2. \tag{5}$$

The pseudo spheroidal 3-space given by eq. (4) is spherically symmetric and regular for $K > 1$. It is flat when $K = 1$ and generates into open hyperboloid when $K = 0$.

Following the Vaidya–Tikekar [4] approach we consider the space-time with metric

$$ds^2 = e^{\nu(r)}dt^2 - \frac{1 + Kr^2/R^2}{1 + r^2/R^2}\, dr^2 - r^2(d\theta^2 + \sin^2\theta d\phi^2). \tag{6}$$

Various aspects of spherical distributions of perfect fluid in equilibrium described by space-times with metric in a form similar to (6) have been investigated by Buchdahl [1]. Vaidya and Tikekar [4] have examined the geometrical features of the 3-dimensional physical spaces obtained as $t =$ constant hypersurfaces of such space-times. The space-time of the specific solution discussed by Buchdahl has the geometry of a 3-spheroid immersed in a 4-dimensional Euclidean space of Vaidya–Tikekar type. An extensive study of such solutions has also been done by Maharaj and Leach [6]. The 3-space of the metric (6) is characterized by pseudo spheroidal geometry and therefore the specific class of solutions in this set up is clearly distinct from the specific class of solutions reported by Buchdahl, Vaidya and Tikekar [4] and Maharaj and Leach [6].

3. Matter distribution on pseudo spheroidal space-time

In this section the gravitational significance of a static, spherical distribution of matter in the form of perfect fluid is explored on the background of the space-time of the metirc (6) with energy-momentum tensor

$$T_{ij} = (\rho + p/c^2)u_i u_j - (p/c^2)g_{ij}. \tag{7}$$

Here ρ, p and u^i respectively denote the matter density, fluid pressure and the unit 4-velocity field of the fluid. Since the fluid distribution is at rest,

$$u^i = (0, 0, 0, e^{-\nu/2}). \tag{8}$$

Einstein's field equations

$$\mathcal{R}_{ij} - \frac{1}{2}\mathcal{R}g_{ij} = -\frac{8\pi G}{c^2}T_{ij} \tag{9}$$

for a specific choice of the curvature parameter $K = 2$ leads to the space-time metric written explicitly as

$$\begin{aligned} \mathrm{d}s^2 = &\left[A\sqrt{1 + r^2/R^2} + B\left(X(r) - \frac{1}{\sqrt{2}}\sqrt{1 + 2r^2/R^2}\right)\right]^2 \mathrm{d}t^2 \\ &- \frac{1 + 2r^2/R^2}{1 + r^2/R^2}\,\mathrm{d}r^2 - r^2(\mathrm{d}\theta^2 + \sin^2\theta\mathrm{d}\phi^2), \end{aligned} \tag{10}$$

where

$$X(r) = \sqrt{1 + r^2/R^2}\,\ln[\sqrt{2}\sqrt{1 + r^2/R^2} + \sqrt{1 + 2r^2/R^2}\,] \tag{11}$$

and A, B are arbitrary constants.

The matter density and fluid pressure for the distribution (10) are expressed as

$$\frac{8\pi G}{c^2}\rho = \frac{3}{R^2}\left(1 + \frac{2r^2}{3R^2}\right)\left(1 + \frac{2r^2}{R^2}\right)^{-2}, \tag{12}$$

$$\frac{8\pi G}{c^4}p = \frac{A\sqrt{1 + r^2/R^2} + B[X(r) + (1/\sqrt{2})\sqrt{1 + 2r^2/R^2}]}{R^2(1 + 2r^2/R^2)(A\sqrt{1 + r^2/R^2} + B[X(r) - (1/\sqrt{2})\sqrt{1 + 2r^2/R^2}])}. \tag{13}$$

It is evident from eq. (12) that density is positive throughout the distribution. The gradient of density $\mathrm{d}\rho/\mathrm{d}r$ is found to be negative indicating that ρ is decreasing radially outward.

4. Size of the fluid sphere

The total mass and size of the configuration can be estimated using the scheme given by Vaidya and Tikekar [4], as follows.

Equation (12) determine ρ at the boundary $r = a$ of the distribution as

$$\frac{8\pi G}{c^2}\rho(a) = \frac{3(1 + 2a^2/3R^2)}{R^2(1 + 2a^2/R^2)^2}. \tag{14}$$

We introduce the density variation parameter

$$\lambda = \frac{\rho(a)}{\rho(0)} = \frac{1 + 2a^2/3R^2}{(1 + 2a^2/R^2)^2}, \tag{15}$$

where $\rho(0)$ is the density at the centre. Since ρ is a decreasing function of $r, \lambda < 1$. Solving (15) as quadratic in (a^2/R^2) one finds

$$\frac{a^2}{R^2} = \frac{1 - 6\lambda + \sqrt{1 + 24\lambda}}{12\lambda}. \tag{16}$$

The algebraic root assigning negative values to a^2/R^2 is rejected to ensure that a/R is real.

Equation (12) implies that the matter density at the centre is explicitly related with curvature parameter R as

$$\frac{8\pi G}{c^2}\rho(0) = \frac{3}{R^2}. \tag{17}$$

Equation (17) therefore determines R in terms of $\rho(a)$ and λ. Equation (16) then determines the boundary radius a of the distribution. Thus the size of the configuration is determined in terms of the surface density $\rho(a)$ and density variation parameter λ.

5. Physical plausibility

Any physically acceptable solution must comply with the following conditions:

(i) The matter density ρ and fluid pressure p should be non-negative throughout the distribution.

(ii) The gradients $\mathrm{d}\rho/\mathrm{d}r$ and $\mathrm{d}p/\mathrm{d}r$ should be negative.

(iii) The speed of sound should not exceed the speed of light as implication of causality fulfillment.

(iv) The interior metric should match continuously with the Schwarzschild exterior solution

$$\mathrm{d}s^2 = \left(1 - \frac{2m}{r}\right)\mathrm{d}t^2 - \left(1 - \frac{2m}{r}\right)^{-1}\mathrm{d}r^2 - r^2(\mathrm{d}\theta^2 + \sin^2\theta\mathrm{d}\phi^2) \tag{18}$$

at the boundary surface $r = a$ of the distribution where $p(a) = 0$.

The continuity of the metric coefficients give

$$m = \frac{a^3}{2R^2(1 + 2a^2/R^2)} \tag{19}$$

and

$$\sqrt{1 - 2m/a} = A\sqrt{1 + a^2/R^2} + B\left(X(a) - (1/\sqrt{2})\sqrt{1 + 2a^2/R^2}\right), \tag{20}$$

where

$$X(a) = \sqrt{1 + a^2/R^2}\ln(\sqrt{2}\sqrt{1 + a^2/R^2} + \sqrt{1 + 2a^2/R^2}). \tag{21}$$

The continuity of pressure across $r = a$ requires that pressure to vanish on the boundary implying that

$$A\sqrt{1 + a^2/R^2} = -B(X(a) + (1/\sqrt{2})\sqrt{1 + 2a^2/R^2}). \tag{22}$$

The constants A and B are determined from eqs (19), (20) and (22) as

$$A = \frac{X(a) + (1/\sqrt{2})\sqrt{1 + 2a^2/R^2}}{\sqrt{2}(1 + 2a^2/R^2)}, \tag{23}$$

$$B = -\frac{\sqrt{1 + a^2/R^2}}{\sqrt{2}(1 + 2a^2/R^2)}, \tag{24}$$

while the total mass m is determined by (19).

The expressions (23) and (24) for A and B when substituted in (13), one can find after a lengthy but straightforward computation that $p \geq 0$ throughout the sphere. Further using the TOV equation we found that the pressure is decreasing radially outward.

Using the expressions (12) and (13) for density and pressure and the values of A and B in the TOV equation it can be readily seen that the speed of sound will not exceed the speed of light in the central region and boundary of the distribution, ensuring the fulfilment of causality requirements.

The expression for $\mathrm{d}p/\mathrm{d}\rho$, which represents the speed of sound in isentropic fluids, takes the form

$$\frac{\mathrm{d}p}{\mathrm{d}\rho} = \frac{\pi G R^2 (\rho + p/c^2)(1 + 2r^2/R^2)^3 \, [1 + (8\pi G R^2 p/c^4)(1 + 2r^2/R^2)]}{(5 + 2r^2/R^2)(1 + r^2/R^2)}. \tag{25}$$

At the centre, $\mathrm{d}p/\mathrm{d}\rho$ has the value

$$\left(\frac{\mathrm{d}p}{\mathrm{d}\rho}\right)_0 = \frac{\pi G R^2 [\rho(0) + p(0)/c^2](1 + 8\pi G p(0) R^2/c^4)}{5}. \tag{26}$$

From eqs (12), (13), (23) and (24) we can show that

$$\rho(0) - 3p(0)/c^2 > 0 \tag{27}$$

at the centre and using (17) and (27) it readily follows from (26) that

$$\left(\frac{\mathrm{d}p}{\mathrm{d}\rho}\right)_0 < 0.2c^2. \tag{28}$$

At the boundary, using (14), we have the expression

$$\left(\frac{\mathrm{d}p}{\mathrm{d}\rho}\right)_s = \frac{3(1 + 2a^2/R^2)(1 + 2a^2/3R^2)}{8(5 + 2a^2/R^2)(1 + a^2/R^2)} c^2 < c^2. \tag{29}$$

The variation of $\mathrm{d}p/\mathrm{d}\rho$, which represents the speed of sound in isentropic fluids, is examined using numerical procedures for certain specific models in this set up. It is found that p/ρ is decreasing radially outward indicating that $\mathrm{d}(p/\rho)/\mathrm{d}\rho > 0$. However the speed of sound is found to be increasing radially outward for a number of models, which is an unsatisfactory feature of these solutions in view of the expectation that it should be decreasing radially outward which follows from equations of state found in literature. Since definite information about the equation of state for matter in nuclear density ranges is lacking, as argued by Knutsen [9], one must be careful in this respect.

6. Superdense star model

When all thermonuclear sources of energy are exhausted, a star will gradually cool down and in this process it will collapse gravitationally and form a compact star – white dwarf,

Table 1. Masses and equilibrium radii of superdense star models corresponding to $K = 2$ and $\rho(a) = 2 \times 10^{14}$ gm/cm^3.

λ	R (km)	a (km)	m (km)	m/Mo	A	B
0.900	26.928	04.875	0.075	0.050	1.094	−0.674
0.800	25.388	06.828	0.215	0.146	1.062	−0.639
0.700	23.748	08.271	0.403	0.273	1.027	−0.602
0.600	21.987	09.429	0.634	0.429	0.987	−0.562
0.500	20.071	10.382	0.904	0.613	0.943	−0.518
0.400	17.952	11.162	1.216	0.825	0.890	−0.469
0.300	15.547	11.771	1.571	1.065	0.826	−0.413
0.200	12.694	12.176	1.972	1.337	0.742	−0.345
0.125	10.035	12.291	2.304	1.562	0.653	−0.279
0.100	08.976	12.274	2.421	1.641	0.613	−0.252

Note: 1 Mo = 1.475 km.

neutron star, or black hole. Generally a star keeps its equilibrium with outward pressure against the self gravitational force. The model that we have presented here can describe the hydrostatic equilibrium conditions in such a superdense star with densities in the range 10^{14}–10^{16} gm/cm^3. We take the matter density on the boundary $r = a$ of the star as $\rho(a) = 2 \times 10^{14}$ gm/cm^3. Choosing different values for λ, we determine the boundary radius a of the star and its total mass m in accordance with the scheme of § 4 and § 5. The value of m obtained is in kilometers. The mass of the star in grams is obtained using $M = mc^2/G$. The results of these computations together with the values of constants A and B as determined by eqs (23) and (24) are given in table 1.

For $\lambda \leq 0.7$ in table 1, we get a set of physically viable models of relativistic compact stars. The models with $\lambda > 0.7$ in the table have their equilibrium radii much smaller than that of a neutron star. The equilibrium models presented here take lesser values for radii a and total mass m, than the corresponding values given by Vaidya and Tikekar [4].

7. Dynamic stability

A sufficient condition for the dynamic stability of a spherically symmetric distribution of matter under small radial adiabatic perturbations has been developed by Chandrasekhar [7]. A normal mode of radial oscillation for an equilibrium configuration i.e.

$$\delta r = \xi(r) \exp(i\omega t) \tag{30}$$

is stable when the frequency of oscillation ω is real and unstable when ω is imaginary.

Chandrasekhar's [7] pulsation equation for the line element (6) is given by

$$\begin{aligned} &\omega^2 \int_{\text{centre}}^{\text{boundary}} \exp\left(\frac{3\alpha + \nu}{2}\right) \frac{(\rho + p)u^2}{r^2}\, \mathrm{d}r \\ &= \int_{\text{centre}}^{\text{boundary}} \exp\left(\frac{3\nu + \alpha}{2}\right) \left(\frac{\rho + p}{r^2}\right) \\ &\quad \times \left\{ \left[\frac{-2}{r} \frac{\mathrm{d}\nu}{\mathrm{d}r} - \frac{1}{4} \left(\frac{\mathrm{d}\nu}{\mathrm{d}r}\right)^2 + 8\pi p\, \mathrm{e}^{\alpha} \right] u^2 + \frac{\mathrm{d}p}{\mathrm{d}\rho} \left(\frac{\mathrm{d}u}{\mathrm{d}r}\right)^2 \right\} \mathrm{d}r, \end{aligned} \tag{31}$$

where

$$u = \xi r^2 \mathrm{e}^{-\nu/2} \quad \text{and } \mathrm{e}^{\alpha} = \frac{1 + 2r^2/R^2}{1 + r^2/R^2} \quad \text{with } K = 2. \tag{32}$$

The boundary condition to be satisfied at $r = a$ is that the Lagrangian change in pressure

$$\Delta p = -\mathrm{e}^{\nu/2}\left(\frac{\gamma p}{r^2}\right)\left(\frac{\mathrm{d}u}{\mathrm{d}r}\right) = 0 \quad \text{at } r = a,$$

where γ is the adiabatic index. We must have

$$\frac{\mathrm{d}u}{\mathrm{d}r} = 0 \quad \text{at } r = a. \tag{33}$$

Following the method of Bardeen *et al* [8] and used by Knutsen [9] to investigate the stability of Vaidya–Tikekar models, we choose

$$u = R^3 x^{3/2}(1 + a_1 x + b_1 x^2 + \cdots) \tag{34}$$

as the trial function where the new variable x is taken as $x = 2r^2/R^2$.

The boundary condition $\mathrm{d}u/\mathrm{d}r = 0$ at $r = a$ implies

$$3 + 5a_1 b + 7b_1 b^2 + \cdots = 0, \tag{35}$$

where $b = 2a^2/R^2$.

The pulsation equation (31) for the metric (6) now takes the form

$$\omega^2 \int_{\text{centre}}^{\text{boundary}} \exp\left(\frac{3\alpha+\nu}{2}\right)\frac{(\rho+p)u^2}{r^2}\,\mathrm{d}r = \int_0^b R_1 R_2((R_3+R_4+R_5)R_6+R_7R_8)\mathrm{d}x, \tag{36}$$

where

$$R_1 = \frac{2(x+1)}{\sqrt{x+2}}\left(A_1\sqrt{x+2} + B_1[\sqrt{x+2}\,l(x) - \sqrt{x+1}]\right)^3,$$

$$R_2 = \frac{L(x)(x+2) + p(x)(x+2) + q(x)}{4\pi R^2 (x+1)^2 [L(x) + p(x) + q(x)]},$$

$$R_3 = \frac{-8[L(x) + p(x)]}{R^2(x+2)[L(x) + p(x) + q(x)]},$$

$$R_4 = \frac{-2x[L(x) + p(x)]^2}{R^2(x+2)^2[L(x) + p(x) + q(x)]^2},$$

$$R_5 = \frac{2(x+1)[L(x) + p(x) - q(x)]}{R^2(x+1)(x+2)[L(x) + p(x) + q(x)]},$$

$$R_6 = 2R^4 x^2(1 + a_1 x + b_1 x^2 + \cdots)^2,$$

$$R_7 = \frac{(x+1)[L(x) + p(x)][L(x)(x+2) + p(x)(x+2) + q(x)]}{(x+5)(x+2)[L(x) + p(x) + q(x)]^2},$$

Table 2. The values of the integral on the right hand side of the pulsation equation (36) for some specific choices of the constants a_1 and b_1 and $\lambda = 0.4$.

a_1	b_1	Integral
0.000	−0.717	1.476
−0.776	0.000	0.536
−0.858	1.000	0.084
1.000	−1.641	3.447
5.000×10^2	-4.627×10^2	1.076×10^5
-5.410×10^2	5.000×10^2	1.246×10^5
1.000×10^5	-9.240×10^4	4.272×10^9
-1.000×10^5	9.240×10^4	4.272×10^9

$$\begin{aligned}
R_8 &= 4R^2x(3 + 5a_1x + 7b_1x^2 + \cdots)^2, \\
L(x) &= r(x)[l(b) - l(x)], \\
l(x) &= \ln[\sqrt{x+1} + \sqrt{x+2}], \\
l(b) &= \ln[\sqrt{b+1} + \sqrt{b+2}], \\
p(x) &= \sqrt{x+2}\,\sqrt{b+1}, \\
q(x) &= \sqrt{x+1}\,\sqrt{b+2}, \\
r(x) &= \sqrt{x+2}\,\sqrt{b+2}, \\
A_1 &= \frac{\sqrt{b+2}\,l(b) + \sqrt{b+1}}{b+1}, \\
B_1 &= -\frac{\sqrt{b+2}}{(b+1)}.
\end{aligned}$$

We have evaluated the integral on the right of the equation (36) numerically for different values of b. It is found that the integral admits positive values for $0.243 \leq b \leq 1.146$ (i.e. $0.3 \leq \lambda \leq 0.7$) and for different choices small, large, postive or negative values of the constants a_1, b_1.

We have reported in table 2 the values of the integral on the right side of the equation (36) evaluated numerically for certain specific choices of a_1 and b_1 for the model with $\lambda = 0.4$ of table 1.

This analysis indicates that these models with $0.3 \leq \lambda \leq 0.7$ will be stable. The space-time with pseudo spheroidal geometry for its spatial sections $t =$ constant thus may admit the possibilities of describing interiors of superdense fluid stars in equilibrium.

Acknowledgements

The authors express their sincere thanks to the referee for valuable suggestions and to the Director, IUCAA for the facilities provided to them for this work.

References

[1] H A Buchdahl, *Phys. Rev.* **116**, 1027 (1959)
[2] R J Adler, *J. Math. Phys.* **15**, 727 (1974)
[3] C Leibovitz, *Phys. Rev.* **185**, 1664 (1969)
[4] P C Vaidya and R Tikekar, *J. Astrophys. Astron.* **3**, 325 (1982)
[5] R Tikekar, *J. Math. Phys.* **31**, 2454 (1990)
[6] S D Maharaj and P G L Leach, *J. Math. Phys.* **37**, 430 (1996)
[7] S Chandrasekhar, *Astrophys. J.* **140**, 417 (1964)
[8] J M Bardeen, K S Thorne and D W Meltzer, *Astrophys. J.* **145**, 505 (1966)
[9] H Knutsen, *Mon. Not. R. Astron. Soc.* **232**, 163 (1988)

PRAMANA
—journal of
physics

© Printed in India

Vol. 50, No. 2,
February 1998
pp. 105–108

Causal dissipation in Robertson–Walker cosmological models

J P SINGH, A PRASAD and R K TIWARI
Department of Maths and Statistics, A.P.S. University, Rewa 486 003, India

MS received 28 July 1997; revised 16 December 1997

Abstract. Some of the Robertson–Walker cosmological models filled with a fluid with bulk viscosity have been derived which are consistent with causal thermodynamics. The models are discussed briefly.

Keywords. FRW models; viscous dissipation; cosmology; extended irreversible thermodynamics.

PACS No. 98.80

1. Introduction

Introduction of viscosity into the material content of model universes is gaining importance [1]. This is in the hope of having realistic description of the real universe mainly during the early stages of its evolution. Several workers have considered viscous fluid but only a few of them have tried to make it thermodynamically consistent. Thermodynamical consistency of the viscous fluid is undoubtedly essential as it leads to more realistic description. Moreover, if this consistency occurs in a way which allows the dissipation of viscosity causally, the reality of description is further enhanced.

Initial efforts to obtain the above consistency were based on inadequate theories given by Eckart [2], and Landau and Lifshitz [3] – inadequate in the sense that these (theories) allowed viscous dissipation with super luminal speeds [4, 5]. However, this drawback was later on overcome by resorting to extended irreversible thermodynamics (EIT) which provided the relativistic causality in a natural way [6, 7]. Thus the viscosity obeying EIT may be a reasonable resort.

In the frame work of standard (Robertson–Walker) cosmology, models have been derived which are causally well behaved as regards their viscous-fluid contents. Hiscock and Salmonsan [8] have considered the flat case with bulk viscosity. Zakari and Jou [9] and Maartens [10], while discussing it, have investigated the possibility of exponential inflation. Banerjee and Beesham [11] have obtained a power law solution as well. In the non-flat case we have, of course, the solution given by Mindez and Pavon [12], but in the

We consider the Robertson–Walker space-time given by

$$\mathrm{d}s^2 = -\mathrm{d}t^2 + R^2(t)[(1-kr^2)^{-1}\mathrm{d}r^2 + r^2(\mathrm{d}\theta^2 + \sin^2\theta \mathrm{d}\varphi^2)], \tag{1}$$

where $k = 0, \pm 1$ and the energy momentum tensor T_{ij} in the Einstein's field equation

$$G_{ij} = T_{ij} \quad (\text{for } 8\pi G = 1 = c) \tag{2}$$

of the form

$$T_{ij} = (\rho + p_{\mathrm{eff}})u_i u_j + p_{\mathrm{eff}}\, g_{ij}, \tag{3}$$

where $p_{\mathrm{eff}} = p + \Pi$; ρ, p, Π and u_i being respectively the energy density, equilibrium pressure, bulk viscous stress and the unit flow vector of the fluid co-moving orthogonally to the surface of homogeneity. We also consider the laws of

1. *Energy conservation*

$$T^{ij}_{;j} = 0. \tag{4}$$

2. *Number conservation*

$$N^i_{;i} = 0, \quad N^i = nu^i. \tag{5}$$

alongwith

3. *The H-theorem*

$$S^i_{;i} \geq 0. \tag{6}$$

4. *The Gibb's equation*

$$\begin{aligned} S^i &= sN^i - (\tau\Pi^2/2\xi T)u^i, \\ Tds &= \mathrm{d}(\rho/n) + pd(1/n), \end{aligned} \tag{7}$$

where s, n, $T \geq 0$, $\xi \geq 0$ and $\tau \geq 0$ are respectively the specific entropy, number density, temperature, bulk viscosity coefficient and the relaxation coefficient for bulk viscous effects. A semicolon in the above indicates covariant differentiation.

Equations (3)–(7) give rise to evolution equation [10, 11] for the bulk viscosity

$$\Pi + \tau\dot{\Pi} = -3\xi H - (\epsilon/2)\tau\Pi(3H + \dot{\tau}/\tau - \dot{\xi}/\xi - \dot{T}/T), \tag{8}$$

where

$$H = (1/3)\theta = (1/3)u^i_{;i} = \dot{R}/R,$$

θ being the expansion scalar and an overhead dot standing for differentiation with respect to time t. Equations (1)–(3) lead to

$$(\dot{R}/R)^2 + k/R^2 = \rho/3 \tag{9}$$

and

$$\ddot{R}/R = -(1/6)[\rho + 3(p + \Pi)]. \tag{10}$$

Thus we get only three independent equations (8)–(10) in seven unknowns ρ, p, Π, ξ, τ, T and R. So, as usual, we assume the following ad-hoc relations

$$p = (\gamma - 1)\rho, \quad 1 \leq \gamma \leq 2, \tag{11}$$

$$\xi = \alpha\rho^q, \quad \alpha \geq 0, \quad q \geq 0, \tag{12}$$

$$\tau = \xi/\rho, \tag{13}$$

and

$$T = \beta\rho^r, \quad \beta > 0, \quad r \geq 0. \tag{14}$$

Now with the help of (9), (10) and (11), eq. (8) can be written in the form

$$\begin{aligned}
&\tau\ddot{H} + (3/2)\tau(\epsilon + 2\gamma)H\dot{H} + \dot{H} + (1/2)\epsilon\tau(\dot{\tau}/\tau - \dot{\xi}/\xi - \dot{T}/T)\dot{H} \\
&\quad + (9/4)\epsilon\gamma\tau H^3 + (3/4)\epsilon\gamma\tau(\dot{\tau}/\tau - \dot{\xi}/\xi - \dot{T}/T)H^2 + (3/2)\gamma H^2 \\
&\quad - (3/2)\xi H + \{(3\gamma - 2)/2R^2\}\cdot k\tau \\
&\quad \times [1/\tau + (3/2)\epsilon H - 2\dot{R}/R + (\epsilon/2)(\dot{\tau}/\tau - \dot{\xi}/\xi - \dot{T}/T)] = 0.
\end{aligned} \tag{15}$$

Using (12)–(14), eq. (15) becomes

$$\begin{aligned}
&\ddot{H} + (3/2)(2\gamma + \epsilon)\dot{H}H + \alpha^{-1}[3(H^2 + k/R^2)]^{1-q} \\
&\quad \times [\dot{H} + 3\gamma H^2/2 + (k/2R^2)(3\gamma - 2)] + (9/4)\epsilon\gamma H^3 \\
&\quad + [(k/2R^2)(3\gamma - 2)(3\epsilon/2 - 2) - (9/2)(H^2 + k/R^2)]H \\
&\quad - (r + 1)\epsilon H \cdot (\dot{H} - k/R^2)/(H^2 + k/R^2) \\
&\quad \times [\dot{H} + (3/2)\gamma H^2 + (k/2R^2)(3\gamma - 2)] = 0.
\end{aligned} \tag{16}$$

A general solution of eq. (16) is difficult to obtain. However, for the case $k = 0$, Maartens [10] has obtained an exponential solution whereas Banerjee and Beesham [11] have derived a power law solution. We notice in the present paper that $R = t$ with $q = 1/2$ is also a solution provided:

(i) *For* $k = 1$:

$$\alpha = \begin{cases} \sqrt{6}(3\gamma - 2)/(5 + 6\gamma) > 0 & \text{when } \epsilon = 0 \\ 2\sqrt{6}(3\gamma - 2)/4(5 + r) - 3\gamma(1 + 2r) > 0, & \\ \quad 0 < r < (20 - 3\gamma)/2(3\gamma - 2) & \text{when } \epsilon = 1. \end{cases}$$

(ii) *For* $k = 0$:

$$\alpha = \begin{cases} \sqrt{3}(3\gamma - 2)/(5 + 6\gamma) > 0 & \text{when } \epsilon = 0 \\ 2\sqrt{3}(3\gamma - 2)/4(5 + r) - 3\gamma(1 + 2r) > 0, & \\ \quad 0 < r < (20 - 3\gamma)/2(3\gamma - 2) & \text{when } \epsilon = 1. \end{cases}$$

3. Discussion

For $k = -1$, the solution $R = t$, holds identically, though eq. (16) is not the proper way to go through in this case. Actually, in this case, $\rho = 0 = p$. Thus no matter exists and the universe is empty. Thus $R = t$ is inconsistent when $k = -1$.

When $k = 1$, we obtain for the solutions corresponding to both the truncated ($\epsilon = 0$) and full ($\epsilon = 1$) theories the following expressions for concerned quantities:

$$\rho = 6/t^2, \quad p = 6(\gamma - 1)/t^2, \quad \Pi = 2(2 - 3\gamma)/t^2,$$
$$\xi = \alpha\sqrt{6}/t, \quad \tau = (\alpha/\sqrt{6})t, \quad T = 6^r\beta t^{-2r}.$$

Clearly, for $t > 0$, each of the quantities ρ, p, ξ, τ and T is positive, while Π is negative. Moreover, both ρ and p tend to ∞ as $t \to 0$, and they tend to 0 as $t \to \infty$. Also $\theta = 3/t \to \infty$ and 0 respectively when $t \to 0$ and ∞. Thus the model starts with a big bang at $t = 0$ and its rate of expansion vanishes asymptotically. The temperature decreases gradually to zero when the expansion stops. We observe that $-\Pi = p + \rho/3$ which restricts the model to be inflationary (actually, the condition for inflation $\ddot{R} > 0$ requires, by virtue of (10), that $-p_{\rm eff} > \rho/3$). The behaviour of the models are similar to that corresponding to the solutions for $k = 0$, in which case the expressions for various quantities differ slightly by some positive constants only. The solutions for $k = 0$, form the particular cases of that obtained by Banerjee and Beesham [11].

References

[1] D Jou, J Casas-Vazquez and G Lebon, *Extended irreversible thermodynamics* (Springer-Verlag, Berlin, 1993)

[2] C Eckart, *Phys. Rev.* **58**, 919 (1940)

[3] L Landau and E M Lifshitz, *Fluid mechanics* (Addison-Wesley, Reading, MA, 1958), Sec. 127

[4] W A Hiscock and L Lindbolm, *Phys. Rev.* **D31**, 725 (1985)

[5] W A Hiscock and L Lindbolm, *Phys. Rev.* **D35**, 3723 (1987)

[6] W A Hiscock and L Lindbolm, *Ann. Phys. (NY)* **151**, 466 (1983)

[7] W A Hiscock and L Lindbolm, *Contemp. Math.* **71**, 181 (1988)

[8] W A Hiscock and J Salmonsan, *Phys. Rev.* **D43**, 3249 (1991)

[9] M Zakari and D Jou, *Phys. Rev.* **D48**, 1597 (1993)

[10] R Maartens, *Class. Quantum Gravit.* **12**, 1455 (1995)

[11] N Banerjee and A Beesham, *Pramana – J. Phys.* **46**, 213 (1996)

[12] V Mindez and D Pavon, *Mon. Not. R. Astron. Soc.* **282**, 753 (1996)

PRAMANA
—journal of
physics

© Printed in India

Vol. 50, No. 2,
February 1998
pp. 109–131

Particle production in curved spacetime

N G SARKAR and S BISWAS
Department of Physics, University of Kalyani, Kalyani 741 235, India
Email: sbiswas@klyuniv.ernet.in

MS received 2 May 1997; revised 22 September 1997

Abstract. Particle production in curved spacetime has been discussed through the method of complex time WKB approximation. We consider Dirac equation in non-flat spacetime to understand particle production as particle–antiparticle rotation. The method is also generalized to understand particle production through parametric resonance. To understand the method of CWKB we consider particle production in Kasner spacetime as an example.

Keywords. Particle production; Robertson–Walker spacetime; parametric resonance.

PACS Nos 03.65; 04.62; 98.80

1. Introduction

The Dirac equation in curved spacetime is of considerable interest in astrophysics and cosmology. Previous investigations in this direction are due to Fock [1], Tetrode [2], Schrödinger [3] and McVittie [4]. A general discussion of the $m = 0$ neutrino case was given by Brill and Wheeler [5].

In astrophysics and cosmology the pair creation in expanding universes has been of considerable interest for several reasons. The choice of quantum vacuum is a very delicate object in curved spacetime and it greatly affects the calculations leading to pair creation. The works in this direction are due Chimento and Mollerach [6], Audretsch and Schäfer [7], Castagnino and Mazzitelli [8], Biswas and Guha [9], Biswas *et al* [10], Guha *et al* [11] and Biswas *et al* [12]. Calculation of pair creation and others related to has also been carried by Lotze [13], Barut and Duru [14], Biswas *et al* [15], Sahni [16], Barut and Singh [17] and many others.

In astrophysics the study of Dirac equation has gained importance in strange matter calculations as well as in neutron star calculations [18], with and without magnetic field. In cosmology the effect of particle production has some physical considerations, mainly in the study of damping and avoidance of initial singularity. A study of pair creation of spin $\frac{1}{2}$ particles (massive and massless) in Robertson–Walker universes was made by Parker [19], Lotze [13] and recently by Biswas *et al* [11, 12]. In the so called back-reaction problem, the effect of particle production back on the metric has not been incorporated successfully so far. Fischetti, Hartle and Hu [20], Anderson [21] tried to solve the back-reaction problem but the effect of particle production is not directly involved in the calculations. Ford [22] tried to stress the importance of particle production in solving the back-reaction problem, but the calculations, though interesting, lack to project the dynamical evolution of spacetime that can only be solved through the solution of Einstein field equations with a term for particle production density in the right-hand side of Einstein equations.

Various authors have studied particle production both in flat or non-flat spacetime. The common method is to define in and out vacuum and find the Bogolubov coefficients. The temporal equation resulting from Dirac equation in a Robertson–Walker framework has been found to differ [16, 17]. It has therefore been necessary to restudy Dirac equation in curved spacetime and find the correct temporal equation. It should be pointed out that the form of temporal equation is crucial in determining the particle production in expanding spacetime. In our previous works we followed a different procedure to calculate the pair production amplitude both in flat or non-flat R-W spacetime. In our approach [9–12], the turning points determined from the second order temporal Dirac equation are crucial in calculating the pair production amplitude. The turning points are fixed by the temporal equation in a given spacetime. To find out the correct turning points we investigate the derivation again without taking any results from other works. In this work we find that the Dirac equation in diagonal tetrad differs significantly from that of Barut and Singh [17]. We carry out the explicit derivation and find that our calculation is consistent with Sahni [16].

The present work, though a recheck of some previous calculations, also deals with some new results e.g., use of two dimensional temporal Dirac equation to understand particle production as particle–antiparticle rotation and parametric resonance particle production as a generalization of our result.

In § 2 and § 3 we consider Dirac equation in expanding non-flat spacetime and reduce it to two dimensional form to study particle–antiparticle rotation. Section 4 deals with parametric resonance particle production and § 5 deals with particle production in Kasner spacetime. We end up with discussion in § 6.

Recently particle production has been an active area of research [23–26] in cosmology to understand reheating mechanism after inflation, and the origin of cold dark matter. The method used [23–26] is parametric resonance. Our approach is an alternative one very similar to parametric resonance particle production. It is the aim of this work to highlight our approach with some specific examples. Though much work has been done on particle production, the present attempt sees the subject from a different approach with applicability in other directions.

2. The Dirac equation in expanding non-flat spacetime

The Dirac equation in curved spacetime is

$$\left[i\gamma^{\mu}(x)\frac{\partial}{\partial x^{\mu}} - i\gamma^{\mu}(x)\Gamma_{\mu}(x)\right]\psi = m\psi. \tag{1}$$

Here $\gamma^{\mu}(x)$ are curvature dependent Dirac matrices, $\Gamma_{\mu}(x)$ the spin connections and m the mass of the particle.

2.1 *The metric*

We start with Robertson–Walker type metric that describes a homogeneous isotropic non-flat universe given by

$$ds^2 = dt^2 - a^2(t)\left[\frac{dr^2}{1-kr^2} + r^2 d\theta^2 + r^2\sin^2\theta d\varphi^2\right],$$

where $k = +1, 0, -1$, and for $k = 0$ this metric reduces to the conformally flat case. order to understand the difference with flat-space equation we convert eq. (2) using

$$\begin{pmatrix} dr \\ d\theta \\ d\varphi \end{pmatrix} = \begin{pmatrix} \sin\theta\cos\varphi & \sin\theta\sin\varphi & \cos\theta \\ \frac{\cos\theta\cos\varphi}{r} & \frac{\cos\theta\sin\varphi}{r} & -\frac{\sin\theta}{r} \\ -\frac{\sin\varphi}{r\sin\theta} & \frac{\cos\varphi}{r\sin\theta} & 0 \end{pmatrix} \begin{pmatrix} dx_1 \\ dx_2 \\ dx_3 \end{pmatrix},$$

to the form

$$\begin{aligned} ds^2 = dt^2 - a^2(t)\Bigg[&\frac{1-k(x_2^2+x_3^2)}{\rho^2}dx_1^2 + \frac{1-k(x_1^2+x_3^2)}{\rho^2}dx_2^2 + \frac{1-k(x_1^2+x_2^2)}{\rho^2}\mathrm{d} \\ &+ \frac{2kx_1x_2}{\rho^2}dx_1dx_2 + \frac{2kx_1x_3}{\rho^2}dx_1dx_3 + \frac{2kx_2x_3}{\rho^2}dx_2dx_3\Bigg] \\ = g_{\mu\nu}dx^\mu dx^\nu&, \end{aligned}$$

with $\rho^2 = 1 - kr^2$ and

$$g_{\mu\nu} = \begin{pmatrix} 1 & 0 & 0 & 0 \\ 0 & -a^2\frac{1-k(x_2^2+x_3^2)}{\rho^2} & -a^2\frac{kx_1x_2}{\rho^2} & -a^2\frac{kx_1x_3}{\rho^2} \\ 0 & -a^2\frac{kx_1x_2}{\rho^2} & -a^2\frac{1-k(x_1^2+x_3^2)}{\rho^2} & -a^2\frac{kx_2x_3}{\rho^2} \\ 0 & -a^2\frac{kx_1x_3}{\rho^2} & -a^2\frac{kx_2x_3}{\rho^2} & -a^2\frac{1-k(x_1^2+x_2^2)}{\rho^2} \end{pmatrix}.$$

The inverse of $g_{\mu\nu}$ is given by

$$g^{\mu\nu} = \begin{pmatrix} 1 & 0 & 0 & 0 \\ 0 & -\frac{1-kx_1^2}{a^2} & \frac{kx_1x_2}{a^2} & \frac{kx_1x_3}{a^2} \\ 0 & \frac{kx_1x_2}{a^2} & -\frac{1-kx_2^2}{a^2} & \frac{kx_2x_3}{a^2} \\ 0 & \frac{kx_1x_3}{a^2} & \frac{kx_2x_3}{a^2} & -\frac{1-kx_3^2}{a^2} \end{pmatrix}.$$

2.2 *Affine connections*

Using $g_{\mu\nu}$ and $g^{\mu\nu}$ as given in equations (5) and (6) we calculate the affine connecti $\Gamma^\alpha_{\mu\nu}$ with $\alpha, \mu, \nu = 0, 1, 2, 3$ to take the form

$$\Gamma^0_{\mu\nu} = \begin{pmatrix} 0 & 0 & 0 & 0 \\ 0 & a\dot{a}\left(1+\frac{kx_1^2}{\rho^2}\right) & a\dot{a}\frac{kx_1x_2}{\rho^2} & a\dot{a}\frac{kx_1x_3}{\rho^2} \\ 0 & a\dot{a}\frac{kx_1x_2}{\rho^2} & a\dot{a}\left(1+\frac{kx_2^2}{\rho^2}\right) & a\dot{a}\frac{kx_2x_3}{\rho^2} \\ 0 & a\dot{a}\frac{kx_1x_3}{\rho^2} & a\dot{a}\frac{kx_2x_3}{\rho^2} & a\dot{a}\left(1+\frac{kx_3^2}{\rho^2}\right) \end{pmatrix},$$

$$\Gamma^1_{\mu\nu} = \begin{pmatrix} 0 & \dot{a}/a & 0 & 0 \\ \dot{a}/a & kx_1\left(1+\frac{kx_1^2}{\rho^2}\right) & \frac{k^2x_1^2x_2}{\rho^2} & \frac{k^2x_1^2x_3}{\rho^2} \\ 0 & \frac{k^2x_1^2x_2}{\rho^2} & kx_1\left(1+\frac{kx_2^2}{\rho^2}\right) & \frac{k^2x_1x_2x_3}{\rho^2} \\ 0 & \frac{k^2x_1^2x_3}{\rho^2} & \frac{k^2x_1x_2x_3}{\rho^2} & kx_1\left(1+\frac{kx_3^2}{\rho^2}\right) \end{pmatrix}, \tag{8}$$

$$\Gamma^2_{\mu\nu} = \begin{pmatrix} 0 & 0 & \dot{a}/a & 0 \\ 0 & kx_2\left(1+\frac{kx_1^2}{\rho^2}\right) & \frac{k^2x_1x_2^2}{\rho^2} & \frac{k^2x_1x_2x_3}{\rho^2} \\ \dot{a}/a & \frac{k^2x_1x_2^2}{\rho^2} & kx_2\left(1+\frac{kx_2^2}{\rho^2}\right) & \frac{k^2x_2^2x_3}{\rho^2} \\ 0 & \frac{k^2x_1x_2x_3}{\rho^2} & \frac{k^2x_2^2x_3}{\rho^2} & kx_2\left(1+\frac{kx_3^2}{\rho^2}\right) \end{pmatrix}, \tag{9}$$

$$\Gamma^3_{\mu\nu} = \begin{pmatrix} 0 & 0 & 0 & \dot{a}/a \\ 0 & kx_3\left(1+\frac{kx_1^2}{\rho^2}\right) & \frac{k^2x_1x_2x_3}{\rho^2} & \frac{k^2x_1x_3^2}{\rho^2} \\ 0 & \frac{k^2x_1x_2x_3}{\rho^2} & kx_3\left(1+\frac{kx_2^2}{\rho^2}\right) & \frac{k^2x_2x_3^2}{\rho^2} \\ \dot{a}/a & \frac{k^2x_1x_3^2}{\rho^2} & \frac{k^2x_2x_3^2}{\rho^2} & kx_3\left(1+\frac{kx_3^2}{\rho^2}\right) \end{pmatrix}. \tag{10}$$

2.3 *Curvature dependent Dirac matrices*

Henceforth curvature dependent Dirac matrices are written as $\gamma_\mu(x)$ and satisfy the anti-commutation rule $\gamma_\mu\gamma_\nu + \gamma_\nu\gamma_\mu = 2g_{\mu\nu}$. The curvature independent ordinary Dirac matrices are denoted by γ_a, where $\mu, a = 0,1,2,3$; $\gamma_a\gamma_b + \gamma_b\gamma_a = 2\eta_{ab}$; $\eta_{00} = 1$, $\eta_{ii} = -1$, $\eta_{0i} = 0$. The relation between $\gamma_\mu(x)$ and γ_a is given by vierbein-components L^a_μ defined through the relation

$$\gamma_\mu(x) = L^a_\mu(x)\gamma_a. \tag{11}$$

For R-W spacetime the vierbein are fixed through

$$\mathrm{d}s^2 = L^a_\mu L_{\nu a}\mathrm{d}x^\mu \mathrm{d}x^\nu. \tag{12}$$

Here $x^0 \equiv t$, $x^1 \equiv r$, $x^2 \equiv \theta$, $x^3 \equiv \varphi$ and $\mathrm{d}s^2$ is given by (2). We find

$$L^a_\mu = \begin{array}{c} \mu \longrightarrow \\ a \\ \downarrow \end{array} \begin{pmatrix} 1 & 0 & 0 & 0 \\ 0 & a/\rho & 0 & 0 \\ 0 & 0 & ar & 0 \\ 0 & 0 & 0 & ar\sin\theta \end{pmatrix}. \tag{13}$$

In order to find the vierbein in cartesian coordinates denoted by $\widetilde{L}^a_\mu$ we use relation (2)

$$\widetilde{L}^a_\mu = \begin{array}{c} \mu \longrightarrow \\ a \\ \downarrow \end{array} \begin{pmatrix} 1 & 0 & 0 & 0 \\ 0 & \frac{ax_1}{r\rho} & \frac{ax_2}{r\rho} & \frac{ax_3}{r\rho} \\ 0 & \frac{ax_1x_3}{r\sqrt{x_1^2+x_2^2}} & \frac{ax_2x_3}{r\sqrt{x_1^2+x_2^2}} & -\frac{a\sqrt{x_1^2+x_2^2}}{r} \\ 0 & -\frac{ax_2}{r\sqrt{x_1^2+x_2^2}} & \frac{ax_1}{r\sqrt{x_1^2+x_2^2}} & 0 \end{pmatrix}. \tag{14}$$

In case of flat spacetime $k = 0$ (i.e. $\rho = 1$), $\widetilde{L}^a_\mu$ should reduce to a diagonal form. But equation (4) does not reduce to diagonal form for $k = 0$ as is expected. This is due to the fact that the vierbein is defined up to a Lorentz transformation in the flat tangent space. As Lorentz transformation for the 3-space dimensions can be viewed as a rotation, we rotate the vierbein (14) by multiplying it with the rotation matrix

$$R = \begin{pmatrix} 1 & 0 & 0 & 0 \\ 0 & \sin\theta\cos\varphi & \sin\theta\sin\varphi & \cos\theta \\ 0 & \cos\theta\cos\varphi & \cos\theta\sin\varphi & -\sin\theta \\ 0 & -\sin\varphi & \cos\varphi & 0 \end{pmatrix}, \tag{15}$$

or

$$R = \begin{pmatrix} 1 & 0 & 0 & 0 \\ 0 & \frac{x_1}{r} & \frac{x_2}{r} & \frac{x_3}{r} \\ 0 & \frac{x_1x_3}{r\sqrt{x_1^2+x_2^2}} & \frac{x_2x_3}{r\sqrt{x_1^2+x_2^2}} & -\frac{\sqrt{x_1^2+x_2^2}}{r} \\ 0 & -\frac{x_2}{r\sqrt{x_1^2+x_2^2}} & \frac{x_1}{r\sqrt{x_1^2+x_2^2}} & 0 \end{pmatrix}, \tag{15a}$$

to obtain the new vierbein as,

$$\widetilde{L}^a_\mu = \begin{array}{c} \mu \longrightarrow \\ a \\ \downarrow \end{array} \begin{pmatrix} 1 & 0 & 0 & 0 \\ 0 & a\frac{x_1^2+\rho(x_2^2+x_3^2)}{r^2\rho} & \frac{ax_1x_2(1-\rho)}{r^2\rho} & \frac{ax_1x_3(1-\rho)}{r^2\rho} \\ 0 & \frac{ax_1x_2(1-\rho)}{r^2\rho} & a\frac{x_2^2+\rho(x_1^2+x_3^2)}{r^2\rho} & \frac{ax_2x_3(1-\rho)}{r^2\rho} \\ 0 & \frac{ax_1x_3(1-\rho)}{r^2\rho} & \frac{ax_2x_3(1-\rho)}{r^2\rho} & a\frac{x_3^2+\rho(x_1^2+x_2^2)}{r^2\rho} \end{pmatrix}. \tag{16}$$

For $k = 0$ i.e. $\rho = 1$, this matrix turns out to be a diagonal one and moreover, it is also symmetric.

Thus we can calculate the covariant curvature dependent Dirac matrices $\gamma_\mu(x)$ in terms of curvature independent ordinary Dirac matrices γ_a by using equations (11) and (16) which are as follows:

$$\begin{aligned} \gamma_0(x) &= \gamma_0, \\ \gamma_1(x) &= \frac{a}{r^2\rho}[\{x_1^2+\rho(x_2^2+x_3^2)\}\gamma_1 + x_1x_2(1-\rho)\gamma_2 + x_1x_3(1-\rho)\gamma_3], \\ \gamma_2(x) &= \frac{a}{r^2\rho}[x_1x_2(1-\rho)\gamma_1 + \{x_2^2+\rho(x_1^2+x_3^2)\}\gamma_2 + x_2x_3(1-\rho)\gamma_3], \\ \gamma_3(x) &= \frac{a}{r^2\rho}[x_1x_3(1-\rho)\gamma_1 + x_2x_3(1-\rho)\gamma_2 + \{x_3^2+\rho(x_1^2+x_2^2)\}\gamma_3], \end{aligned} \tag{17}$$

relations $\gamma^{\mu}(x) = g^{\mu\nu}\gamma_{\nu}(x)$ and equations (6) and (17), are obtained as

$$\begin{aligned}
\gamma^{0}(x) &= \gamma_0,\\
\gamma^{1}(x) &= \frac{1}{ar^2}[-(\rho x_1^2 + x_2^2 + x_3^2)\gamma_1 + x_1x_2(1-\rho)\gamma_2 + x_1x_3(1-\rho)\gamma_3\\
\gamma^{2}(x) &= \frac{1}{ar^2}[x_1x_2(1-\rho)\gamma_1 - (\rho x_2^2 + x_1^2 + x_3^2)\gamma_2 + x_2x_3(1-\rho)\gamma_3],\\
\gamma^{3}(x) &= \frac{1}{ar^2}[x_1x_3(1-\rho)\gamma_1 + x_2x_3(1-\rho)\gamma_2 - (\rho x_3^2 + x_1^2 + x_2^2)\gamma_3].
\end{aligned}$$

2.4 *Spin connections*

The spin connections are given by the equation

$$\Gamma_{\mu} = -\tfrac{1}{8}[\gamma^{\nu}(x), \gamma_{\nu}(x)_{||\mu}],$$

where the covariant derivative is given by

$$\gamma_{\nu}(x)_{||\mu} = \gamma_{\nu}(x)_{|\mu} - \Gamma^{\alpha}_{\mu\nu}\gamma_{\alpha}(x).$$

We find Γ_{μ} by using equations (7), (8), (9), (10), (17) and (18) as

$$\begin{aligned}
\Gamma_0 &= 0,\\
\Gamma_1 &= -\frac{1}{2}\Bigg[\gamma_1\gamma_0\dot{a}\frac{x_1^2 + \rho(x_2^2 + x_3^2)}{r^2\rho} + \gamma_2\gamma_0\dot{a}\frac{x_1x_2(1-\rho)}{r^2\rho}\\
&\qquad + \gamma_3\gamma_0\dot{a}\frac{x_1x_3(1-\rho)}{r^2\rho} + \gamma_1\gamma_2\frac{x_2(1-\rho)}{r^2} + \gamma_1\gamma_3\frac{x_3(1-\rho}{r^2}\\
\Gamma_2 &= -\frac{1}{2}\Bigg[\gamma_1\gamma_0\dot{a}\frac{x_1x_2(1-\rho)}{r^2\rho} + \gamma_2\gamma_0\dot{a}\frac{x_2^2 + \rho(x_1^2 + x_3^2)}{r^2\rho}\\
&\qquad + \gamma_3\gamma_0\dot{a}\frac{x_2x_3(1-\rho)}{r^2\rho} + \gamma_2\gamma_1\frac{x_1(1-\rho)}{r^2} + \gamma_2\gamma_3\frac{x_3(1-\rho)}{r^2}\\
\Gamma_3 &= -\frac{1}{2}\Bigg[\gamma_1\gamma_0\dot{a}\frac{x_1x_3(1-\rho)}{r^2\rho} + \gamma_2\gamma_0\dot{a}\frac{x_2x_3(1-\rho)}{r^2\rho}\\
&\qquad + \gamma_3\gamma_0\dot{a}\frac{x_3^2 + \rho(x_1^2 + x_2^2)}{r^2\rho} + \gamma_3\gamma_1\frac{x_1(1-\rho)}{r^2} + \gamma_3\gamma_2\frac{x_2(1-\rho}{r^2}
\end{aligned}$$

2.5 *The Dirac equation*

From equations (18) and (21), we get

$$\gamma^{\mu}(x)\Gamma_{\mu}(x) = -\Bigg[\frac{3}{2}\gamma_0\frac{\dot{a}}{a} + \gamma_1\frac{x_1(1-\rho)}{ar^2} + \gamma_2\frac{x_2(1-\rho)}{ar^2} + \gamma_3\frac{x_3(1-\rho)}{ar^2}$$

lso using equations (3) and (18) we may write

$$\gamma^{\mu}(x)\partial_{\mu} = \gamma_0\partial_t - \frac{1}{a}\left[\rho\left(\gamma_1\frac{x_1}{r} + \gamma_2\frac{x_2}{r} + \gamma_3\frac{x_3}{r}\right)\partial_r \right.$$
$$+ \left(\gamma_1\frac{x_1x_3}{r^2\sqrt{x_1^2+x_2^2}} + \gamma_2\frac{x_2x_3}{r^2\sqrt{x_1^2+x_2^2}} - \gamma_3\frac{\sqrt{x_1^2+x_2^2}}{r^2}\right)\partial_\theta$$
$$\left. + \left(-\gamma_1\frac{x_2}{x_1^2+x_2^2} + \gamma_2\frac{x_1}{x_1^2+x_2^2}\right)\partial_\varphi\right]. \tag{23}$$

finally, Dirac equation (1) takes the form through (22) and (23) as

$$\left[i\gamma_0\partial_t + i\frac{3}{2}\gamma_0\frac{\dot a}{a} - \frac{i}{a}\left\{\rho\left(\gamma_1\frac{x_1}{r} + \gamma_2\frac{x_2}{r} + \gamma_3\frac{x_3}{r}\right)\partial_r \right.\right.$$
$$+ \left(\gamma_1\frac{x_1x_3}{r^2\sqrt{x_1^2+x_2^2}} + \gamma_2\frac{x_2x_3}{r^2\sqrt{x_1^2+x_2^2}} - \gamma_3\frac{\sqrt{x_1^2+x_2^2}}{r^2}\right)\partial_\theta$$
$$+ \left(-\gamma_1\frac{x_2}{x_1^2+x_2^2} + \gamma_2\frac{x_1}{x_1^2+x_2^2}\right)\partial_\varphi$$
$$\left.\left. - \gamma_1\frac{x_1(1-\rho)}{r^2} - \gamma_2\frac{x_2(1-\rho)}{r^2} - \gamma_3\frac{x_3(1-\rho)}{r^2}\right\} - m\right]\psi = 0. \tag{24}$$

ve a more compact form of equation (24), we use the transformation of the curvature
endent Dirac matrices in spherical polar coordinates by

$$\begin{pmatrix}\gamma_r\\ \gamma_\theta\\ \gamma_\varphi\end{pmatrix} = \begin{pmatrix}\sin\theta\cos\varphi & \sin\theta\sin\varphi & \cos\theta\\ \cos\theta\cos\varphi & \cos\theta\sin\varphi & -\sin\theta\\ -\sin\varphi & \cos\varphi & 0\end{pmatrix}\begin{pmatrix}\gamma_1\\ \gamma_2\\ \gamma_3\end{pmatrix}, \tag{25}$$

$$\left[i\gamma_0\partial_t + i\,\frac{3}{2}\gamma_0\frac{\dot a}{a} - \frac{i}{a}\left\{\rho\gamma_r\partial_r + \gamma_\theta\frac{1}{r}\partial_\theta + \gamma_\varphi\frac{1}{r\sin\theta}\partial_\varphi - (1-\rho)\frac{\boldsymbol{\gamma}\cdot\mathbf{r}}{r^2}\right\} - m\right]\psi = 0. \tag{26}$$

ultiplying equation (26) by $-i\gamma_0$ and using the relation $\gamma_i = \gamma_0\alpha_i$, $\alpha_i = \gamma_0\gamma_i$, it
nes

$$\left[\partial_t + \frac{3}{2}\frac{\dot a}{a} + im\gamma_0 - \frac{1}{a}\left\{\boldsymbol{\alpha}\cdot\nabla + (\rho-1)\alpha_r\left(\partial_r + \frac{1}{r}\right)\right\}\right]\psi = 0, \tag{27}$$

n reduces to the flat spacetime equation for $\rho = 1$ i.e.,

$$\left[\partial_t + \frac{3}{2}\frac{\dot a}{a} + im\gamma_0 - \frac{1}{a}\boldsymbol{\alpha}\cdot\nabla\right]\psi = 0. \tag{28}$$

3. Solution of the Dirac equation

It is better to find out a diagonal tetrad gauge than the cartesian tetrad equation, becau is not so simple to find out the solution of eq. (27) for $\rho = 1$, as the flat space equation for $\rho = 0$. On the other hand there is a study on the necessary and suffi condition for the separability of equations obtained from the diagonal tetrad ga Moreover, there is a unitary transformation that maps the Dirac equation in the diag tetrad gauge into the equation in cartesian tetrad gauge.

In this case, metric (2) can be written by changing the variables

$$\begin{aligned} \mathrm{d}t &= \exp\left(\tfrac{1}{2}\alpha(\tau)\right)\mathrm{d}\tau, \\ a(t) &= \exp\left(\tfrac{1}{2}\alpha(\tau)\right), \\ r &= \xi(\chi), \end{aligned}$$

as,

$$\mathrm{d}s^2 = \mathrm{e}^{\alpha(\tau)}[\mathrm{d}\tau^2 - \{\mathrm{d}\chi^2 + \xi^2(\chi)(\mathrm{d}\theta^2 + \sin^2\theta \mathrm{d}\varphi^2)\}]$$

such that

$$\xi(\chi) = \begin{cases} \sin\chi, & \text{for } k = +1, \\ \chi, & \text{for } k = 0, \\ \sinh\chi, & \text{for } k = -1. \end{cases}$$

Using metric (30), the Dirac equation (1) takes the form

$$\Bigg[\mathrm{e}^{-\frac{1}{2}\alpha(\tau)}\Bigg\{i\gamma_0\partial_\tau + i\frac{3}{4}\gamma_0\dot{\alpha} - i\Bigg(\gamma_1\left(\partial_\chi + \frac{\xi'}{\xi}\right) + \gamma_2\frac{1}{\xi}\left(\partial_\theta + \frac{1}{2}\cot\theta\right) + \gamma_3\frac{1}{\xi\sin\theta}\partial_\varphi\Bigg)\Bigg\} - m\Bigg]\bar{\psi} = 0,$$

or simply

$$\left[\partial_\tau + \frac{3}{4}\dot{\alpha} - \left\{\alpha_1\left(\partial_\chi + \frac{\xi'}{\xi}\right) + \alpha_2\frac{1}{\xi}\left(\partial_\theta + \frac{1}{2}\cot\theta\right) + \alpha_3\frac{1}{\xi\sin\theta}\partial_\varphi\right\} + im\gamma_0\mathrm{e}^{\frac{1}{2}\alpha}\right]\bar{\psi}$$

(

where $\dot{\alpha} = \partial\alpha/\partial\tau$ and $\xi' = \partial\xi/\partial\chi$. The unitary transformation S that maps equation (into equation (27) is

$$\bar{\psi} = S\psi,$$

where

$$S = \frac{1}{2}(\gamma_1\gamma_2 + \gamma_2\gamma_3 + \gamma_3\gamma_1 + 1)\exp\left(-\frac{\theta}{2}\gamma_3\gamma_1\right)\exp\left(-\frac{\varphi}{2}\gamma_1\gamma_2\right),$$

and its inverse is

$$S^{-1} = \exp\left(\frac{\varphi}{2}\gamma_1\gamma_2\right)\exp\left(\frac{\theta}{2}\gamma_3\gamma_1\right)\frac{1}{2}(1 - \gamma_1\gamma_2 - \gamma_2\gamma_3 - \gamma_3\gamma_1).$$

transformation some of the identities (see Appendix A in which one of the identities is given in detail) are given below:

$$
\begin{aligned}
&S^{-1}\gamma_1\left(\partial_\chi+\frac{\xi'}{\xi}\right)(S\psi)=(\gamma_1\sin\theta\cos\varphi+\gamma_2\sin\theta\sin\varphi+\gamma_3\cos\theta)\left(\partial_\chi+\frac{\xi'}{\xi}\right)\psi,\\
&S^{-1}\gamma_2(\partial_\theta+\tfrac{1}{2}\cot\theta)(S\psi)=-\tfrac{1}{2}(\gamma_1\sin\theta\cos\varphi+\gamma_2\sin\theta\sin\varphi+\gamma_3\cos\theta)\psi\\
&\quad+\tfrac{1}{2}\cot\theta(\gamma_1\cos\theta\cos\varphi+\gamma_2\cos\theta\sin\varphi-\gamma_3\sin\theta)\psi \qquad (36)\\
&\quad+(\gamma_1\cos\theta\cos\varphi+\gamma_2\cos\theta\sin\varphi-\gamma_3\sin\theta)\partial_\theta\psi,\\
&S^{-1}\gamma_3\partial_\varphi(S\psi)=-\tfrac{1}{2}(\gamma_1\cos\varphi+\gamma_2\sin\varphi)\psi+(\gamma_2\cos\varphi-\gamma_1\sin\varphi)\partial_\varphi\psi.
\end{aligned}
$$

From equations (29) and (31), we get

$$\dot a=\frac{1}{2}\dot\alpha,\, \partial_\tau+\frac{3}{4}\dot\alpha=\mathrm{e}^{\alpha/2}\left(\partial_t+\frac{3}{2}\frac{\dot a}{a}\right),\quad \partial_\chi+\frac{\xi'}{\xi}=\rho\partial_r+\frac{1}{r}\rho.$$

Using these results and the identities (36), it is possible to show that equation (32a) is exactly mapped into equation (27) (see Appendix B)

In order to separate the variables of (32), we take

$$\bar\psi=\xi^{-1}(\chi)\sin^{-(1/2)}\theta\mathrm{e}^{-(3/4)\alpha(\tau)}\Phi, \tag{37}$$

with $\Phi=\frac{1}{2}(\gamma_0\gamma_1+\gamma_2\gamma_0+\gamma_0\gamma_3-\gamma_0\gamma_1\gamma_2\gamma_3)\Sigma$ and

$$\Sigma=\begin{pmatrix} f(\tau)b(\chi)\Theta_1(\theta)\\ f(\tau)b(\chi)\Theta_2(\theta)\\ g(\tau)a(\chi)\Theta_1(\theta)\\ -g(\tau)a(\chi)\Theta_2(\theta)\end{pmatrix}\mathrm{e}^{in\varphi}, \tag{38}$$

where n takes the values $\pm1/2$, $\pm3/2$, $\pm5/2,\ldots$. We get the following four equations:

$$\frac{1}{f}(i\partial_\tau+m\mathrm{e}^{\alpha/2})g-\frac{1}{a}\partial_\chi b+\frac{i}{\xi}\frac{b}{a}\frac{\partial_\theta(\Theta_1-\Theta_2)}{\Theta_1-\Theta_2}+\frac{n}{\xi\sin\theta}\frac{b}{a}\frac{\Theta_1+\Theta_2}{\Theta_1-\Theta_2}=0, \tag{39}$$

$$\frac{1}{f}(i\partial_\tau+m\mathrm{e}^{\alpha/2})g+\frac{1}{a}\partial_\chi b+\frac{i}{\xi}\frac{b}{a}\frac{\partial_\theta(\Theta_1+\Theta_2)}{\Theta_1+\Theta_2}-\frac{n}{\xi\sin\theta}\frac{b}{a}\frac{\Theta_1-\Theta_2}{\Theta_1+\Theta_2}=0, \tag{40}$$

$$\frac{1}{g}(i\partial_\tau-m\mathrm{e}^{\alpha/2})f-\frac{1}{b}\partial_\chi a+\frac{i}{\xi}\frac{a}{b}\frac{\partial_\theta(\Theta_1+\Theta_2)}{\Theta_1+\Theta_2}+\frac{n}{\xi\sin\theta}\frac{a}{b}\frac{\Theta_1-\Theta_2}{\Theta_1+\Theta_2}=0, \tag{41}$$

$$\frac{1}{g}(i\partial_\tau-m\mathrm{e}^{\alpha/2})f+\frac{1}{b}\partial_\chi a+\frac{i}{\xi}\frac{a}{b}\frac{\partial_\theta(\Theta_1-\Theta_2)}{\Theta_1-\Theta_2}-\frac{n}{\xi\sin\theta}\frac{a}{b}\frac{\Theta_1+\Theta_2}{\Theta_1-\Theta_2}=0. \tag{42}$$

First term of equations (39), (40), (41), (42) are dependent on τ only and rest parts of each of the equations are independent of τ. Hence the first term of each of the equations should be equal to a constant λ (say) and thus we get, for the functions $f(\tau)$ and $g(\tau)$, the coupled equations:

$$\left(\frac{\mathrm{d}}{\mathrm{d}\tau}-im\mathrm{e}^{(1/2)\alpha(\tau)}\right)g(\tau)=-i\lambda f(\tau) \tag{43}$$

and

$$\left(\frac{\mathrm{d}}{\mathrm{d}\tau}+ime^{(1/2)\alpha(\tau)}\right)f(\tau)=-i\lambda g(\tau). \tag{44}$$

Premultiplying (43) by $((\mathrm{d}/\mathrm{d}\tau)+ime^{(1/2)\alpha(\tau)})$ and equation (44) by $((\mathrm{d}/\mathrm{d}\tau)-ime^{(1/2)\alpha(\tau)})$ and using eqs (43) and (44), results in a pair of uncoupled second order equations

$$\left[\frac{\mathrm{d}^2}{\mathrm{d}\tau^2}+\frac{1}{2}im\dot{\alpha}\mathrm{e}^{(1/2)\alpha(\tau)}+\lambda^2+m^2\mathrm{e}^{\alpha(\tau)}\right]f(\tau)=0 \tag{45}$$

and

$$\left[\frac{\mathrm{d}^2}{\mathrm{d}\tau^2}-\frac{1}{2}im\dot{\alpha}\mathrm{e}^{(1/2)\alpha(\tau)}+\lambda^2+m^2\mathrm{e}^{\alpha(\tau)}\right]g(\tau)=0. \tag{46}$$

The result obtained in this section i.e. equations (43) to (46) differs from Barut and Singh but is consistent with Sahni. We will consider (43) and (44) to understand particle production in Kasner spacetime and in some other cases.

4. Parametric resonance particle production

We write eqs (43) to (46) in the form

$$i\frac{\partial\psi}{\partial\tau}=H\psi, \tag{47}$$

and in the second order form

$$\left[\frac{\partial^2}{\partial\tau^2}+(\lambda^2+m^2c^2(\tau)\pm im\dot{c}(\tau))\right]\psi=0. \tag{48}$$

Here

$$\psi=\begin{pmatrix} f \\ g \end{pmatrix} \quad \text{and} \quad H=\sigma^3 mc(\tau)+\sigma^1\lambda, \tag{49}$$

and σ^i are the usual Pauli 2×2 matrices. The complex time WKB (CWKB) approximation allows us to calculate pair production amplitude as follows [9–12]. We determine the complex turning points $\tau_{1,2}$ from

$$\omega(\tau_{1,2})\equiv[\lambda^2+m^2c^2(\tau)\pm im\dot{c}(\tau)]^{1/2}=0, \tag{50}$$

and the pair production amplitude is given by

$$R=-\frac{i\exp[2i\int^{\tau_1}\omega_\lambda(\tau)\mathrm{d}\tau]}{1+\exp[2i\int_{\tau_1}^{\tau_2}\omega_\lambda(\tau)\mathrm{d}\tau}. \tag{51}$$

In obtaining eq. (51) we assumed that particle–antiparticle states are determined through zeroeth order WKB approximation to eq. (48). From eq. (51) it follows that R has poles at

$$\int_{\tau_1}^{\tau_2}\omega_\lambda(\tau)\mathrm{d}\tau=\left(N+\frac{1}{2}\right)\pi, \quad N=0,1,2,\ldots. \tag{52}$$

When the condition (52) is violated the poles become resonances and we get resonance particle production. Because of recent interest in parametric resonance particle production [23–26], we consider Mathieu-type equation which is generally used to understand catastrophic particle production

$$\frac{\mathrm{d}^2 u}{\mathrm{d}z^2} + [h - 2\theta \cos(2z)]u = 0. \tag{53}$$

The advantage of our method lies in the WKB vacuum definition (usually taken at $|\tau| \to \infty$). In cosmology we sometime require to know the particle production at an intermediate stage to obtain the late time evolution of the universe. In such cases the parameter θ may be large and the WKB vacuum definition remains valid even at finite τ.

To demonstrate, we consider large θ approximation and replace the periodic barriers by piece-wise inverted harmonic oscillator; and take $|z| < \frac{\pi}{2}$ such that $\cos(2z) \to (1 - 2z^2)$. We write eq.(53) as

$$\frac{\mathrm{d}^2 u}{\mathrm{d}z'^2} + [\lambda + z'^2]u = 0, \tag{54}$$

with

$$\lambda = \sqrt{\theta}\epsilon, \quad \epsilon = \frac{h}{2\theta} - 1, \quad z' = (4\theta)^{1/4} z. \tag{55}$$

The turning points are at $z' = \pm i\lambda$. We evaluate eq. (51) to get

$$\begin{aligned} |R|^2 &= \frac{\exp(-\pi\lambda)}{1 + \exp(-\pi\lambda)} \\ &= \frac{\exp(-\pi\sqrt{\theta}\epsilon)}{1 + \exp(-\pi\sqrt{\theta}\epsilon)}. \end{aligned} \tag{56}$$

The solution of eq.(54) can be written in terms of the standard parabolic cylindrical function $D_{-(i\sqrt{\theta}\epsilon + (1/2))}(\mathrm{e}^{i\pi/4} 2\theta^{1/4} z)$ which in large θ approximation will satisfy, at finite z, the conditions of WKB definition of particle–antiparticle states. Using the relation $\Gamma(z)\Gamma(1 - z) = \pi/(\sin(\pi z))$, we can determine the standard Bogolubov coefficients α and β from eq.(56) with identification $R = \beta/\alpha$ as

$$\alpha = \frac{\sqrt{2\pi}\theta^{-i\sqrt{\theta}\epsilon/4} \mathrm{e}^{-\pi\sqrt{\theta}\epsilon/4}}{\Gamma((1 + i\sqrt{\theta}\epsilon)/2)}, \quad \beta = \mathrm{e}^{-\pi\sqrt{\theta}\epsilon/2}. \tag{57}$$

This result exactly coincides with [26]. The solution of eq.(53) is written as

$$u(z) = \mathrm{e}^{\lambda z} P(z), \tag{58}$$

with λ real and positive, and $P(z)$, a periodic function. To obtain λ in (58) we have to consider a large number of repeated barrier crossovers to obtain $\lambda \sim (1/\pi) \ln(\mathrm{e}^{-\pi\sqrt{\theta}\epsilon/2}) = (\sqrt{\theta}\epsilon)/2$.Thus we find that parametric resonance particle production is basically CWKB resonance particle production in parameter space (θ, h).

We have considered eq. (53) to understand the effectiveness of our approach. In the next chapter we consider the particle production in Kasner's spacetime through CWKB to understand some salient features of particle production. The above example of particle production in parameter space allows us to define particle–antiparticle states even when $|\eta| \not\to \infty$.

5. The Kasner spacetime

We now concentrate primarily on the Kasner spacetime to study the pair production. In this case we find that temporal equation shows the existence of complex turning points which are needed to evaluate the pair production.

The Kasner metric is given by

$$\mathrm{d}s^2 = \mathrm{d}t^2 - t^{2a_1}\mathrm{d}x^2 - t^{2a_2}\mathrm{d}y^2 - t^{2a_3}\mathrm{d}z^2, \tag{59}$$

where a_1, a_2 and a_3 are real numbers. The spacetime (59) is a model of anisotropically expanding universe and is a solution of vacuum Einstein equation subject to the constraint

$$a_1 + a_2 + a_3 = a_1^2 + a_2^2 + a_3^2 = 1. \tag{60}$$

In the non-degenerate case the a_is are non-vanishing and none of the a_is are equal. On the other hand in the degenerate case one of the a_is is equal to unity, while the others are vanishing. We choose corresponding to eq. (59)

$$\gamma^0(t) = \gamma_0 = \beta, \quad \gamma^i(t) = t^{-a_i}\gamma^i, \quad i = 1, 2, 3. \tag{61}$$

Also we have

$$\eta_{\mu\nu} = \mathrm{diag}(1, -1, -1, -1) \tag{62}$$

and

$$\gamma^0 = \begin{pmatrix} I & 0 \\ 0 & I \end{pmatrix}; \quad \gamma^i = \beta\alpha^i; \quad \alpha^i = \begin{pmatrix} 0 & \sigma^i \\ \sigma^i & 0 \end{pmatrix}, \tag{63}$$

represent flat γ-matrices, while σ^i are 2 × 2 Pauli matrices. The Christoffel symbols $\Gamma^\mu_{\nu\rho}$ and the spin connections Γ_μ are evaluated to get

$$\tilde{\gamma}^\mu\Gamma_\mu = -\frac{\gamma^0}{2t}. \tag{64}$$

Using eq. (64) in equation (1) we have the Dirac equation in Kasner spacetime to have the form

$$\left[i\gamma^0\partial_0 + i(t^{-a_1}\gamma^1\partial_1 + t^{-a_2}\gamma^2\partial_2 + t^{-a_3}\gamma^3\partial_3) + \frac{i\gamma^0}{2t} - m\right]\psi = 0. \tag{65}$$

Substituting

$$\psi = t^{-1/2}\bar{\psi}, \tag{66}$$

in eq. (65) and using eq. (63) we have

$$[\partial_0 + t^{-a_1}\alpha^1\partial_1 + t^{-a_2}\alpha^2\partial_2 + t^{-a_3}\alpha^3\partial_3 + i\gamma^0 m]\bar{\psi} = 0. \tag{67}$$

If we introduce

$$\bar{\psi} = \frac{1}{2\pi^{3/2}} \mathrm{e}^{i\mathbf{k}\cdot\mathbf{x}} \begin{pmatrix} f_1 \\ f_2 \end{pmatrix}, \tag{68}$$

and also using eq. (63) then, like eqs (43) and (44), the functions f_1 and f_2 satisfy the coupled equations

$$(\partial_0 + im) f_1 + i(t^{-a_1}\sigma^1 k_1 + t^{-a_2}\sigma^2 k_2 + t^{-a_3}\sigma^3 k_3) f_2 = 0, \tag{69}$$

$$(\partial_0 - im) f_2 + i(t^{-a_1}\sigma^1 k_1 + t^{-a_2}\sigma^2 k_2 + t^{-a_3}\sigma^3 k_3) f_1 = 0. \tag{70}$$

We note that we can go over to the flat space by identifying

$$\beta = \gamma^0; \quad \gamma^i \partial_i = \gamma\cdot\nabla = i\beta\alpha\cdot\nabla. \tag{71}$$

We seek to find the WKB solutions of (69) and (70) both in non-degenerate and in degenerate case.

5.1 *Non-degenerate case*

We use the transformations

$$A' = UAU^{\dagger}, \quad \partial_{t'} = U\partial_0 U^{\dagger}, \quad f = Uf_1, \quad g = Uf_2, \tag{72}$$

where

$$A = t^{-a_1}\sigma^1 k_1 + t^{-a_2}\sigma^2 k_2 + t^{-a_3}\sigma^3 k_3, \quad A' = \begin{pmatrix} \lambda & 0 \\ 0 & -\lambda \end{pmatrix},$$

$$\lambda = \sqrt{c_1^2 + c_2^2 + c_3^2}, \quad c_i = t^{-a_i} k_i, \quad U = \begin{pmatrix} r_1 \mathrm{e}^{i\phi/2} & r_2 \mathrm{e}^{-i\phi/2} \\ r_2 \mathrm{e}^{i\phi/2} & -r_1 \mathrm{e}^{-i\phi/2} \end{pmatrix}$$

and

$$r_1 = \sqrt{\frac{1}{2}\left(1 + \frac{c_3}{\lambda}\right)}, \quad r_2 = \sqrt{\frac{1}{2}\left(1 - \frac{c_3}{\lambda}\right)}, \quad \phi = \tan^{-1}\left(\frac{c_2}{c_1}\right).$$

As a result $\partial_{t'}$ takes the form

$$\partial_{t'} = \partial_t - \frac{ic_1 c_2 c_3 (a_1 - a_2)}{2\lambda(c_1^2 + c_2^2)} t^{-1}. \tag{73}$$

Equations (69) and (70) becomes

$$(\partial_{t'} + im) f + iA' g = 0 \tag{74}$$

and

$$(\partial_{t'} - im) g + iA' f = 0. \tag{75}$$

Premultiplying eq. (74) by iA'/λ^2 and operating by $(\partial_{t'} - im)$ from left and also using eq. (75) we get uncoupled equation for f,

$$[\partial_{t'}{}^2 - \partial_{t'}(\ln\lambda)\partial_{t'} - im\partial_{t'}(\ln\lambda) + \lambda^2 + m^2] f = 0. \tag{76}$$

Similarly for g using $f(t, -m)$,

$$g(t, m) = f(t, -m). \tag{77}$$

Substituting $f = \mathrm{e}^{(1/2)\int \partial_{t'}(\ln\lambda)\mathrm{d}t'} y$ in eq. (76) and also using eq. (73) it turns to be of the form

$$[\partial_t^2 + \Omega^2(t)]z = 0, \tag{78}$$

where

$$y = \mathrm{e}^{(1/2)\int 2iq(t)\mathrm{d}t} z, \quad q(t) = \frac{c_1 c_2 c_3 (a_1 - a_2)}{2\lambda(c_1^2 + c_2^2)} t^{-1}.$$

5.2 *Degenerate case*

In curved spacetime the role of vacuum is not well resolved. To understand the role of vacuum, we concentrate on degenerate Kasner spacetime in the light of CWKB technique and evaluate the pair production amplitude. This is done to elucidate the vacuum with respect to strong and weak vacuum [8, 27–29]. The study of particle production in the degenerate Kasner spacetime is interesting because of its striking similarity with the Milne universe.

In the degenerate case we take $a_1 = a_3 = 0$ and $a_2 = 1$, so that Kasner metric (59) reduces to

$$\mathrm{d}s^2 = \mathrm{d}t^2 - (\mathrm{d}x^2 + t^2\mathrm{d}y^2 + \mathrm{d}z^2). \tag{79}$$

Accordingly eq. (67) becomes

$$[\partial_0 + \alpha^1\partial_1 + t^{-1}\alpha^2\partial_2 + \alpha^3\partial_3 + i\gamma^0 m]\bar{\psi} = 0. \tag{80}$$

We insert in eq. (80) the following

$$\bar{\psi} \sim \mathrm{e}^{i\mathbf{k}\cdot\mathbf{x}}\chi, \tag{81}$$

where

$$\chi = \begin{pmatrix} f_1 \\ f_2 \end{pmatrix} \tag{82}$$

and define

$$\begin{aligned} {k_+}^2 &= {k_1}^2 + {k_3}^2, \\ M^2 &= {k_+}^2 + m^2, \\ \beta' M &= \alpha^1 k_1 + \alpha^3 k_3 + \beta m. \end{aligned} \tag{83}$$

Equation (80) then takes the form

$$[i\partial_0 - \alpha^2 k_2 t^{-1} - \beta' M]\chi = 0. \tag{84}$$

As eq. (84) has only two anticommuting variables we may choose

$$\beta' = \sigma^3 \quad \text{and} \quad \alpha^2 = \sigma^1, \tag{85}$$

as if (84) reduces to Dirac equation

$$i\partial_0\psi = H\psi, \tag{86}$$

where

$$\psi = \begin{pmatrix} \chi_1 \\ \chi_2 \end{pmatrix}, \tag{87}$$

$$H = \sigma^1 k_2 t^{-1} + \sigma^3 M. \tag{88}$$

This equation has a remarkable similarity with Dirac equation in time dependent electromagnetic field [18]. The basic feature of reflection and particle production in the work of Cornwall and Tiktopoulos [18] is that the external field (in our case it is the gravitational field) acts between t_1 and t_2. For $t < t_1$ there is no particle but at $t > t_2$ (or $t \to +\infty$) the solutions behave such that it becomes a mixture of particle–antiparticle solutions and is written in terms of free orthonormals. Cornwall and Tiktopoulos demanded that between t_1 and t_2 the spinor suffers a rotation of odd multiple of π in order to have pair production. It may be mentioned that the particle production in an electric and gravitational field was also explicitly calculated for scalar and spinors by Sahni [30]; however, our approach is very much similar to particle production in flat spacetime using Feynman–Stuckleburg prescription.

We generalize the above approach through our *complex time multiple reflection technique* for which it is necessary to find out two solutions that will behave like particle and antiparticle at $t \to \infty$ in order to fix up the vacuum. Though not mentioned in the work of Cornwall and Tiktopoulos we observe that $t = t_1$ and $t = t_2$ must be two turning points to be determined from the second order Dirac equation corresponding to eq. (84). We show that for a system having turning points this particle–antiparticle transformation takes place very naturally [15].

(i) To generalize the work of Cornwall and Tiktopoulos [18] we used particle–antiparticle definitions in curved spacetime as follows. We adopt WKB definition of particle–antiparticle [8, 27–29] solutions such that

$$\lim_{\eta\to\mp\infty} U^{\text{in}}_{\text{out}} \simeq \exp(iS^{\text{in}}_{\text{out}}) \tag{89}$$

and

$$\lim_{\eta\to\mp\infty} V^{\text{in}}_{\text{out}} \simeq \exp(-iS^{\text{in}}_{\text{out}}), \tag{90}$$

respectively. Here

$$S^{\text{in}}_{\text{out}} = \lim_{\eta\to\mp\infty} S \tag{91}$$

and S is a solution of Hamilton–Jacobi equation.

(ii) To have reflection in time we must have turning points.

(iii) The pair production amplitude depends on two fixed points i.e. the turning points. We use eq. (82) in eq. (84) to have coupled equations

$$(\partial_0 + iM) f_1 + ik_2 t^{-1} f_2 = 0, \tag{92}$$

$$(\partial_0 - iM) f_2 + ik_2 t^{-1} f_1 = 0. \tag{93}$$

Premultiplying eq. (92) by t and then operating by $(\partial_0 - iM)$ from left and using (93) we have, like eq. (78),

$$[\partial_\eta^2 + \Omega^2(\eta)] f_1 = 0, \tag{94}$$

where we have introduced

$$t = \mathrm{e}^\eta \tag{95}$$

and

$$\Omega(\eta) = [M^2\mathrm{e}^{2\eta} + iM\mathrm{e}^\eta + k_2^2]^{1/2}. \tag{96}$$

We now find the particle production amplitude $|R|^2$ by our non-perturbative method of WKB approximation in complex time. Equation (94) is of the same form of a Schrödinger-like equation (not in space) in conformal time coordinate viz.,

$$\frac{\mathrm{d}^2\psi}{\mathrm{d}\eta^2} + \Omega^2(\eta)\psi = 0, \tag{97}$$

where

$$\Omega(\eta) = (\omega^2 - V)^2, \tag{98}$$

with ω playing the role of energy and V being a potential term. We define the following

$$\begin{aligned} \tau &= M\mathrm{e}^\eta, \\ b &= -\frac{i}{2}, \\ c &= -ik_2. \end{aligned} \tag{99}$$

The turning points τ_1 and τ_2 are now obtained from

$$\Omega(\tau_{1,2}) = 0, \tag{100}$$

to be

$$\begin{aligned} \tau_1 &= b + \sqrt{b^2 + c^2}, \\ \tau_2 &= b - \sqrt{b^2 + c^2}. \end{aligned} \tag{101}$$

Since the particle production amplitude R (see Appendix C) is given by

$$R = \frac{\mathrm{e}^{2iS(\tau_1)}}{1 + \mathrm{e}^{2iS(\tau_1,\tau_2)}}, \tag{102}$$

where from equation

$$S(\eta) = \int \Omega(\eta)\mathrm{d}\eta, \tag{103}$$

we get

$$S(\tau_1) = \frac{\pi}{4} - \frac{\pi i k_2}{2} \tag{104}$$

$$S(\tau_1, \tau_2) = \frac{\pi}{2} - \pi i k_2. \tag{105}$$

The pair production amplitude can now be obtained employing (102) to be

$$|R|^2 = \frac{e^{2\pi k_2}}{1 + e^{4\pi k_2} - 2e^{2\pi k_2}}. \tag{106}$$

The result shows that there is particle production. If we wish to obtain the result for Milne universe herefrom, we may set $k_1 = k_3 = 0$ which means from eq. (83)

$$M = m, \tag{107}$$

and the pair production amplitude will be of the same form of eq. (106), as it is independent of $M = m$ and thus we get particle production even in Milne universe in two dimension. It is a new result and needs careful analysis. We have based our calculation on WKB approximation and adopted the WKB prescription of particle–antiparticle. So the in vacuum and out vacuum are adiabatic vacuum. It is surprising to find pair production even in adiabatic vacuum which is possible when $|0, \mathrm{in}\rangle \neq |0, \mathrm{out}\rangle$ though both are defined in terms of adiabatic modes. The standard result for the Milne universe in two dimension [9, 16, 31] are as follows:

(1) There is no pair production in adiabatic vacuum.
(2) There is pair production in conformal vacuum.

These two facts are based upon the solutions of the temporal equation [16]. However, our result does not rely upon a particular solution and depends only on the turning points and the extra phase obtained through reflections. It is a global feature of Robertson–Walker spacetime.

The standard arguments for the Milne or Chitre Hartle universe both in two and four dimensions reveal that under coordinate transformation the metric reduces to Minkowski spacetime and hence we do not see any pair production in Milne universe. From our approach it is clear that as soon as one does the coordinate transformation to reduce to a Minkowski spacetime-like metric, (a) one squeezes the spacetime instead of the whole as in the original universe. (b) It also gets rid of the turning points. This in turn means that an electron in a Milne universe is definitely not equivalent to some other electron in another spacetime obtained after coordinate transformation. Hence seeing the similarity of Milne universe with Minkowski spacetime it is not desirable to comment on the existence or non-existence of pair production.

6. Discussion

The method which we have developed has its basis in the Feynman–Stuckleburg prescription according to which negative energy particle solutions propagating backward in time is considered equivalent to positive energy antiparticle solutions propagating forward in time. Accordingly the e^+e^- pair creation from a potential (where we have positive energy e^+ and e^-, both propagating forward in time) may be treated as being equivalent to the reflection of a negative energy electron initially propagating backward in time, to suffer reflection in time thereby giving way to a positive energy electron moving forward in time. Alternatively, particle production can be viewed upon as a process of reflection in time due to which there is no particle present at $t \to -\infty$ but at $t \to +\infty$ there is a particle moving forward in time and an antiparticle moving backward in time. In CWKB the wave starts from a real point and suffers reflection at the complex turning points. Knoll and Schaeffer [32, 33], Schrempp and Schrempp [34] developed the method of complex semiclassical paths in space which they have utilized in calculating scattering amplitude (in case of reflection in space). We extended their method invoking complex semiclassical paths in time which is used to calculate pair production amplitude (in the case of reflection in time).

Elsewhere [10] we have established an analogy of CWKB with moving mirror example in curved spacetime. Similarity of pair production in gravitational field with that of electromagnetic field has been elucidated in our earlier works [12]. As the production of particles carried out in our approach is remarkably similar to pair production in electromagnetic field, it is thus supposed that instability of the vacuum is the root cause of pair production in such a situation as in electromagnetic case. $\mathrm{Im}\mathcal{L}_{\mathrm{eff}}$, which is needed to measure the instability of vacuum, can be calculated, as in our earlier work [10], in CWKB, without taking recourse to Bogolubov coefficient.

Let us now present a synopsis of the work done here. (i) The particle–antiparticle model in curved spacetime is fixed by zeroeth order WKB solution of the field equation. In other words we have invoked Parker's definition. (ii) The vacuum is chosen from the CWKB solutions which serve as mode solutions for proper adiabatic vacuum. (iii) Occurrence of turning points ensures particle production. This fact is hitherto unnoticed in the literature. These turning points are the characteristic of a given spacetime. (iv) Occurrence of turning points is a common feature of all standard expanding spacetimes. Hence particle production is a general characteristic of expanding spacetimes. (v) The turning points are determined utilizing eq. (98). (vi) The in vacuum in our degenerate Kasner case is Hartle Hawking vacuum as in collapsing star problem [10, 31]. The out vacuum is such that as the particle evolves from the in vacuum, it does not find the out vacuum as a physical vacuum i.e. $|0,\mathrm{in}\rangle \neq |0,\mathrm{out}\rangle$. This occurs because $\int \Omega(\tau)\mathrm{d}\tau\big|_{\tau=\tau_1} \neq 0$. (vii) Mixing of positive and negative frequency modes result in particle production. The situation is like the blackhole problem [10, 30] where mixing of positive and negative frequency states occur at the horizon. (viii) Vacuum acts like a blackhole. In blackhole case hole mass decreases but here vacuum energy changes. In both cases $\mathrm{Im}\mathcal{L}_{\mathrm{eff}}$ remains finite. (ix) The standard explanation of no particle production in Milne universe is that under coordinate transformation, (for two dimension)

$$\begin{aligned} y^0 &= \mathrm{e}^{\eta}\cosh x, \\ y^1 &= \mathrm{e}^{\eta}\sinh x, \end{aligned} \tag{108}$$

with $0 < y^0 < \infty$ and $-\infty < y^1 < \infty$, it reduces to Minkowski spacetime. Hence we do not expect particle production in two dimensional Milne universe. Our calculation, however, contradicts the situation both in two as well as in four dimension. The coordinate transformation washes out the turning points and hence there is no particle production. But the turning points are crucial and acts like horizon [10, 31, 35] and is responsible for mixing of positive and negative frequency states resulting in pair production.

Details in this respect are discussed in our earlier works [10, 11]. The basic calculation is that the vacuum in Milne universe is not the same as Minkowski vacuum and in a gravitational field, the instability of this vacuum results in particle production. In complex time WKB approximation (CWKB) technique, the aforementioned ideas find an elegant manifestation.

We have also studied catastrophic particle production under periodic perturbation through CWKB and find results consistent with other works. This allows us to study particle production in the light of CWKB to understand some aspects of cosmological evolution of the universe.

Appendix A

Among the three only one of the identities

$$\begin{aligned} S^{-1}\gamma_2(\partial_\theta + \tfrac{1}{2}\cot\theta)(S\psi) \\ &= -\tfrac{1}{2}(\gamma_1 \sin\theta\cos\varphi + \gamma_2 \sin\theta\sin\varphi + \gamma_3\cos\theta)\psi \\ &\quad + \tfrac{1}{2}\cot\theta(\gamma_1\cos\theta\cos\varphi + \gamma_2\cos\theta\sin\varphi - \gamma_3\sin\theta)\psi \\ &\quad + (\gamma_1\cos\theta\cos\varphi + \gamma_2\cos\theta\sin\varphi - \gamma_3\sin\theta)\partial_\theta\psi, \end{aligned} \tag{A1}$$

is shown in detail here and others follow the same rules.

Here we strictly follow

$$\bar{\psi} = S\psi$$

and

$$S = \tfrac{1}{2}(\gamma_1\gamma_2 + \gamma_2\gamma_3 + \gamma_3\gamma_1 + 1)e^{-(\theta/2)\gamma_3\gamma_1}e^{-(\varphi/2)\gamma_1\gamma_2}.$$

Then the left hand side of equation (A1) may be written as

$$S^{-1}\gamma_2(\partial_\theta + \tfrac{1}{2}\cot\theta)(S\psi) = (S^{-1}\gamma_2 S\partial_\theta + S^{-1}\gamma_2(\partial_\theta S) + \tfrac{1}{2}\cot\theta S^{-1}\gamma_2 S)\psi. \tag{A2}$$

Here

$$\begin{aligned} S^{-1}\gamma_2 S &= \tfrac{1}{4}e^{(\varphi/2)\gamma_1\gamma_2}e^{(\theta/2)\gamma_3\gamma_1}(1 - \gamma_1\gamma_2 - \gamma_2\gamma_3 - \gamma_3\gamma_1)\gamma_2 \\ &\quad \times (\gamma_1\gamma_2 + \gamma_2\gamma_3 + \gamma_3\gamma_1 + 1)e^{-(\theta/2)\gamma_3\gamma_1}e^{-(\varphi/2)\gamma_1\gamma_2} \\ &= \tfrac{1}{4}e^{(\varphi/2)\gamma_1\gamma_2}e^{(\theta/2)\gamma_3\gamma_1}(1 - \gamma_1\gamma_2 - \gamma_2\gamma_3 - \gamma_3\gamma_1) \\ &\quad \times (\gamma_1 - \gamma_3 + \gamma_1\gamma_2\gamma_3 + \gamma_2)e^{-(\theta/2)\gamma_3\gamma_1}e^{-(\varphi/2)\gamma_1\gamma_2} \\ &= \tfrac{1}{4}e^{(\varphi/2)\gamma_1\gamma_2}e^{(\theta/2)\gamma_3\gamma_1}(\gamma_1 - \gamma_3 + \gamma_1\gamma_2\gamma_3 + \gamma_2 - \gamma_2 + \gamma_1\gamma_2\gamma_3 + \gamma_3 + \gamma_1 \\ &\quad - \gamma_1\gamma_2\gamma_3 - \gamma_2 + \gamma_1 - \gamma_3 + \gamma_3 + \gamma_1 + \gamma_2 - \gamma_1\gamma_2\gamma_3)e^{-(\theta/2)\gamma_3\gamma_1}e^{-(\varphi/2)\gamma_1\gamma_2} \\ &= \frac{1}{4}\cdot 4e^{(\varphi/2)\gamma_1\gamma_2}e^{(\theta/2)\gamma_3\gamma_1}\gamma_1\left(\cos\frac{\theta}{2} - \gamma_3\gamma_1\sin\frac{\theta}{2}\right)e^{-(\varphi/2)\gamma_1\gamma_2} \\ &= e^{(\varphi/2)\gamma_1\gamma_2}\left(\cos\frac{\theta}{2} + \gamma_3\gamma_1\sin\frac{\theta}{2}\right)\left(\gamma_1\cos\frac{\theta}{2} - \gamma_3\sin\frac{\theta}{2}\right)e^{-(\varphi/2)\gamma_1\gamma_2} \end{aligned}$$

$$
\begin{aligned}
&= e^{(\varphi/2)\gamma_1\gamma_2}(\gamma_1\cos\theta-\gamma_3\sin\theta)\left(\cos\frac{\varphi}{2}-\gamma_1\gamma_2\sin\frac{\varphi}{2}\right)\\
&= \left(\cos\frac{\varphi}{2}+\gamma_1\gamma_2\sin\frac{\varphi}{2}\right)\left\{(\gamma_1\cos\theta-\gamma_3\sin\theta)\cos\frac{\varphi}{2}\right.\\
&\quad \left.+(\gamma_2\cos\theta+\gamma_1\gamma_2\gamma_3\sin\theta)\sin\frac{\varphi}{2}\right\}\\
&= \gamma_1\cos\theta\cos\varphi-\gamma_3\sin\theta+\gamma_2\cos\theta\sin\varphi, \qquad \text{(A3)}
\end{aligned}
$$

$$
\begin{aligned}
S^{-1}\gamma_2(\partial_\theta S) &= \frac{1}{2}S^{-1}\gamma_2(\gamma_1\gamma_2+\gamma_2\gamma_3+\gamma_3\gamma_1+1)\partial_\theta\left(\cos\frac{\theta}{2}-\gamma_3\gamma_1\sin\frac{\theta}{2}\right)e^{-(\varphi/2)\gamma_1\gamma_2}\\
&= \frac{1}{4}e^{(\varphi/2)\gamma_1\gamma_2}e^{(\theta/2)\gamma_3\gamma_1}(1-\gamma_1\gamma_2-\gamma_2\gamma_3-\gamma_3\gamma_1)\gamma_2\\
&\quad\times(\gamma_1\gamma_2+\gamma_2\gamma_3+\gamma_3\gamma_1+1)\left(-\frac{1}{2}\sin\frac{\theta}{2}-\frac{1}{2}\gamma_3\gamma_1\cos\frac{\theta}{2}\right)e^{-(\varphi/2)\gamma_1\gamma_2}\\
&= -\frac{1}{8}4e^{(\varphi/2)\gamma_1\gamma_2}\left(\cos\frac{\theta}{2}+\gamma_3\gamma_1\sin\frac{\theta}{2}\right)\left(\gamma_1\sin\frac{\theta}{2}+\gamma_3\cos\frac{\theta}{2}\right)e^{-(\varphi/2)\gamma_1\gamma_2}\\
&= -\frac{1}{2}e^{(\varphi/2)\gamma_1\gamma_2}(\gamma_3\cos\theta+\gamma_1\sin\theta)\left(\cos\frac{\varphi}{2}-\gamma_1\gamma_2\sin\frac{\varphi}{2}\right)\\
&= -\frac{1}{2}\left(\cos\frac{\varphi}{2}+\gamma_1\gamma_2\sin\frac{\varphi}{2}\right)\left\{(\gamma_3\cos\theta+\gamma_3\sin\theta)\cos\frac{\varphi}{2}\right.\\
&\quad\left.+(-\gamma_1\gamma_2\gamma_3\cos\theta+\gamma_2\sin\theta)\sin\frac{\varphi}{2}\right\}\\
&= -\tfrac{1}{2}(\gamma_3\cos\theta+\gamma_1\sin\theta\cos\varphi+\gamma_2\sin\theta\sin\varphi), \qquad \text{(A4)}
\end{aligned}
$$

$$
\tfrac{1}{2}\cot\theta S^{-1}\gamma_2 S=\tfrac{1}{2}\cot\theta(\gamma_1\cos\theta\cos\varphi-\gamma_3\sin\theta+\gamma_2\cos\theta\sin\varphi). \qquad \text{(A5)}
$$

Using equations (A3), (A4) and (A5) in equation (A2) give the required result of equation (36).

Appendix B

The unitary transformation (34) maps equation (32) into (28) which has to be proved here.

From equations (29) and (31) we get

$$
\dot a(t)=\frac{1}{2}\dot\alpha(\tau),\quad \partial_\tau+\frac{3}{4}\dot\alpha(\tau)=e^{(1/2)\alpha(\tau)}\left(\partial_t+\frac{3}{2}\frac{\dot a}{a}\right)\quad\text{and}\quad \partial_\chi+\frac{\xi'}{\xi}=\rho\partial_r+\frac{\rho}{r}.
$$

Using these with $\alpha_i=\gamma_0\gamma_i$ and the identities of equation (36), equation (32a) becomes

$$
\begin{aligned}
&\left[e^{(1/2)\alpha(\tau)}\left(\partial_t+\frac{3}{2}\frac{\dot a}{a}\right)-\gamma_0\left\{(\gamma_1\sin\theta\cos\varphi+\gamma_2\sin\theta\sin\varphi+\gamma_3\cos\theta)\left(\rho\partial_r+\frac{\rho}{r}\right)\right.\right.\\
&\quad-\frac{1}{2r}(\gamma_1\sin\theta\cos\varphi+\gamma_2\sin\theta\sin\varphi+\gamma_3\cos\theta)\\
&\quad+\frac{1}{2r}\left(\gamma_1\frac{\cos^2\theta}{\sin\theta}\cos\varphi+\gamma_2\frac{\cos^2\theta}{\sin\theta}\sin\varphi-\gamma_3\cos\theta\right)
\end{aligned}
$$

$$+\frac{1}{r\sin\theta}(-\gamma_1\sin\varphi+\gamma_2\cos\varphi)\partial_\varphi\Bigg\}+im\gamma_0\mathrm{e}^{(1/2)\alpha(\tau)}\Bigg]\psi=0$$

or

$$\begin{aligned}
&\Bigg[\partial_t+\frac{3}{2}\frac{\dot{a}}{a}-\frac{\gamma_0}{a}\Bigg\{(\gamma_1\sin\theta\cos\varphi+\gamma_2\sin\theta\sin\varphi+\gamma_3\cos\theta)\left(\rho\partial_r+\frac{\rho}{r}\right)\\
&\quad-\frac{1}{r}(\gamma_1\sin\theta\cos\varphi+\gamma_2\sin\theta\sin\varphi+\gamma_3\cos\theta)\\
&\quad+\frac{1}{r}(\gamma_1\cos\theta\cos\varphi+\gamma_2\cos\theta\sin\varphi-\gamma_3\sin\theta)\partial_\theta\\
&\quad+\frac{1}{r\sin\theta}(-\gamma_1\sin\varphi+\gamma_2\cos\varphi)\partial_\varphi\Bigg\}+im\gamma_0\Bigg]\psi=0.
\end{aligned}$$

This equation becomes, after using the transformation (26),

$$\left[\partial_t+\frac{3}{2}\frac{\dot{a}}{a}+im\gamma_0-\frac{\gamma_0}{a}\left\{\gamma_r\left(\rho\partial_r+\frac{\rho}{r}\right)-\frac{1}{r}\gamma_r+\frac{1}{r}\gamma_\theta\partial_\theta+\frac{1}{r\sin\theta}\gamma_\varphi\partial_\varphi\right\}\right]\psi=0,$$

$$\left[\partial_t+\frac{3}{2}\frac{\dot{a}}{a}+im\gamma_0-\frac{1}{a}\left\{\alpha_r\partial_r+\alpha_\theta\frac{1}{r}\partial_\theta+\alpha_\varphi\frac{1}{r\sin\theta}\partial_\varphi+(\rho-1)\alpha_r\left(\partial_r+\frac{1}{r}\right)\right\}\right]\psi=0,$$

$$\left[\partial_t+\frac{3}{2}\frac{\dot{a}}{a}+im\gamma_0-\frac{1}{a}\left\{\alpha\cdot\nabla+(\rho-1)\alpha_r\left(\partial_r+\frac{1}{r}\right)\right\}\right]\psi=0$$

and thus the result.

Appendix C

We determine the turning points, using eq. (98), from

$$\Omega(\eta_{1,2})=0. \tag{C1}$$

Defining

$$S(\eta_i,\eta_f)=\int_{n_i}^{n_f}\Omega(\eta)\mathrm{d}\eta \tag{C2}$$

and

$$S(\eta_i)=\left[\int\Omega(\eta)\mathrm{d}\eta\right]_{\eta=\eta_i}, \tag{C3}$$

the boundary condition takes the form

$$\psi\underset{\eta\to-\infty}{\sim}\exp\left[iS(\eta,\eta_1)\right], \tag{C4}$$

$$\psi \underset{\eta \to \infty}{\widetilde{\quad}} \exp[iS(\eta,\eta_1)] - iR\exp[-iS(\eta,\eta_1)], \tag{C5}$$

where R is the reflection amplitude. In eqs (C4) and (C5) η is real but the turning points are complex. In CWKB the reflection amplitude is identified as the pair production amplitude. The CWKB solution of eq. (97) is

$$\psi \xrightarrow[\eta \to \infty]{} e^{iS(\eta,\eta_0)} - ie^{iS(\eta_1,\eta_0)-iS(\eta,\eta_1)} \sum_{\mu=0} [-ie^{iS(\eta_1,\eta_2)}]^{2\mu}, \tag{C6}$$

where η is real and η_0 is real, arbitrary and $\eta_0 > \eta$. In (C6), the first term represent a wave starting at η_0 and moving left reaches real $\eta < \eta_0$. The second term takes the contribution of the reflected part as follows. A wave starting at η_0 reaches the complex turning point η_1 and after bouncing back from η_1 reaches η. This is represented as

$$(-i)\exp[iS(\eta_1,\eta_0) - iS(\eta,\eta_1)]. \tag{C7}$$

This contribution (C7) to the second term of (C6) is then multiplied by the repeated reflections between η_1 and η_2 and so comes the following factor in the second term of (C6), namely

$$\sum_{\mu=0} [-i\exp\{iS(\eta_1,\eta_2)\}]^{2\mu} = \frac{1}{1+e^{2iS(\eta_1,\eta_2)}}. \tag{C8}$$

For convenience we have neglected the WKB pre-exponential all through. Comparing (C6) with the boundary condition (C5) we have

$$R = \frac{\exp[2iS(\eta_1)]}{1+\exp[2iS(\eta_1,\eta_2)]}. \tag{C9}$$

If we consider $\exp[iS(\eta,\eta_0)]$ as antiparticle solution then (C6) is interpreted as the reflection of antiparticle from the turning point η_1 and the reflected part is interpreted as particle moving forward in time. This is Klein paradox-like situation not in space but in time.

References

[1] V Fock, *Z. Phys.* **53**, 592 (1928)
[2] H Tetrode, *Z. Phys.* **50**, 336 (1928)
[3] E Schrödinger, *Preuss. Akad. Wiss. Berlin* **11–12**, 105 (1932)
[4] G C McVittie, *Mon. Not. R. Astron. Soc.* **92**, 868 (1932)
[5] D R Brill and J A Wheeler, *Rev. Mod. Phys.* **29**, 465 (1957)
[6] L P Chimento and M S Mollerach, *Phys. Rev.* **D34**, 3689 (1986)
[7] J Audretsch and G Schäfer, *J. Phys.* **A11**, 1583 (1978)
[8] M A Castagnino and F D Mazzitelli, *Phys. Rev.* **D31**, 742 (1985)
[9] S Biswas and J Guha, *Pramana–J. Phys.* **40(6)**, 467 (1993)
[10] S Biswas, J Guha and N G Sarkar, *Class. Quantum Gravit.* **12**, 1591 (1995)
[11] J Guha, D Biswas, N G Sarkar and S Biswas, *Class. Quantum Gravit.* **12**, 1641 (1995)
[12] S Biswas, J Guha and N G Sarkar, *Pramana–J. Phys.* **42(4)**, 319 (1994)
[13] K H Lotze, *Class. Quant. Gravit.* **3**, 81 (1986)
[14] A O Barut and I H Duru, *Phys. Rev.* **D36**, 3705 (1987)

[15] S Biswas, J Guha and P Dasgupta, *Int. J. Mod. Phys.* **A10**, (1995)
[16] V Sahni, *Class. Quant. Gravit.* **1**, 579 (1984)
[17] A O Barut and L P Singh, *Exact solution of the Dirac equation in spatially non-flat RW spacetime II*, ICTP, IC/90/205 (1990)
[18] J M Cornwall and G Tiktopoulos, *Phys. Rev.* **D39**, 334 (1989)
[19] L Parker, *Phys. Rev.* **183**, 1057 (1969)
[20] M V Fischetti, J B Hartle and B L Hu, *Phys. Rev.* **D20**, 1757 (1979)
[21] P Anderson, *Phys. Rev.* **D28**, 271 (1983)
[22] L H Ford, *Phys. Rev.* **D22**, 3003 (1980b)
[23] L Kofman, A Linde and A A Starobinsky, *Phys. Rev. Lett.* **73**, 3195 (1994)
[24] D Boyanovsky, M D'Attanasio, H J de Vega, R Holman, D S Lee and A Singh, Report No. PITT-09–95 (unpublished); *Phys. Rev.* **D51**, 4419 (1995) and references therein
[25] M Yoshimura, *Prog. Theor. Phys.* **94**, 873 (1995)
[26] H Fujisaki, K Kumekawa, M Yumaguchi and M Yoshimura, *Phys. Rev.* **D53**, 6805 (1996)
[27] M A Castagnino and L Chimento, *Phys. Rev.* **D34**, 3676 (1986)
[28] M A Castagnino, E Gunzig, P Nardone and J P Paz, *Phys. Rev.* **D34**, 3698 (1986)
[29] F D Mazettelli, J P Paz and M A Castagnino, *Phys. Rev.* **D34**, 2994 (1987)
[30] V Sahni, *Phys. Lett.* **A86**, 87 (1981)
[31] N D Birrell and P C W Davies, *Quantum fields in curved space* (Cambridge University Press, 1982)
[32] J Knoll and R Schaeffer, *Ann. Phys.* **97**, 307 (1976)
[33] J Knoll and R Schaeffer, *Phys. Rep.* **31**, 159 (1977)
[34] F Schrempp and B Schrempp, *Nucl. Phys.* **B163**, 397 (1980)
[35] T Padmanaban, *Ann. Phys. (NY)* **141**, 316 (1982)

physics

February 1998
pp. 133–148

Finite temperature Cornwall–Jackiw–Tomboulis formalism of Φ^6 theory

K P SATHEESH and K BABU JOSEPH
Department of Physics, Cochin University of Science and Technology, Kochi 682 002, India

MS received 24 July 1997

Abstract. The finite temperature effective potential for a scalar field with Φ^6 interaction is calculated by extending the CJT formalism for composite operators. It is found that unrenormalized terms appear in the effective potential due to the presence of an unrenormalized mass term. Nonzero turning points are obtained both for positive and negative λ. High temperature expansion is performed and the results are analysed numerically. Graphical analysis indicates symmetry restoration when $T \to 0$.

Keywords. Composite operator; double Legendre transform; CJT formalism; effective potential; finite temperature; symmetry restoration; high temperature expansion.

PACS Nos 11.10; 11.15

1. Introduction

Study of symmetry changing phase transitions of a quantum field in the presence of a surrounding thermal bath is very important in the study of the evolution of the universe and in the analysis of very high energy collisions where very high matter and radiation density exist. Detailed study of these phase transitions has been done by various authors [1–4]. The effective potential method is very useful in studying spontaneous symmetry breaking (SSB) at zero temperature [5, 6]. Estimation of the critical temperature of phase transitions can be done by extending this approach to finite temperature. These studies mainly using loop expansion techniques have played a pivotal role in framing our understanding about the early universe, unified theories, quark gluon plasma etc.

Recently there has been a revival of interest in finite temperature quantum field theory, apparently caused by the recognition of the importance of symmetry breaking phase transitions and the problem of precise determination of critical temperature. An accurate analysis of phase transitions (both analytical and numerical) becomes necessary because most of the cosmological models critically depend on it. For example baryon asymmetry may be generated at the electro-weak level if the phase transition is of first order [7–10]. For calculation of critical temperature various perturbative and non-perturbative techniques have been suggested [11–19].

Effective potential defined as single Legendre transform provides an efficient way to obtain quantum corrections to the classical potential. But this popular method suffers from a serious shortcoming. Since it is defined as a single Legendre transform, it is always a convex function. This forbids the double well shape for the exact effective potential and implies the absence of local maximum at the symmetric origin. But in a theory possessing SSB classical analysis predicts a maximum at the origin. Various procedures to avoid this difficulty have been suggested earlier [3, 20, 21]. One of the most efficient of these approaches is to define an effective action by including a source $K(x,y)$ coupled to a term which is quadratic in the field variable. By this procedure an effective potential with a proper loop expansion to each order which is not convex, is obtained. This idea was first put forward by Hawking and Moss in the context of quantum field theory in the early universe [22]. A self-consistent improvement for the finite temperature effective potential has also been suggested [23]. In this formalism it is possible to sum a large class of ordinary perturbation theory diagrams that contribute to the effective action and the gap equation which determines the form of the propagator, is obtained by variational method.

All the above improvements developed for conventional finite temperature effective potential are based on an important contribution by Cornwall, Jackiw and Tomboulis (CJT). They defined the effective action for composite fields in flat space and zero temperature as a double Legendre transform with two sources $J(x)$ and $K(x,y)$. These two sources are coupled respectively to $\phi(x)$ and $\phi(y)$ [24]. The CJT formalism is considered to be best suited for studying phase transitions because it uses a generalized effective action in which not only the mean field but also the correlation functions appear as independent variables. A simple series expansion has been developed for this improved effective action [24].

The CJT formalism has recently been used to resolve various difficulties in quantum field theory [25, 26]. For example, it has been applied to the triviality problem in Φ^4 theory [27]. An improved effective potential based on this formalism has also been developed [28]. The self-consistent improvement of finite temperature effective potential involves the summation of daisy and superdaisy diagrams, for which a novel resummation procedure has been recently proposed [29].

Recently, there has been considerable interest in the application of functional techniques in field theories with dimensions less than $(3+1)$, mainly because some of the problems afflicting 4-dimensional theories are absent there [30–32]. According to Coleman's theorem, spontaneous symmetry breaking can occur only when the dimensions are higher than $(1+1)$. In $(2+1)$ dimensions the most general renormalizable theory is for a Φ^6 model. This model has been studied earlier by using various methods and it has been shown that it possesses an ultraviolet fixed point in $1/N$ expansion and Gaussian approximation [33–35]. Finite temperature field theory has also been analysed [17, 18]. It is well known that in finite temperature CJT analysis of Φ^4 theory, the effective potential shows a cut-off dependence due to the presence of a $(\lambda\phi^4/12)$ term. It is natural to think that in lower dimensions where coupling constant renormalization is not required this difficulty will not be there. Even though this is found to be true for Φ^4 theory in $(2+1)$ dimensions, an unrenormalized mass term appears in the expression for effective potential for Φ^6 theory. Thus the diffiiculty persists in a disguised form, in $(2+1)$ dimensional Φ^6 theory.

2. CJT formalism

The CJT method provides a generalization of the ordinary effective action $\Gamma(\phi)$ (the generating functional for single particle irreducible n-point functions). This generalized effective action $\Gamma(\phi, G)$ depends both on $\phi(x)$ the expectation value of quantum field $\Phi(x)$, and $G(x,y)$ the expectation value of time ordered product $T\langle\Phi(x)\Phi(y)\rangle$. Physical (on-shell) solutions require the following variational equations:

$$\frac{\delta\Gamma(\phi, G)}{\delta\phi(x)} = 0, \tag{1}$$

$$\frac{\delta\Gamma(\phi, G)}{\delta G(x,y)} = 0. \tag{2}$$

Consider the vacuum persistence amplitude $Z(J,K)$ in the presence of two source terms $J(x)\phi(x)$ and $\frac{1}{2}\phi(x)\phi(y)K(x,y)$:

$$Z(J,K) \equiv N\int \mathcal{D}\Phi \exp\left[i\int \mathrm{d}^4x\left[\mathcal{L}[\Phi(x)] + J(x)\Phi(x) + \frac{1}{2}\Phi(x)K(x,y)\Phi(y)\right]\right]. \tag{3}$$

$W(J,K)$, the generating functional for connected diagrams is defined as

$$Z(J,K) \equiv \exp[iW(J,K)]. \tag{4}$$

The classical action $I(\Phi) = \int \mathrm{d}^4x\mathcal{L}(x)$ may be written as

$$I(\phi) = \int \mathrm{d}^4x\mathrm{d}^4y\phi(x)D_0^{-1}(x-y)\phi(y) + I_{\mathrm{int}}(\phi) \tag{5}$$

$$I_{\mathrm{int}}(\phi) = \int \mathrm{d}^4x\mathcal{L}_{\mathrm{int}}(x). \tag{6}$$

$D_0(x-y)$ is the free propagator that satisfies

$$D_0^{-1}(x-y) = -(\Box + 2)\delta^4(x-y). \tag{7}$$

The generalized effective action $\Gamma(\phi, G)$ is the double Legendre transform of $W(J,K)$,

$$\begin{aligned}\Gamma(\Phi, G) =& W(J,K) - \int \mathrm{d}^4(x)\Phi(x)J(x) - \frac{1}{2}\int \mathrm{d}^4x\mathrm{d}^4y[\Phi(x)K(x,y)\Phi(y)]\\ &- \frac{1}{2}\int \mathrm{d}^4x\mathrm{d}^4yG(x,y)K(x,y),\end{aligned} \tag{8}$$

where $J(x)$ and $K(x,y)$ are determined by

$$\frac{\delta W(J,K)}{\delta J(x)} = \phi(x), \tag{9}$$

$$\frac{\delta W(J,K)}{\delta K(x,y)} = \frac{1}{2}[\phi(x)\phi(y) + G(x,y)]. \tag{10}$$

By actually performing functional differentiation on (8) we find

$$\frac{\delta\Gamma(\phi, G)}{\delta\phi(x)} = -J(x) - \int \mathrm{d}^4 y K(x,y)\phi(y), \tag{11}$$

$$\frac{\delta\Gamma(\phi, G)}{\delta G(x,y)} = -\frac{1}{2}K(x,y). \tag{12}$$

In the absence of sources, (1) and (2) are regained which permit a variational solution. The conventional effective action $\Gamma(\phi) = \Gamma(\phi, G_0)$ where G_0 is the solution of (2). Generalized effective action $\Gamma(\phi, G)$ is the generating functional for the two particle irreducible (2PI) Greens functions expressed in terms of the full propagator. The series expansion for $\Gamma(\phi, G)$ is shown to be [24]

$$\Gamma(\phi, G) = I_{\text{class}}\cdot(\phi) + \tfrac{1}{2}\mathrm{tr}\ln D_0 G^{-1} + \tfrac{1}{2}\mathrm{tr}[D^{-1}G - 1] + \Gamma^{(2)}(\phi, G), \tag{13}$$

where 'tr' is the functional trace 'ln' is the functional logarithm and $D^{-1}G$ is the functional product. The inverse propagator is defined as the functional second derivative of action:

$$D^{-1}(\phi; x,y) = \frac{\delta^2 I(\phi)}{\delta\phi(x)\delta\phi(y)} = D^{-1}(x-y) + \frac{\delta^2 I_{\text{int}}(\phi)}{\delta\phi(x)\delta\phi(y)}. \tag{14}$$

Computation of the quantity $\Gamma^{(2)}(\phi, G)$ is done as follows. In the classical action $I(\Phi)$, the field Φ is shifted by $\phi(x)$. The shifted action $I(\Phi + \phi)$, possesses terms cubic and higher in Φ. These define as interaction part I_{int} with vertices depending on $\phi(x)$. $\Gamma^{(2)}(\phi, G)$ is then given by all the 2PI vacuum graphs and the propagator is set equal to $G(x,y)$. The theory in its full generality is not translationally invariant since vertices depend on $\phi(x)$ and G is not a function of $(x-y)$ alone. The propagator of the theory is determined by finding the gap equation for G using the variation equations [eqs (1) and (2)].

3. Effective potential

Translationally invariant solutions are obtained by imposing the following conditions (homogeneous states):

$$\phi(x) = \text{Constant}, \tag{15}$$

$$G(x,y) = G(x-y), \tag{16}$$

$$\Gamma(\phi, G) = -E(\phi, G)\int \mathrm{d}t, \tag{17}$$

where $E(\phi, G)$ is the minimum of the energy when varying over all the normalized states with constraints:

$$\langle\Phi(x)\rangle = \phi(x), \tag{18}$$

$$\langle\Phi(x)\Phi(y)\rangle = \phi(x)\phi(y) + G(x,y), \tag{19}$$

$$E(\phi, G) = V(\phi, G)\int \mathrm{d}^{\nu-1}x, \tag{20}$$

where ν is the space-time dimension of the theory. Thus the effective potential is given by

$$V(\phi, G) = -\frac{\Gamma(\phi, G)}{\int \mathrm{d}^{\nu}x}. \tag{21}$$

A series expansion for the effective potential is obtained by defining the following Fourier transformed propagators

$$G(k) = \int \mathrm{d}^{\nu}x \mathrm{e}^{ik(x-y)} G(x-y), \tag{22}$$

$$D(\phi, k) = \int \mathrm{d}^{\nu}x \mathrm{e}^{ik(x-y)} D(\phi; x-y), \tag{23}$$

$$D_0(k) = \int \mathrm{d}^{\nu}x \mathrm{e}^{ik(x-y)} D_0(x-y), \tag{24}$$

$$\begin{aligned} V(\phi, G) = {} & U(\phi) + \frac{1}{2}\int \frac{\mathrm{d}^{\nu}x}{2\pi} \ln \det D_0(k) G^{-1}(k) \\ & + \frac{1}{2}\int \frac{\mathrm{d}^{\nu}k}{(2\pi)^{\nu}} \operatorname{tr}\left[D^{-1}(\phi, k) G^{-1}k - 1\right] + V_{(2)}(\phi, G), \end{aligned} \tag{25}$$

where $U(\phi)$ is the classical potential, $V_{(2)}(\phi, G)$ is the sum of 2PI vacuum graphs, with vertices given by $I_{\mathrm{int}}(\phi, \Phi)$ and the propagator is set equal to $G(k)$. The field ϕ on which vertices depend is now a constant parameter. Trace and logarithms apply to component fields and determinants are no more functional.

To describe the theory at finite temperature we use the Euclidean time τ satisfying the boundary conditions $0 \leq \tau \leq \beta \equiv 1/T$. All the Feynman diagrams (2PI diagrams) developed at zero temperature are valid here also. The Feynman rules for writing the algebra of the diagrams are different at finite temperature [21]. They are

$$\omega_n = \frac{2\pi n}{\beta}, \tag{26}$$

$$\text{loop integral} \rightarrow \frac{1}{\beta}\sum_n \int \frac{\mathrm{d}^{\nu-1}k}{(2\pi)^{\nu-1}}, \tag{27}$$

$$\text{vertex delta function} \rightarrow \beta(2\pi)^{\nu-1}\delta \sum_{\omega_n} \delta^{\nu-1}\left(\sum_i k_i\right). \tag{28}$$

Field Φ satisfies the periodic boundary conditions

$$\Phi\left(-\frac{\beta}{2}, x\right) = \Phi\left(\frac{\beta}{2}, x\right). \tag{29}$$

With these modifications we can write the series expansion for finite temperature CJT effective potential (analog of Gibb's potential) with time integration suppressed and a summation performed

$$\int \frac{\mathrm{d}^{\nu}k}{(2\pi)^{\nu}} \rightarrow \frac{1}{\beta}\sum_n \int \frac{\mathrm{d}^{\nu-1}k}{(2\pi)^{\nu-1}}. \tag{30}$$

4. Φ^6 Theory

The classical potential of the theory is given by

$$U(\Phi) = \frac{1}{2} m_{\mathrm{B}}^2 \Phi^2 + \frac{\lambda_{\mathrm{B}}}{4!}\Phi^4 + \frac{\xi_{\mathrm{B}}}{6!}\Phi^6, \tag{31}$$

where λ and ξ represent coupling constants for Φ^4 and Φ^6 interactions respectively and the subscript B indicates bare parameters. The functional operator D^{-1} is given by

$$D^{-1}(\Phi; (x,y)) = -\left[\Box + m_{\mathrm{B}}^2 + \frac{\lambda_{\mathrm{B}}}{2}\Phi^2 + \frac{\xi_{\mathrm{B}}}{24}\right]\delta^{\nu}(x-y). \tag{32}$$

After shifting the field Φ to $(\Phi + \phi)$, the interaction Lagrangian takes the form

$$L_{\mathrm{int}}(\Phi, \phi) = \left[\frac{\lambda_{\mathrm{B}}}{6}\phi\Phi^3 + \frac{\lambda_{\mathrm{B}}}{4!}\Phi^6 + \frac{\xi_{\mathrm{B}}}{6!}\Phi^6 + \frac{\xi_{\mathrm{B}}}{5!}\phi\Phi^5 + \frac{\xi_{\mathrm{B}}}{48}\phi^2\Phi^4 + \frac{\xi_{\mathrm{B}}}{36}\phi^3\Phi^5\right]. \tag{33}$$

A few of the 2PI vacuum graphs up to three loops are shown in figure 1. We select only those graphs with vertices depending on first order in the coupling constant. This approximation (Hartree–Fock) corresponds to a systematic variational procedure and is superior to commonly used one-loop approximation. No graphs with internal lines appear. Daisy and superdaisy graphs shown in figure 3 are of this type. Thus only the graphs shown in figure 2 need be summed. The sum of the relevant 2PI graphs takes the form

$$\Gamma_{\beta}^{(2)}(\phi, G) = \frac{3}{4!}\lambda_{\mathrm{B}} \int \mathrm{d}^{\nu}x G(x,x)G(x,x) + \frac{10}{6!}\xi_{\mathrm{B}} \int \mathrm{d}^{\nu}x G(x,x)G(x,x)G(x,x). \tag{34}$$

The expression for the finite temperature nonlocal composite operator effective action in Hartree–Fock approximation becomes

$$\begin{aligned}\Gamma_{\beta}(\phi, G) = & I_{\mathrm{class}} + \frac{1}{2}\operatorname{tr}\ln D_0 G^{-1} + \frac{1}{2}\operatorname{tr}(D^{-1}G - 1) \\ & + \frac{3}{4!}\lambda_{\mathrm{B}} \int \mathrm{d}^{\nu}x G(x,x)G(x,x) + \frac{10}{6!}\xi_{\mathrm{B}} \int \mathrm{d}^{\nu}x G(x,x)G(x,x)G(x,x).\end{aligned} \tag{35}$$

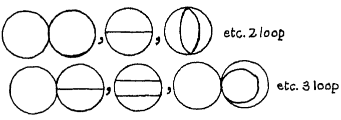

Figure 1. 2PI graphs for Φ^4 and Φ^6.

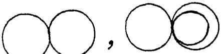

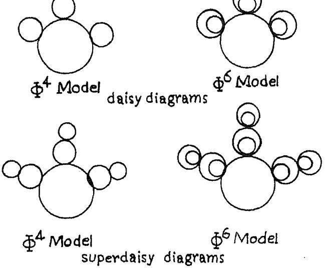

Figure 3. Daisy and superdaisy graphs for Φ^4 and Φ^6.

By performing variation with respect to G the modified gap equation is obtained as

$$G^{-1}(x,y) = D^{-1}(x,y) + \left[\frac{\lambda_{\mathrm{B}}}{2}G(x,x) + \frac{\xi_{\mathrm{B}}}{12}G(x,x)G(x,x)\right]\delta^3(x-y). \tag{36}$$

By iteration it can be seen that G generates all daisy and superdaisy graphs of figure 3, which reveals the fact that we have achieved a definite improvement in the resummation of diagrams.

Since we are interested only in translation invariant theories we fix an ansatz for G and define the Fourier transformed propagators [eqs (22), (23) and (24)]

$$G(k) \equiv \int \frac{\mathrm{d}^\nu x}{(2\pi)^\nu} G(x-y)\mathrm{e}^{ik(x-y)} = \frac{1}{k^2+M^2}, \tag{37}$$

$$D(k) \equiv \int \frac{\mathrm{d}^\nu x}{(2\pi)^\nu} D(x-y)\mathrm{e}^{ik(x-y)} = \frac{1}{k^2+m_{\mathrm{B}}^2+\frac{\lambda_{\mathrm{B}}}{2}\phi^2+\frac{\xi_{\mathrm{B}}}{24}\phi^4}. \tag{38}$$

Here the propagator is chosen in terms of an effective mass M which acts as a variational parameter. Effective potential in terms of M^2 and ϕ can be written using static configuration and constant background field

$$\begin{aligned} V_\beta(\phi,M) = {} & \left[\frac{1}{2}m_{\mathrm{B}}^2\phi^2 + \frac{\lambda_{\mathrm{B}}}{4!}\phi^4 + \frac{\xi_{\mathrm{B}}}{6!}\phi^6\right] + \frac{1}{2}\int\frac{\mathrm{d}^3k}{(2\pi)^3}\ln(k^2+M^2) \\ & - \frac{1}{2}\left[M^2 - m_{\mathrm{B}}^2 - \frac{\lambda_{\mathrm{B}}}{2}\phi^2 - \frac{\xi_{\mathrm{B}}}{24}\phi^4\right]G(x,x) + \frac{\lambda_{\mathrm{B}}}{8}G(x,x)G(x,x) \\ & + \frac{\xi_{\mathrm{B}}}{48}G(x,x)G(x,x)G(x,x). \end{aligned} \tag{39}$$

Putting $\xi_{\mathrm{B}} = 0$ we get Φ^4 theory in (2+1) dimensions. Comparing the expression obtained with the Gaussian effective potential studies [16] we see that both are formally similar. But as far as Φ^6 theory is concerned dissimilarities emerge because of the term $\xi\phi_0^2$. It is interesting to note that this factor is not contributed by the daisy or superdaisy diagrams, but by a graph with vertex not proportional to ξ. This graph is not considered in Hartree–Fock approximation.

Since the effective potential is an ordinary function (not a functional) stationary requirements with respect to ϕ and M^2 is obtained by ordinary differentiation

$$\frac{\partial V}{\partial \phi} = \phi\left[m_{\mathrm{B}}^2 + \frac{\lambda_{\mathrm{B}}}{6}\phi^2 + \frac{\xi_{\mathrm{B}}}{120}\phi^4 + \frac{\lambda_{\mathrm{B}}}{2}G(x,x) + \frac{\xi_{\mathrm{B}}}{12}\Phi^2 G(x,x)\right] = 0, \tag{40}$$

$$\frac{\partial V}{\partial M^2} = -\frac{1}{2}\left[M^2 - m_{\mathrm{B}}^2 - \frac{\lambda_{\mathrm{B}}}{2}\phi^2 - \frac{\xi_{\mathrm{B}}}{24}\phi^4 - \frac{\lambda_{\mathrm{B}}}{2}G(x,x) - \frac{\xi_{\mathrm{B}}}{8}G(x,x)G(x,x)\right]\frac{\partial G(x,x)}{\partial M^2} = 0. \tag{41}$$

Conventional effective potential is defined at the solution of (41). The effective mass is given by

$$M^2(\phi) = \left[m_{\mathrm{B}}^2 + \frac{\lambda_{\mathrm{B}}}{2}\phi^2 + \frac{\xi_{\mathrm{B}}}{24}\phi^4 + \frac{\lambda_{\mathrm{B}}}{2}G(x,x) + \frac{\xi_{\mathrm{B}}}{8}G(x,x)G(x,x)\right]. \tag{42}$$

Required expression for the effective potential is obtained by replacing the effective mass M by $M(\phi)$ in (39). Equation (39) shows certain very important peculiarities of Φ^6 and Φ^4 theories relevant at zero temperature

$$V'(\phi) = \phi\left[M^2(\phi) - \left(\frac{\lambda_{\mathrm{B}}}{3}\phi^2\right)\right]. \tag{43}$$

For Φ^4 theory $M^2(\phi)$ is intrinsically positive. Hence if $\lambda_{\mathrm{B}} < 0$ only solution to the above equation is $\phi = 0$ (or potential is unbounded from below). That is for negative λ_{B} non-zero turning points do not exist. In the case of Φ^6 theory

$$V'(\phi) = \phi\left[M^2(\phi) - \left(\frac{\lambda_{\mathrm{B}}}{3}\phi^2 + \frac{\xi_{\mathrm{B}}}{30}\phi^4\right)\right] - \frac{\xi}{4}\left[1 - \frac{\phi^2}{3}\right]G^2, \tag{44}$$

non-zero turning points are possible also for $\lambda_{\mathrm{B}} < 0$. Φ^6 theory in Hartee–Fock approximation requires up to three loops for obtaining the effects of ξ coupling. We have four parts for the effective potential

$$V_\beta(\phi, M(\phi)) = V^0 + V^1 + V^2 + V^3, \tag{45}$$

$$V^0 = \left[\frac{1}{2}m_{\mathrm{B}}^2\phi^2 + \frac{\lambda_{\mathrm{B}}}{4!}\phi^4 + \frac{\xi_{\mathrm{B}}}{6!}\phi^6\right], \tag{46}$$

$$V^1 = \frac{1}{2}\int \frac{\mathrm{d}^3k}{(2\pi)^3}\ln[k^2 + M^2(\phi)], \tag{47}$$

$$V^2 = -\frac{\lambda_{\mathrm{B}}}{8}G(x,x)G(x,x), \tag{48}$$

$$V^3 = -\frac{\xi_{\mathrm{B}}}{24}G(x,x)G(x,x)G(x,x), \tag{49}$$

which are obtained by substituting $M(\phi)$. Effective potential for both Φ^4 and Φ^6 theories

5. Renormalization

The effective mass term $M(\phi)$ defining the effective potential is divergent mainly due to the presence of $G(x,x)$. Following renormalization prescription is employed in $(2+1)$ dimensions to regularize $M(\phi)$ [6, 23]. Define

$$G(M(\phi)) \equiv -\frac{M(\phi)}{4\pi} + \frac{1}{\beta}\int \frac{\mathrm{d}^2k}{(2\pi)^2}\frac{1}{E(\mathrm{e}^{\beta E}-1)} \tag{50}$$

with

$$E \equiv [k^2 + M^2(\phi)]^{1/2}. \tag{51}$$

In $(2+1)$ dimensions coupling constant renormalization is not required. Define

$$m_r^2 \equiv m_\mathrm{B}^2 + \frac{1}{2}\lambda I_1 + \frac{\xi'}{4}I_1 + \frac{\xi}{8}I_1^2, \tag{52}$$

$$I_1 \equiv \int \frac{\mathrm{d}^2k}{(2\pi)^2}\frac{1}{2k} = \lim_{\Lambda\to\infty}\left(\frac{\Lambda}{4\pi}\right), \tag{53}$$

$\xi' \equiv \xi G(M(\phi))$. Using the summation procedure developed by Dolan and Jackiw [2, 23] the summation in time co-ordinate can be performed

$$G(x,x) = \int \frac{\mathrm{d}^2k}{(2\pi)^2}\frac{1}{2E} + \frac{1}{\beta}\int \frac{\mathrm{d}^2k}{(2\pi)^2}\frac{1}{E(\mathrm{e}^{\beta E}-1)}. \tag{54}$$

By actual evaluation, introducing a cut-off parameter Λ

$$G(x,x) = G(M(\phi)) + I_1. \tag{55}$$

Equation (54) shows that $G(M\phi))$ is the finite part of the vacuum propagator. A finite expression for $M(\Phi)$ is obtained by expressing it in terms of the renormalized parameters

$$M^2(\phi) = -m_r^2 + \frac{\lambda}{2}\phi^2 + \frac{\xi}{24}\phi^4 + \frac{\lambda}{2}G(M(\phi)) + \frac{\xi}{8}G(M(\phi))G(M(\phi)). \tag{56}$$

Second derivative of the tree level potential is defined as m_tree (tree level mass)

$$M^2(\phi) = m_\mathrm{tree}^2(\phi) + \frac{\lambda}{2}G(M(\phi)) + \frac{\xi}{8}G(M(\phi))G(M(\phi)), \tag{57}$$

$$V_\beta^1(M(\phi)) = -\frac{M^3}{6\pi} + \frac{1}{\beta}\int \frac{\mathrm{d}^2k}{(2\pi)^2}\ln(1-\mathrm{e}^{\beta E}) + \frac{\Lambda^3}{6\pi}. \tag{58}$$

At zero temperature the second term vanishes and the last term is cut-off dependent. Cancellation of this divergence is obtained by combining V^0, V^2 and V^3:

$$\begin{aligned} V_\beta(M) = &-\frac{M^3}{6\pi} + \frac{1}{\beta}\int \frac{\mathrm{d}^2k}{(2\pi)^2}\ln(1-\mathrm{e}^{\beta E}) + \frac{M^4}{2\lambda} \\ &-\frac{1}{2}M^2G(M) - \frac{M^2}{24\eta}G^2(M) - F(\phi), \end{aligned} \tag{59}$$

with

$$\eta^{-1} = \frac{\xi}{\lambda} \text{ and } F(\phi) = \left[\frac{m^2}{24\eta} - \frac{\lambda}{12} - \frac{29}{6!}\xi\phi^2\right]\phi^4. \tag{60}$$

$\xi = 0$ reproduces the result of Camellia and Pi. Using unrenormalized gap equation we combine V^0, V^2 and V^3 and writing them in terms of renormalized parameters

$$V^0 + V^2 + V^3 = \frac{\lambda_r}{8}\left[\phi^2 - \frac{2m_r^2}{\lambda}\right]^2 - \frac{\eta}{24}m_r^2\phi^4 - \frac{\lambda_r}{8}G^2(M) - \frac{\xi_r}{48}G^3(M) - F(\phi). \tag{61}$$

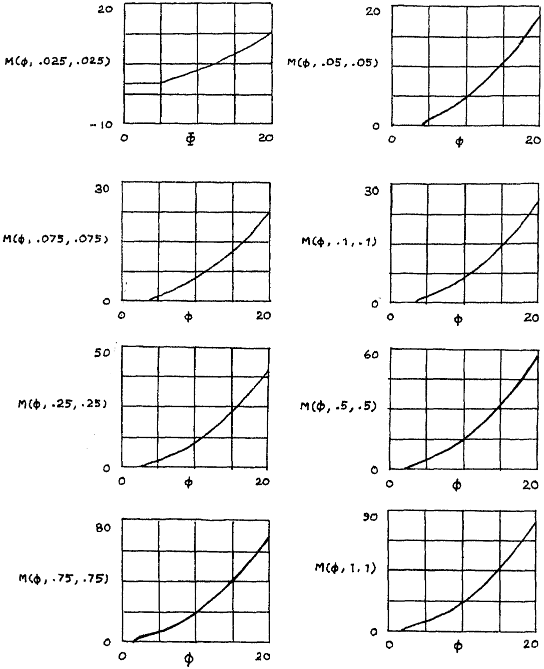

Figure 4. Effective mass for various couplin Φ^6 th

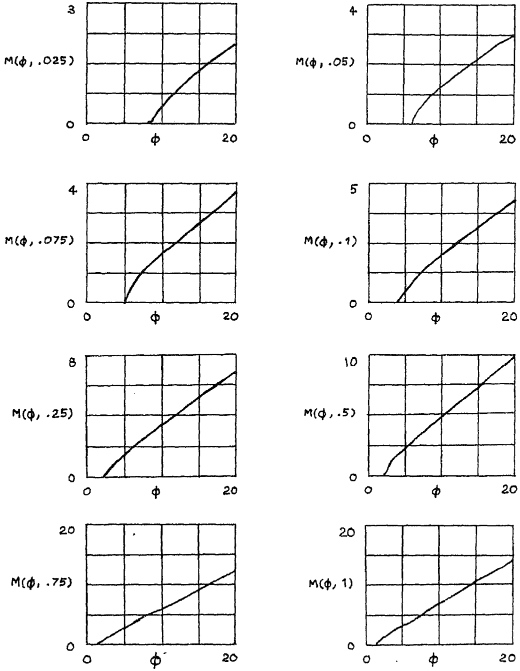

Figure 5. Effective mass for various couplings-Φ^4 theory.

In the case of $(2+1)$ dimensional Φ^4 theory $F(\phi) = \lambda/12$ which is finite. Thus unlike $(3+1)$ dimensional Φ^4 theory the effective potential does not contain any unrenormalized parameters. But in the case of Φ^6 theory $F(\phi)$ contains m which is an unrenormalized mass parameter. But here we can make $F(\phi) = 0$ by adjusting the parameters suitably and make the unrenormalized parameters vanish.

6. High temperature expansion

Evaluation of the effective potential at high temperature up to one loop level has been done earlier in $(3+1)$ and $(1+1)$ dimensions [2, 35]. Additional terms appearing in the

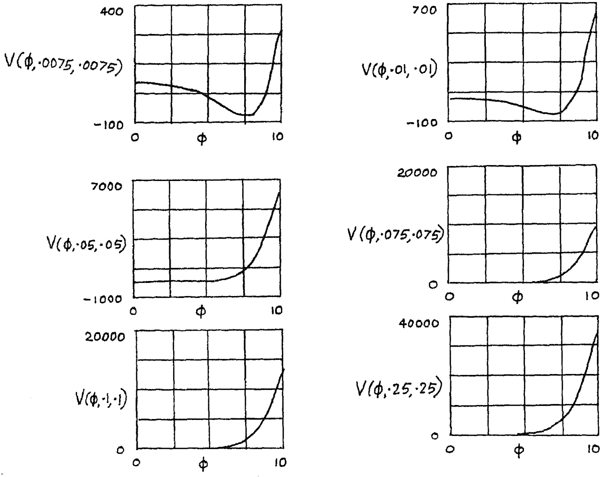

Figure 6. Effective potential for various couplings-Φ^6 theory.

xpression for the effective potential can be obtained by evaluating $G(M(\phi))$, for $M(\phi)/T \ll 1$. The relevant integral (eq. (50)) is of the form

$$h_n(y) = \frac{1}{\Gamma(n)} \int_0^\infty \frac{x^{n-1}\mathrm{d}x}{(x^2+y^2)^{(1/2)}} \frac{1}{\mathrm{e}^{(x^2+y^2)^{(1/2)}} - 1}, \tag{62}$$

$$y = \frac{m}{T}. \tag{63}$$

These integrals satisfy the differential equation

$$\frac{\mathrm{d}h_{n+1}}{\mathrm{d}y} = -\frac{y h_{n-1}}{n}. \tag{64}$$

High temperature expansion for the integral is obtained by using the identity

$$\frac{1}{\mathrm{e}^2 - 1} = \frac{1}{z} - \frac{1}{2} + 2\sum_{l=1}^{\infty} \frac{z}{z^2 + (2\pi l)^2}. \tag{65}$$

Multiplying the integrand by a factor $x^{-\epsilon}$ for convergence, performing term by term ntegration and letting $\epsilon \to 0$ at the end we get

$$h_1(y) = \frac{\pi}{2y} + \frac{1}{2}\ln\frac{y}{4\pi} + \frac{1}{2}\gamma + O(y^2). \tag{66}$$

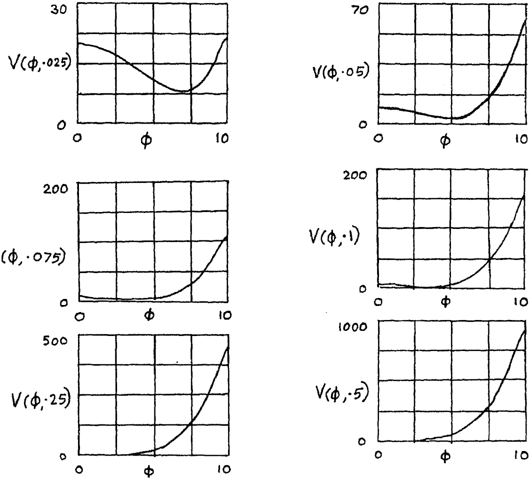

Figure 7. Effective potential for various couplings-Φ^4 theory.

$\gamma = 0.5772\ldots$ which is the Euler constant.

$$h_2(y) = -\ln(1 - \mathrm{e}^{-\nu}). \tag{67}$$

Other values of h can be found by using the differential equation (64). We have

$$\frac{1}{\beta}\int \frac{\mathrm{d}^2k}{(2\pi)^2}\,\frac{1}{E(\mathrm{e}^{\beta E}-1)} = \frac{1}{\pi}\int \frac{k\mathrm{d}k}{(2\pi)^2}\frac{1}{E(\mathrm{e}^{\beta E}-1)}. \tag{68}$$

By using the formula (67) we get

$$G(M(\phi)) = -\frac{M(\phi)}{4\pi} + \frac{1}{\pi}\ln(1 - \mathrm{e}^{-M/T}) \tag{69}$$

which can be used to evaluate V_{eff} at high temperature using (60). High temperature expansion for the effective mass can be obtained from (56).

7. Conclusions

A self-consistent improvement for the finite temperature Φ^6 theory is obtained as an extension of CJT formalism. Certain peculiarities of the Φ^6 field theory in $(2+1)$ dimensions are analysed. Φ^4 theory in $(2+1)$ dimensions does not contain any

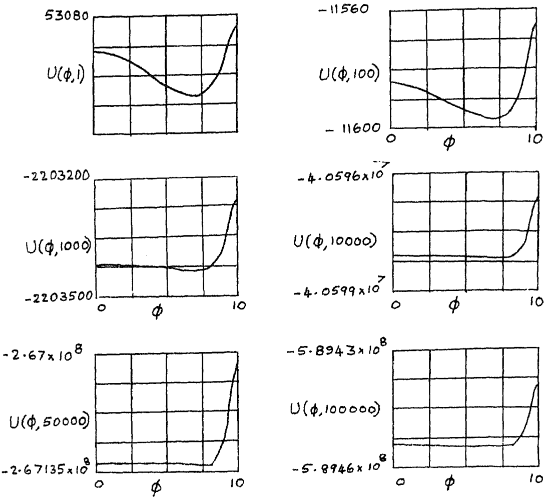

Figure 8. Effective potential at various temperatures-Φ^6 theory.

unrenormalized terms unlike its $(3+1)$ dimensional counterpart. Φ^6 theory in $(2+1)$ dimensions contains divergent terms in the form of an unrenormalized mass parameter in the expression for effective potential, but can be made to vanish. In this model physically meaningful stable theory is possible both for positive and negative λ, indicating the possibility of bound states. High temperature expansion for the effective potential is obtained.

Behavior of the effective mass can be clearly understood by numerically solving the equation for effective mass. Figures 4 and 5 show these graphs for certain relevant values at zero temperature for Φ^4 and Φ^6 theories. The straight region parallel to the ϕ axis indicates imaginary values of the effective mass. It is clear that this region indicates a broken symmetry phase. Comparison between Φ^4 and Φ^6 theories shows that they are identical in shape except for higher numerical values for Φ^6 model. A study of the behaviour of effective potential (figures 6 and 7) for different couplings is also given (in weak coupling range since the reliability of the approximation in the strong coupling range is not well established). Shape of the graph is same for a reasonable range of couplings with a notable difference in the stretch of the straight region.

Graph for effective potential at finite temperature (figures 8 and 9) shows that as temperature increases the minimum gradually dissappears indicating an approach to

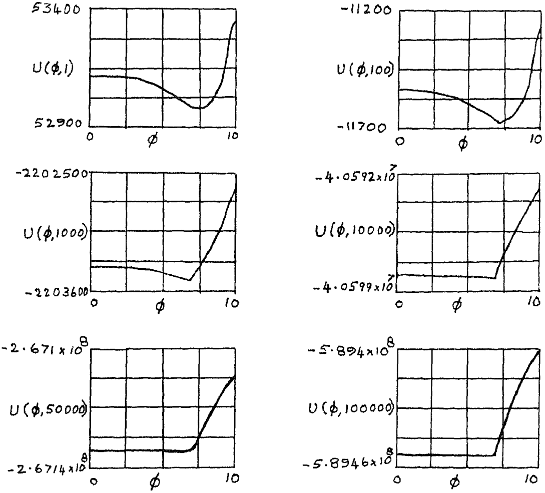

Figure 9. Effective potential at various temperatures-Φ^6 theory high temperature expansion.

Using the numerically obtained value of the effective mass, effective potential can be calculated using high temperature expansion (figure 9). The graphs clearly indicate broken symmetry phase at zero temperature. Comparison with the graphs obtained earlier [23] shows that behaviours of Φ^6 and Φ^4 theories are similar apart from considerable differences in numerical values.

References

[1] D Kirzhnits and A Linde, *Phys. Lett.* **B42**, 471 (1972)
[2] L Dolan and R Jackiw, *Phys. Rev.* **D9**, 3320 (1974)
[3] A D Linde, *Rep. Prog. Phys.* **42**, 861 (1979)
[4] S Weinberg, *Phys. Rev.* **D9**, 3357 (1974)
[5] S Coleman and E Weinberg, *Phys. Rev.* **D7**, 1888 (1973)
[6] R Jackiw, *Phys. Rev.* **D9**, 1686 (1974)
[7] A D Dologov, *Phys. Rep.* **222**, 309 (1992)
[8] V Kuzmin, V Rubakov and M Shaposhnikov, *Phys. Lett.* **B155**, 36 (1985)
[9] M E Carrington, *Phys. Rev.* **D45**, 2933 (1992)
[10] M E Carrington and J I Kapusta, *Phys. Rev.* **D47**, 5304 (1993)
[11] J I Kapusta, D B Reiss and S Rudaz, *Nucl. Phys.* **B263**, 207 (1986)
[12] M E Shaposhnikov, *Phys. Lett.* **B277**, 324 (1992)

[13] P Arnold, *Phys. Rev.* **D46**, 2628 (1992)
[14] J E Eponosa, M Quiros and F Swirner, *Phys. Lett.* **B291**, 115 (1992)
[15] F Grassi, R Hakkim and H D Sivak, *Int. J. Mod. Phys.* **A6**, 4579 (1991)
[16] G A Hajj and P M Stevenson, *Phys. Rev.* **D37**, 413 (1988)
[17] I Roditi, *Phys. Lett.* **B169**, 264 (1986)
[18] I Roditi, *Phys. Lett.* **B177**, 85 (1986)
[19] W A Bardeen and M Moshe, *Phys. Rev.* **D34**, 1229 (1986)
[20] M Dine, R G Leigh, P Huet, A D Linde and D Linde, *Phys. Rev.* **D46**, 550 (1992)
[21] R H Brandenberger, *Rev. Mod. Phys.* **57**, 1 (1985)
[22] S W Hawking and I G Moss, *Nucl. Phys.* **B224**, 180 (1983)
[23] G A Camelia and S Y Pi, *Phys. Rev.* **D47**, 2356 (1993)
[24] J M Cornwall, R Jackiw and E Tomboulis, *Phys. Rev.* **D10**, 2428 (1974)
[25] K T Mahanthappa and J Randa, *Phys. Rev.* **D27**, 2500 (1983)
[26] J Randa, *Phys. Rev.* **D27**, 2531 (1983)
[27] V Branchina, P Castornia, M Consoli and Z Zappala, *Phys. Rev.* **D42**, 3587 (1990)
[28] Janaki Balakrishnan and G Moss Ian, *Phys. Rev.* **D49**, 4113 (1994)
[29] G G Boyd, D E Brahm and S D H Hsu, *Phys. Rev.* **D48**, 4952 (1993)
[30] R Jackiw and S Templeton, *Phys. Rev.* **D24**, 2291 (1981)
[31] L V Belvedre, *Phys. Rev.* **D41**, 2612 (1990)
[32] D K Campbell and A K Bishop, *Nucl. Phys.* **B200**, 297 (1982)
[33] P M Stevenson and I Roditi, *Phys. Rev.* **D33**, 2305 (1986)
[34] R D Pisarski, *Phys. Rev. Lett.* **48**, 574 (1982)
[35] K Babu Joseph and V C Kuriakose, *J. Phys.* **A15**, 2231 (1982)

Spin observables of the NN interaction in a relativistic harmonic model with confined gluons and mesons

K B VIJAYAKUMAR and S B KHADKIKAR*
Department of Physics, Mangalore University, Mangalagangothri 574 199, India
* Inter-University Centre for Astronomy and Astrophysics, Post Box No 4, Ganeshkhind, Pune 411 007, India
Email: kbvijay@mnglr. ernet.in

MS received 26 August 1996; revised 8 December 1997

Abstract. Polarization observables for the nucleon–nucleon (NN) scattering are investigated in the frame work of relativistic harmonic model below $E_{\text{lab}} = 250\,\text{MeV}$, with the inclusion of the σ and π meson exchange. The results can be interpreted as the 'Cheshire cat principle' of NN interaction.

Keywords. Quark model; harmonic model; confined gluon; polarization observables; Cheshire cat.

PACS No. 13.76

1. Introduction

We investigate here the effect of exchange of confined gluons among relativistically confined quarks in nucleon–nucleon (NN) scattering calculations.

In our previous work [1–3], we investigated the $^1S_0$ and $^3S_1$ (without S-D coupling) phase shifts by using different size parameters with and without the exchange of σ and π mesons in the hamiltonian. The agreement of the results of both the models was interpreted as the 'Cheshire cat principle' [1] valid also for NN interaction. The term in the confined one gluon exchange potential (COGEP) arising from the confinement of gluons plays the role of σ by giving the required attraction in the NN interaction. In our subsequent work [3] we studied the phase shifts of higher order partial waves without invoking σ and π mesons in our model with only α_s (strong coupling constant) as a new parameter. Even though the calculated phase shifts for higher partial waves did not compare well with the phenomenological phase shifts of Arndt *et al* [4] the proton–proton (pp) and neutron–proton (np) differential cross sections $(\sigma(\theta))$ obtained were in good agreement with the experimental $\sigma(\theta)$. The purpose of the present calculation is to establish our earlier claim of 'Cheshire cat principle' [1] of NN interaction. The Cheshire cat models are the version of the MIT bag model [5–7], where physics become completely insensitive to the change in the bag radius. In these models the shifting of the bag wall has no physical effect. Therefore, the radius of the bag can be pushed to infinity resulting in a purely fermionic description (i.e. QCD) or to zero, so that the description is entirely bosonic (i.e. some effective meson theory). To test the validity of the 'Cheshire cat' syndrome we have performed the calculations with the exchange of σ and π mesons in the spirit of non-relativistic quark models (NRQM) [8–11] and with the quark core size 0.5–0.6 fm. It is to be noted that this is smaller than the physical size of a nucleon and has to be supplemented by a pion cloud as in NRQM.

For the confinement of quarks we are making use of the relativistic harmonic model (RHM) [12] which has been successful in explaining the properties of light hadrons. For the confinement of gluons we have made use of the current confinement model (CCM) [13–15] which was developed in the spirit of the RHM. The CCM has been quite successful in describing the glue-ball spectra [14]. The full hamiltonian used in our investigation has the usual kinetic energy, two body confinement potential and the COGEP along with σ and π meson potentials. In consistency with our earlier work [1] we have used a smaller oscillation size parameter so as to include σ and π mesons in our calculation. The parameters used in our calculation are listed in reference [1]. We have employed the exact analogous formulation of NRQM, using the resonating group method (RGM) [16, 17] and have calculated the scattering phase shifts as a function of energy using the Kohn–Hulthen–Kato variational principle formulated by Kamimura [18].

Here, we report the results of NN polarization observables (PO) by including phase shifts of all significant partial waves up to angular momentum $(L) = 2$ with the inclusion of σ and π mesons exchange potentials but taking into account the effect of confinement of gluons. Further, we compare the np PO calculated from the theoretical computed phase shifts with the existing experimental data so as to test directly the predictions of our calculation with the observable quantities.

2. Spin polarization in NN scattering

In this section we present the results of calculated PO in comparison with the PO obtained from the phase shifts of Arndt *et al* [19]. In our work we have employed the formulation and the notation of Bystricky *et al* [20]. In the formulation the polarization matrix X_{pqik} with four indices, which correspond to the polarization directions of the scatterer, recoil, beam and target. If the polarization of the particle is not analysed (or unpolarized) the corresponding index is set to zero. If the analysis of the polarization of particle is carried out, then these index are set to n, m or l corresponding to the spin projection on the basis vectors. The polarization matrix X_{pqik} is defined through the NN scattering matrix M. The scattering matrix M for each iso-spin state is expressed in terms of the invariant scattering amplitude a, b, c, d and e which are complex functions of energy and scattering angle θ. The five amplitudes a, b, c, d, e with the T-matrix (T-matrix $=$ S-matrix-1) elements can be determined from the phase shifts and the mixing parameters using the partial wave decomposition [20–22]. The details can be found in standard reference of Bystricky *et al* [20]. We have calculated PO in the energy range E_{lab} 0 MeV to 250 MeV for np interaction. The standard convention is to call P a polarization, and D a depolarization. The expressions for the following variables are given in references [20–22].

In figure 1 we display spin observables P_{n000} at 50 and 150 MeV for np interaction. The agreement between experimental data [19] and theoretically computed phase shifts is good at 150 MeV. But there is a typical deviation to the theoretical curve at 50 MeV. This

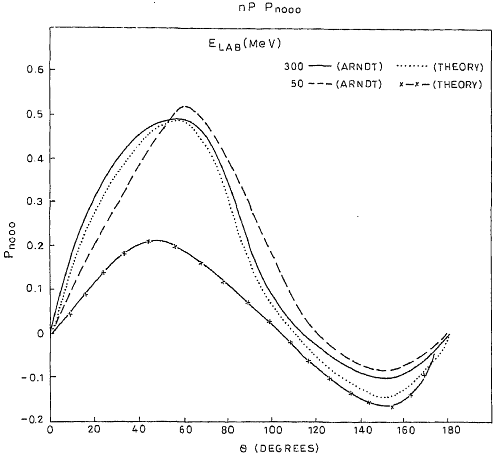

Figure 1. The calculated np polarization observable P_{n000} as a function of scattering angle (θ) in degrees, in comparison with Arndt *et al* [19].

means at low energy the phase shifts are not well determined. This implies that polarization is sensitive to NN interaction at small distances. Similar conclusions have been arrived by Macharvariani *et al* [21]. Figure 2 is a plot of depolarization D against the scattering angle (θ). The D determines the amount of polarization perpendicular to the scattering plane converted into the same after the second scattering. Here, the agreement between theory and experiment is better at all energies [19]. In the next section the important results are stated and summarized.

3. Conclusion

In this paper an attempt has been made to understand the NN PO in the frame work of the RHM and the CCM by employing the RGM formulation. The aim was to understand the role played by the confined gluons on NN interaction. We have computed the phase shifts of all partial waves up to $L = 2$ taking into account the confinement of gluons but by invoking σ and π mesons in the spirit of NRQM. With a smaller oscillator size parameter in consistent with RHM, the model is able to reproduce the phase shifts of most of the partial waves. The np PO are also in agreement with the corresponding experimental observables. However, for the majority of the PO no direct data exists. The confined gluons along with conventional σ and π mesons satisfactorily explain NN observables.

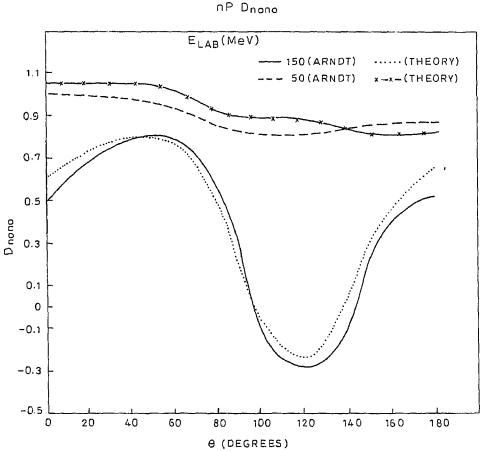

Figure 2. The calculated np polarization observable D_{n0n0} as a function of scattering angle (θ) in degrees, in comparison with Arndt *et al* [19].

The results obtained clearly establishes the validity of 'Cheshire cat principle' in NN interaction.

References

[1] S B Khadkikar and K B Vijayakumar, *Phys. Lett.* **B254**, 320 (1991)
[2] S B Khadkikar and K B Vijayakumar, *Pramana – J. Phys.* **36**, 557 (1991)
[3] K B Vijayakumar and S B Khadkikar, *Nucl. Phys.* **A556**, 396 (1993)
[4] R A Arndt, L D Roper, R A Bryan, R B Clark, B J VerWest and P Signell, *Phys. Rev.* **D28**, 97 (1983)
[5] V Vento, M Rho, E M Nyman, J H Jun and G E Brown, *Nucl. Phys.* **A345**, 413 (1980)
[6] G E Brown, J W Durso and M B Johnson, *Nucl. Phys.* **A397**, 447 (1983)
[7] S Nadkarni, H B Nielsen and I Zahed, *Nucl. Phys.* **B253**, 308 (1985)
[8] C S Warke and R Shanker, *Phys. Rev.* **C21**, 2643 (1980)
[9] K Brauer, A Faessler, F Fernandez and K Shimizu, *Nucl. Phys.* **A507**, 599 (1990)
[10] A Faessler, F Fernandez, G Lubeck and K Shimizu, *Nucl. Phys.* **A402**, 555 (1983)
[11] M Oka and K Yazaki, *Prog. Theor. Phys.* **66**, 556, 572 (1981)
[12] S B Khadkikar and S K Gupta, *Phys. Lett.* **B124**, 523 (1983)
[13] S B Khadkikar, *Pramana – J. Phys.* **24**, 63 (1985)
[14] S B Khadkikar and P C Vinod Kumar, *Pramana – J. Phys.* **29**, 39 (1987)
[15] P C Vinod Kumar, K B Vijayakumar and S B Khadkikar, *Pramana – J. Phys.* **39**, 47 (1992)
[16] J A Wheeler, *Phys. Rev.* **52**, 1083 (1937)
[17] Y C Tang, M Lemere and D R Thompson, *Phys. Rep.* **3**, 167 (1978)

[18] K Kamimura, *Prog. Theor. Phys. Suppl.* **62**, 236 (1977)
[19] R A Arndt, L D Roper, R L Workman and M W McNaughton, *Phys. Rev.* **D45**, 3995 (1992)
[20] J Bystricky, C Lechanoine-Leluc and F Lehar, *J. Phys.* **48**, 199 {1987)
[21] A I Machavariani, U Straub and A Faessler, *Nucl. Phys.* **A548**, 592 (1992)
[22] D R Entem, A I Machavariani, A Valcarce, A J Buchmann, A Faessler and F Fernandez, *Nucl. Phys.* **A602**, 308 (1996)

physics

pp. 155–162

Ratio of the color suppressed decays $\Lambda_b \to \Lambda J/\psi$ and $B^0 \to KJ/\psi$

A K GIRI and R MOHANTA
Physics Department, Utkal University, Bhubaneswar 751 004, India
E-mail: nanda@iop.ren.nic.in

MS received 5 April 1997; revised 4 December 1997

Abstract. Based on the factorization approximation, we have estimated the ratio of the branching fractions for the color suppressed nonleptonic decays $\Lambda_b \to \Lambda J/\psi$ and $B^0 \to KJ/\psi$. Treating the s-quark as heavy, we have used the HQET to calculate the hadronic matrix elements. The mesonic Isgur–Wise function is calculated in the quark model whereas for the baryonic IW function we have employed the bound state soliton picture. The results obtained agree very well with the recent CDF experimental data.

Keywords. Factorization approximation; heavy quark effective theory; Isgur–Wise function.

PACS Nos 11.30; 13.25; 13.30

1. Introduction

Recently the decay mode $\Lambda_b \to \Lambda J/\psi$ has been observed at the Femilab [1] and the production cross section times branching fraction for the decay $\Lambda_b \to \Lambda J/\psi$ relative to that of $B^0 \to KJ/\psi$ has been measured to be $0.27 \pm 0.12 \pm 0.05$. Based on the factorization approach, we have shown that the CDF data [1] for the ratio $\mathrm{Br}(\Lambda_b \to \Lambda J/\psi)/\mathrm{Br}(B^0 \to KJ/\psi)$ can be well accounted for in the framework of heavy quark effective theory (HQET) [2–5]. Much of the success of HQET has been in the treatment of decays from one heavy flavor to another, namely $b \to c$ transitions. However, one approximation used recently in the literature has been to treat the *strange* quark as heavy, so that the decays we are interested here can be considered as heavy to heavy transitions. In fact the previous challenging studies [6–9] suggest that the heavy quark effective theory is still effective for s-system, if a constituent quark mass is employed for m_s and $1/m_s$ corrections are taken into account properly. Therefore it is interesting to examine the applicability of the heavy flavor symmetry in the s-quark system even if the s quark mass is not large enough compared to the QCD scale Λ_{QCD}. There is a lot of altercation in the literature regarding the fact, 'whether HQET could be applied to s quark system or not'. In a recent letter Chakraverty *et al* [10] have shown that heavy quark symmetry is not reliable for the s quark system. On the other hand applying HQET to $B \to K^{(*)}$ transitions, Robert and Ledroit [11] suggested that the heavy s limit may give an acceptable description of unpolarized data but does not give reliable results when applied to polarization observables (Γ_L/Γ). In this paper we assume the validity of HQET for s-quark system and examine the ratio of the branching fractions for the decays $\Lambda_b \to \Lambda J/\psi$ relative to $B^0 \to KJ/\psi$, with the factorization approximation.

Factorization in two body non-leptonic decays of heavy pseudoscalar mesons [12] was resurrected a few years ago as a means of estimating their decay rates using the existing calculation of the semileptonic decay form factors. It relates the complicated non-leptonic decay amplitudes to products of meson decay constant and hadronic matrix elements of current operators similar to the ones encountered in semileptonic decays. This approximation appears to work well phenomenologically in the B decays, where it has been tested very well [13].

Nonleptonic decays of heavy baryons in general receive contributions from W decay and W exchange diagrams. The calculation of W exchange amplitudes has to rely on phenomenological models and introduces large theoretical uncertainties [14]. The decay mode $\Lambda_b \to \Lambda J/\psi$ is however free from such contributions and proceeds through the W decay diagram. This allows to make rather clean theoretical prediction for the decay rate. Assuming factorization, the matrix element of the effective Hamiltonian is given by the product of the baryonic decay transition and the meson decay constant, i.e.,

$$\langle J/\psi\Lambda|\mathcal{H}_{\text{eff}}|\Lambda_b\rangle \approx \langle J/\psi|\bar{c}\gamma^\mu(1-\gamma_5)c|0\rangle\langle\Lambda|\bar{s}\gamma_\mu(1-\gamma_5)b|\Lambda_b\rangle. \tag{1}$$

To evaluate the hadronic matrix elements we use the results of HQET, treating s-quark as heavy. Since we are dealing with the evaluation of the ratio of the branching fractions for $B^0 \to KJ/\psi$ and $\Lambda_b \to \Lambda J/\psi$ decay processes, we have not included $1/m_s$ corrections in our calculations. As these small corrections appear both in numerator and in denominator, it is assumed to be cancelled without effecting much the leading order result. Therefore at the leading order these matrix elements can be described by the single universal form factor, the well known Isgur–Wise (IW) function. HQET predicts that the Isgur–Wise function is related to the overlap of the light degrees of freedom wavefunctions of the heavy particles. In general the light component is very complicated, but in the valence quark approximation the light component of a heavy meson is a light antiquark whereas the light component of the heavy baryon is a light diquark. This implies the fact that the mesonic and baryonic Isgur–Wise functions are quite different from each other and need to be evaluated separately.

The IW functions are not calculable from perturbative QCD. On the contrary, heavy quark symmetry tells us only the normalization of the Isgur–Wise function at the zero recoil point i.e., when the initial and the final heavy quarks have the same velocity. Since apart from the zero recoil point HQET does not predict the shape of the IW function, it makes sense to calculate it in a model, which gives the same result in the appropriate limit as predicted by the HQET. Here we therefore use the quark model of Ali *et al* [8] to evaluate the mesonic Isgur–Wise function and the bound state soliton picture [15] for the baryonic function.

The outline of the paper is as follows. In § 2 we present the formalism for the description of nonleptonic decays of heavy mesons and baryons using the factorization approximation. The Isgur–Wise functions are calculated in § 3. Section 4 contains result and discussions.

$$\mathcal{H}_{\rm eff} = \frac{G_{\rm F}}{\sqrt{2}} V_{cb} V_{cs}^{*} [C_1(m_b)(\bar{c}\gamma_\mu(1-\gamma_5)b)(\bar{s}\gamma^\mu(1-\gamma_5)c)$$
$$+ C_2(m_b)(\bar{s}\gamma_\mu(1-\gamma_5)b)(\bar{c}\gamma^\mu(1-\gamma_5)c)], \qquad (2)$$

where $G_{\rm F}$ is the Fermi coupling constant; C_1 and C_2 are the Wilson coefficients which contain the short distance QCD corrections. In the leading logarithmic approximations they are given to be [16]

$$C_1(m_b) = 1.12 \quad \text{and} \quad C_2(m_b) = -0.26. \qquad (3)$$

The effective Hamiltonian describes two classes of nonleptonic decays. The first class is of the type: $\Lambda_b \rightarrow \Lambda_c D_s$ and $B^0 \rightarrow D D_s$, while the second class represent $\Lambda_b \rightarrow \Lambda J/\psi$ and $B^0 \rightarrow K J/\psi$; J/ψ is the charmonium state.

To evaluate the matrix element of the effective Hamiltonian, we employ factorization assumption. By Fierz rearrangement, we rewrite the effective Hamiltonian in a form suitable for the use of this assumption. Upon Fierz rearrangement, the factorized Hamiltonian for the decays is given as

$$\mathcal{H}_{\rm eff} = \frac{G_{\rm F}}{\sqrt{2}} V_{cb} V_{cs}^{*} a_2 (\bar{s}\gamma_\mu(1-\gamma_5)b)(\bar{c}\gamma^\mu(1-\gamma_5)c), \qquad (4)$$

where $a_2 = C_2 + C_1/N_{\rm c}$, with $N_{\rm c}$ is the number of colors. One may expect $N_{\rm c} = 3$, but the decay rate obtained from factorization is too small for $N_{\rm c} = 3$, while the limit $N_{\rm c} \rightarrow \infty$ gives a remarkable value. Since in this paper we are dealing with the ratio of the branching fractions, the dependence on $N_{\rm c}$ is unimportant.

As pointed out in the previous section we evaluate the matrix elements of the effective Hamiltonian using the factorization approximation. For $B^0 \rightarrow K J/\psi$ transition, we therefore write the transition amplitude as

$$\mathcal{A}(B^0(v_1) \rightarrow K(v_1')J/\psi(p_\psi, \epsilon_\psi)) = \frac{G_{\rm F}}{\sqrt{2}} V_{cb} V_{cs}^{*} a_2 \langle J/\psi(p_\psi, \epsilon_\psi)|\bar{c}\gamma^\mu(1-\gamma^5)c|0\rangle$$
$$\times \langle K(v_1')|\bar{s}\gamma_\mu(1-\gamma_5)b|B^0(v_1)\rangle. \qquad (5)$$

The hadronic matrix element $\langle K(v_1')|\bar{s}\gamma_\mu(1-\gamma_5)b|B^0(v_1)\rangle$ is extracted from the corresponding semileptonic decays of B mesons into the Kaon state. In the heavy s-limit it is given in the HQET [4] as

$$\langle K(v_1')|\bar{s}\gamma_\mu(1-\gamma_5)b|B^0(v_1)\rangle = \sqrt{m_b m_s}\, \xi(\omega_1)(v_1 + v_1')_\mu, \qquad (6)$$

where $\xi(\omega_1)$ is the mesonic Isgur–Wise function with $\omega_1 = (v_1 \cdot v_1')$. The remaining matrix element can be written as

$$\langle J/\psi(p_\psi, \epsilon_\psi)|\bar{c}\gamma^\mu(1-\gamma_5)|0\rangle = M_\psi . f_\psi \epsilon_\psi^\mu, \qquad (7)$$

where f_ψ is the charmonium decay constant and ϵ_ψ^μ denotes its polarization.

Using eqs (5–7) we obtain the partial decay width of $B^0 \to KJ/\psi$ decay mode in the rest frame of initial B^0 meson as

$$\Gamma(B^0(v_1) \to K(v_1')J/\psi(p_\psi, \epsilon_\psi)) = \frac{G_F^2}{16\pi} |\mathbf{p}_1| |V_{cb}V_{cs}^*|^2 a_2^2 f_\psi^2 \xi^2(\omega_1) \times m_b m_s(\omega_1^2 - 1)\left(1 + \frac{M_K}{M_B}\right)^2, \tag{8}$$

where $|\mathbf{p}_1|$ is the c.o.m momentum of the emitted particles and is given as

$$|\mathbf{p}_1| = \frac{1}{2M_B}[(M_B^2 - M_K^2 - M_\psi^2)^2 - 4M_K^2 M_\psi^2]^{1/2}. \tag{9}$$

Now similarly for the $\Lambda_b \to \Lambda J/\psi$ transition, the hadronic matrix element of the factorized amplitude from eq. (1) can be written as

$$\langle\Lambda(v_2', s')|\bar{s}\gamma_\mu(1-\gamma_5)b|\Lambda_b(v_2, s)\rangle = \eta(\omega_2)\bar{u}_\Lambda(v_2', s')\gamma_\mu(1-\gamma_5)u_{\Lambda_b}(v_2, s), \tag{10}$$

where $\eta(\omega_2)$ is the baryonic Isgur–Wise function with $\omega_2 = v_2 \cdot v_2'$. The spinors present in the above equation $u_\Lambda(v_2', s')$ and $u_{\Lambda_b}(v_2, s)$ are the usual Dirac spinors for the Λ and Λ_b states, with spin sum given as

$$\sum_s u(v, s)\bar{u}(v, s) = \frac{\not{v} + 1}{2}. \tag{11}$$

With eqs (1), (7) and (10) we obtain the partial decay width for $\Lambda_b \to \Lambda J/\psi$ decay as

$$\Gamma(\Lambda(v_2, s) \to \Lambda(v_2', s')J/\psi(p_\psi, \epsilon_\psi)) = \frac{G_F^2}{8\pi M_{\Lambda_b}^2} |\mathbf{p}_2|\, |V_{cb}V_{cs}^*|^2 a_2^2 f_\psi^2 \eta^2(\omega_2) \times [(M_{\Lambda_b}^2 - M_\Lambda^2)^2 + M_\psi^2(M_{\Lambda_b}^2 + M_\Lambda^2 - 2M_\psi^2)], \tag{12}$$

where $|\mathbf{p}_2|$ is the c.o.m momentum of the emitted particles in the rest frame of Λ_b baryon.

After evaluating the partial decay widths for the two types of decays, we now obtain the ratio of their branching fractions as

$$\frac{\mathrm{Br}(\Lambda_b \to \Lambda J/\psi)}{\mathrm{Br}(B^0 \to KJ/\psi)} = \frac{\tau_{\Lambda_b}\Gamma(\Lambda_b \to \Lambda J/\psi)}{\tau_{B^0}\Gamma(B^0 \to KJ/\psi)} = \frac{\tau_{\Lambda_b}}{\tau_{B^0}} \frac{|\mathbf{p}_2|}{|\mathbf{p}_1|} \frac{\eta^2(\omega_2)}{\xi^2(\omega_1)} \frac{2M_B^2}{M_{\Lambda_b}^2} \frac{[(M_{\Lambda_b}^2 - M_\Lambda^2)^2 + M_\psi^2(M_{\Lambda_b}^2 + M_\Lambda^2 - 2M_\psi^2)]}{[(\omega_1^2 - 1)m_b m_s(M_K + M_B)^2]}. \tag{13}$$

Thus one can see from eq. (13) that the ratio of the branching fractions is independent of any model dependent parameters. The only unknown quantities present in the expression are the Isgur–Wise functions $\xi(\omega_1)$ and $\eta(\omega_2)$. These universal functions are evaluated in a simplified manner as presented in the following section.

3. Evaluation of the Isgur–Wise functions

The Isgur–Wise function which represents the nonperturbative QCD effects, are a measure of the light cloud (spectator quarks) rearrangement around the heavy quark subsection 3.2.

3.1 $\xi(\omega_1)$ *for* $B^0 \rightarrow KJ/\psi$

The Isgur–Wise function calculated in the quark model, predicts the decay widths for rare $B \rightarrow K^*\gamma$ [8] and the branching ratios of nonleptonic B mesons [7, 17] very well. In this model the function $\xi(\omega_1)$ can be obtained from the overlap integral as

$$\xi(\omega_1) = \int r^2 \mathrm{d}r \phi_{\mathrm{F}}^*(r)\phi_{\mathrm{I}}(r) j_0(\Lambda r\sqrt{\omega_1^2 - 1}), \tag{14}$$

where ϕ_{I} and ϕ_{F} refer to the radial wave functions of the initial and final mesons respectively. j_0 is the spherical Bessel function of the zeroth order. The 'inertia parameter Λ' is taken to be [18]

$$\Lambda = \frac{M_K \cdot m_d}{m_s + m_d} = \frac{3}{8} M_K, \tag{15}$$

for the constituent quark mass values $m_d = 330\,\mathrm{MeV}$ and $m_s = 550\,\mathrm{MeV}$. To calculate the Isgur–Wise function (14) we use the wave functions of harmonic oscillator for ϕ_{I} and ϕ_{F} in the form

$$\phi(r) = \left(\frac{4\beta^3}{\sqrt{\pi}}\right)^{1/2} \exp(-\beta^2 r^2/2), \tag{16}$$

with oscillator strength β. The values of β_K and β_B fitted in ref. [19] ($\beta_K = 0.34\,\mathrm{GeV}$ and $\beta_B = 0.41\,\mathrm{GeV}$) are not equal. However we have assumed β to be same, for the initial and final mesons and obtain

$$\xi(\omega_1) = \exp\left(\frac{-\Lambda^2(\omega_1^2 - 1)}{4\beta^2}\right). \tag{17}$$

We have taken $\beta = 0.295$ GeV, which is extracted from the best fit in ref. [7].

The value of ω_1 is determined by considering the kinematics of the system. Since we are dealing with the two body decays $B^0(v_1) \rightarrow K(v_1')J/\psi(p_\psi)$, momentum conservation gives

$$M_B v_1^\mu = M_K v_1'^\mu + p_\psi^\mu, \tag{18}$$

which gives

$$\omega_1 = v_1 \cdot v_1' = \frac{M_B^2 + M_K^2 - M_\psi^2}{2M_B M_K}. \tag{19}$$

Thus with eqs (17) and (19) we have obtained the mesonic Isgur–Wise function $\xi(\omega_1)$ to be

$$\xi(\omega_1) = 0.317. \tag{20}$$

3.2 $\eta(\omega_2)$ *for* $\Lambda_b \to \Lambda J/\psi$

Here we have presented the evaluation of the Isgur–Wise function in the same manner as suggested in ref. [15]. The Isgur–Wise function calculated in this manner explains very well the two body non-leptonic decays $\Lambda_b \to \Lambda_c P(V)$ [20] and the radiative rare decay $\Lambda_b \to \Lambda\gamma$ [21]. In this model the heavy baryons are treated as the bound state of the soliton with the heavy meson. The Isgur–Wise function is given as

$$\eta(\omega_2) = \int d^3\mathbf{q}\Phi^*(\mathbf{q})\Phi(\mathbf{q} + m_B(\mathbf{v}_2 - \mathbf{v}_2')), \tag{21}$$

where m_B represents the mass of the soliton which is taken as the mass of nucleon, for the ground state Λ_Q baryons.

The binding potential between the heavy meson and the chiral soliton is simple harmonic [22] and hence the wave function is taken as

$$\Phi(\mathbf{q}) = \frac{1}{(\pi^2 m_B \kappa)^{3/8}} \exp\left(-\frac{\mathbf{q}^2}{2\sqrt{m_B\kappa}}\right), \tag{22}$$

κ is the spring constant and its value is taken to be $(440\,\mathrm{MeV})^3$ [23]. In the rest frame of the initial state, $v_2 = (1, \mathbf{0})$ and $\mathbf{v}_2'$ directed along z-axis we obtain the Isgur–Wise function (21) using (22) for non-relativistic recoils i.e., $|\mathbf{v}_2'|^2 \approx 2(\omega_2 - 1)$, as

$$\eta(\omega_2) = \exp\left(-\frac{(\omega_2 - 1)}{2}\sqrt{\frac{m_B^3}{\kappa}}\right). \tag{23}$$

Again ω_2 is obtained by considering the kinematics of the system, given as

$$\omega_2 = v_2 \cdot v_2' = \frac{M_{\Lambda_b}^2 + M_\Lambda^2 - M_\psi^2}{2M_{\Lambda_b}M_\Lambda}. \tag{24}$$

Now with eq. (24) the baryonic Isgur–Wise function (23) is found to be

$$\eta(\omega_2) = 0.263. \tag{25}$$

4. Results and discussion

In order to obtain the value of the ratio of the branching fractions $\mathrm{Br}(\Lambda_b \to \Lambda J/\psi)/\mathrm{Br}(B^0 \to KJ/\psi)$ with eq. (13) we use the following values. The quark masses are taken as $m_b = 4.5\,\mathrm{GeV}$ and $m_s = 550\,\mathrm{MeV}$. The masses of Λ_b and B^0 particles are taken from ref. [1] as $M_{\Lambda_b} = 5621$ MeV and $M_B = 5281$ MeV. The other particle masses and the life times of Λ_b and of B^0 are taken from ref. [24]. With these values we obtain the ratio of the branching fractions to be

$$\frac{\mathrm{Br}(\Lambda_b \to \Lambda J/\psi)}{\mathrm{Br}(B^0 \to KJ/\psi)} = 1.017. \tag{26}$$

Using the value $\sigma_{\Lambda_b}/\sigma_{B^0} = 0.1/0.375$ from ref. [1], we obtain the production cross section times branching fraction for the decay $\Lambda_b \to \Lambda J/\psi$ relative to that of the decay

$B^0 \to KJ/\psi$ as

$$\frac{\sigma_{\Lambda_b} \mathrm{Br}(\Lambda_b \to \Lambda J/\psi)}{\sigma_{B^0} \mathrm{Br}(B^0 \to KJ/\psi)} = 0.271, \tag{27}$$

which is in excellent agreement with the CDF data 0.27 ± 0.12 ± 0.05 [1]. The overall agreement of our result with the experimental data justifies the fact that factorization approximation works well for the description of color suppressed nonleptonic decays (decays proportional to a_2) of the heavy hadrons.

In this paper we have estimated the ratio of the branching fractions of the color suppressed nonleptonic decays $\Lambda_b \to \Lambda J/\psi$ and $B^0 \to KJ/\psi$, based on the factorization approximation. Treating the s-quark as heavy, we have used HQET for the evaluation of the hadronic matrix elements. Since HQET does not predict the shape of the IW function and of course visualizing the fact that the IW functions are different for the baryonic and mesonic sectors, due to the different configuration in their light degrees of freedom, we employ the well established models for their evaluation. The Isgur–Wise function is evaluated in the quark model [8] for $B^0 \to KJ/\psi$ decay and in the bound state soliton picture [15] for $\Lambda_b \to \Lambda J/\psi$ decay mode. Since the evaluation of the Isgur–Wise function is of course model dependant, there are some theoretical uncertainties introduced as two different models are followed for the estimation of mesonic and baryonic IW functions. The ISGW quark model for the mesonic case is quite well established [6–8, 17]. In fact if the baryonic IW function could have been evaluated in the quark model then hopefully the uncertainties would have been small. However in the absence of such a treatment we have followed a different model for it, so it is necessary to test the reliability of the model. For the sake of comparison we therefore calculate the branching ratio for $B^0 \to KJ/\psi$ process using eqs (8) and (20) and thus from eq. (26) we obtain the branching ratio for $\Lambda_b \to \Lambda J/\psi$ decay process. Now comparing this predicted value with the quark model calculation [25] (without using HQET) the validity of the bound state soliton picture for the baryonic IW function can be seen easily.

To calculate the branching fraction for $B^0 \to KJ/\psi$, we use $|V_{cs}| = 0.9738$, $|V_{cb}| = 0.038$, $a_2 = 0.23$. The decay constant f_ψ can be obtained from the leptonic width of the charmonium state [11] as $f_\psi = 382\,\mathrm{MeV}$. Thus we obtain $\mathrm{Br}(B^0 \to KJ/\psi)$ to be

$$\mathrm{Br}(B^0 \to KJ/\psi) = 3.917 \times 10^{-4}, \tag{28}$$

and with eq. (26) we obtain

$$\mathrm{Br}(\Lambda_b \to \Lambda J/\psi) = 3.984 \times 10^{-4}. \tag{29}$$

Using $1/m_Q$ corrections to the baryonic form factors in the quark model Cheng *et al* [25] obtained

$$\mathrm{Br}(\Lambda_b \to \Lambda J/\psi) = 2.1 \times 10^{-4}. \tag{30}$$

Our present calculation is somewhat greater than their predictions. This decay mode is now observed experimentally by CDF [1]. The branching ratio of $\mathrm{Br}(\Lambda_b \to \Lambda J/\psi) = (3.7 \pm 1.7 \pm 0.4) \times 10^{-4}$ assuming $\mathrm{Br}(B^0 \to KJ/\psi) = 3.7 \times 10^{-4}$. It is seen from eq. (30) that the quark model [25] prediction does not agree well with the experiment. In contrast, our calculation is very simple and free from any theoretical uncertainties besides in the sector of Isgur–Wise functions. It is interesting to note that our theoretical predictions (28) and (29) agree reasonably well with these experimental values. Therefore it should be inferred from the above observation that the evaluation of the IW function using two different models do not introduce much theoretical uncertainties. Our results indicate that the heavy quark symmetry does work in the first approximation to calculate the exclusive decays involving $b \to s$ transitions.

Acknowledgements

We are thankful to Profs B B Deo, N Barik and Dr L Maharana for many useful discussions and suggestions. RM would like to thank CSIR, Govt. of India, for financial support.

References

[1] F Abe *et al*, *Phys. Rev.* **D55**, 1142 (1997)
[2] N Isgur and M B Wise, *Phys. Lett.* **B232**, 113 (1989); *Phys. Lett.* **B237**, 527 (1990); *Nucl. Phys.* **B348**, 276 (1991)
[3] H Georgi, *Phys. Lett.* **B240**, 447 (1990); *Nucl. Phys.* **B348**, 293 (1991)
[4] A F Falk, H Georgi, B Grinstein and M B Wise, *Nucl. Phys.* **B343**, 1 (1990)
[5] M Neubert, *Phys. Rep.* **245**, 259 (1994)
[6] A Ali and T Mannel, *Phys. Lett.* **B264**, 447 (1991)
M R Ahmady and D Liu, *Phys. Lett.* **B302**, 491 (1993)
[7] M R Ahmady and D Liu, *Phys. Lett.* **B324**, 231 (1994)
[8] A Ali, T Ohl and T Mannel, *Phys. Lett.* **B298**, 195 (1993)
[9] T Ito, T Morii and M Tanimoto, *Phys. Lett.* **B274**, 449 (1992); *Prog. Theor. Phys.* **88**, 561 (1992)
[10] D Chakraverty, T De, B Dutta-Roy and A Kundu, *Int. J. Mod. Phys.* **12**, 2763 (1997)
[11] W Roberts and F Ledroit, *Phys. Rev.* **D53**, 3643 (1996)
[12] M Bauer, B Stech and M Wirbel, *Z. Phys.* **C34**, 103 (1987)
[13] D Bortoletto and S Stone, *Phys. Rev. Lett.* **65**, 2951 (1990)
J L Rosner, *Phys. Rev.* **D42**, 3732 (1990)
M Tanimoto, K Goda and K Senba, *Phys. Rev.* **D42**, 3741 (1990)
V Rieckert, *Phys. Rev.* **D47**, 3053 (1993)
C Reader and N Isgur, *Phys. Rev.* **D47**, 1007 (1993)
T Mannel, W Roberts and Z Ryzak, *Phys. Lett.* **B259**, 359 (1991)
A Deandrea, N Di Bartolomeo, R Gatto and G Nardulli, *Phys. Lett.* **B318**, 549 (1993)
[14] G J Koerner and M Kramer, *Z. Phys.* **C55**, 659 (1992)
[15] C K Chow, *Phys. Rev.* **D51**, 1224 (1995)
[16] G Altarelli and L Maiani, *Phys. Lett.* **B52**, 351 (1974)
M K Gaillard and B W Lee, *Phys. Rev. Lett.* **33**, 108 (1974)
[17] A K Giri, L Maharana and R Mohanta, *Pramana – J. Phys.* **48**, 1005 (1997)
A K Giri and R Mohanta, *Pramana – J. Phys.* **49**, 231 (1997)
[18] T Altomari, *Phys. Rev.* **D37**, 677 (1988)
[19] N Isgur, D Scora, B Grinstein and M B Wise, *Phys. Rev.* **D39**, 799 (1989)
[20] A K Giri, L Maharana and R Mohanta, to appear in *Pramana – J. Phys.*
[21] A K Giri and R Mohanta, to appear in *Pramana – J. Phys.*
[22] E Jenkins, A Manohar and M B Wise, *Nucl. Phys.* **B396**, 38 (1993)
[23] C K Chow and M B Wise, *Phys. Rev.* **D50**, 2135 (1994)
[24] Particle Data Group, Review of Particle Properties, *Phys. Rev.* **D54**, Part-I (1996)
[25] H-Y Cheng and B Tseng, *Phys. Rev.* **D53**, 1457 (1996)

PRAMANA
journal of physics

Vol. 50 No. 2
February 1998

INDIAN ACADEMY OF SCIENCES
Indian National Science Academy
Indian Physics Association

Λ_L. This leads to bounds on Higgs mass. This method has been used by several authors [2,6].

An alternate and in our opinion more transparent approach to the 'triviality' problem in ϕ^4-theories has been provided by Stevenson using variational methods for calculating the effective potential [3]. In Stevenson's approach, the relation between the bare and renormalized coupling constant λ_{REN} (defined as the fourth derivative of the effective potential at the origin and thus different from renormalized coupling mentioned above) is

$$\lambda_{\text{REN}} = \lambda_0 \frac{[1 - 12\lambda_0 I_{-1}(m_R)]}{[1 + 6\lambda_0 I_{-1}(m_R)]}, \tag{4}$$

where m_R^2 is the second derivative of the effective potential at the origin and

$$I_{-1}(m) = \int \frac{\mathrm{d}^3 k}{2(2\pi)^3(\sqrt{k^2 + M^2})^3}. \tag{5}$$

Stevenson showed that in the limit of infinite cut-off, the ground state is unstable (i.e. the energy is unbounded from below) for any positive finite λ_0. This result goes against our naive expectation since the tree level effective potential is bounded from below. However, eq. (4) clearly shows that for infinite cut-off $\lambda_{\text{REN}} = -2\lambda_0$, and this is the reflection of the energy of the ground state being unbounded from below (see eq. (4.24) of ref. [3]). Then for a stable ground state, λ_0 and λ_{REN} both tend to zero for infinite cut-off, which is just a trivial theory; we thus arrive at the conclusion identical to the one referred to earlier. Once again, if we regard the ϕ^4-theory as an effective one, λ_0 can have value up to some maximum below which a stable ground state is possible. For a given coupling constant the Higgs masses can be calculated and for the effective theory to be physically meaningful we should have all these masses sufficiently below cut-off Λ_c, say $\Lambda_c/5$ [5]. With such a restriction, one can establish that the Higgs quartic coupling cannot be arbitrarily large, i.e., it has a maximum allowed value, which translates into an upper bound for M_H/M_W.

Triviality bounds in scalar theories have been studied by various non-perturbative methods. These include RGE [5], improved perturbative [6], and lattice theoretic approach [7]. Results are similar, namely that M_H cannot be heavier than a value in the range 800 GeV–1 TeV [4]. Recently we have used a variational approach [8] to arrive at a similar result. This last approach is extremely simple and admits easy generalization to situations more complicated than SM.

Supersymmetric (SUSY) generalization of the SM have been studied in recent times [9]. The most economic SUSY-extension of the SM is a minimal (MSSM) one [9]. In this version, the quartic couplings are restricted by the gauge coupling with the result that the Higgs cannot be arbitrarily heavy. At tree level, one has the relationship

$$M_H^2 \le M_Z^2 \cos^2 2\beta \le M_Z^2, \tag{6}$$

where $\tan\beta$ is the ratio of the vacuum expectation values (VEV's) of the neutral components of the scalar fields H_2 and H_1 that the MSSM involves. Going beyond the tree approximation does not change (6) qualitatively. Thus, Quiros [10] gives the bound

$$M_H \le 125\,\text{GeV} \tag{7}$$

An alternative supersymmetric model proposed is the next to minimal supersymmetric model (NMSSM) which has two $SU(2) \otimes U(1)$ Higgs doublets and one Higgs singlet [9]. The inclusion of a Higgs singlet is suggested in many superstring models and grand unified models. The NMSSM has more coupling parameters than the MSSM and hence it is an interesting theoretical question to enquire into the upper bounds on the Higgs spectrum, particularly the lightest of them. We expect this to be much higher than the one given in (7) and this is the subject matter of our investigation.

The method we follow here is a variational one. Starting with Hamiltonian of the NMSSM we use a gaussian trial wave functional for the ground state and obtain estimates of mass spectra in terms of the bare parameters of the theory. The strategy then is to vary bare parameters over their entire range, impose restrictions that the masses cannot get very close to the cut-off (say less than $\Lambda_c/5$) and obtain the highest mass of the lightest Higgs particle. The parameter space is however very large, and we will be making specific choices of parameters in the hope that our results will be typical of the model itself.

In the context of NMSSM, recently Wu [11] has analysed the problem (triviality bound of Higgs mass) on the basis of one-loop β function following the work of Dashen and Neuberger [2], imposing the restriction that the heaviest Higgs mass in the theory be smaller than the Landau pole position Λ_L. However his estimate of the Landau pole is based on one-loop result of the β function which is questionable since the coupling constant becomes very large in the neighbourhood of the Landau pole. Further the scalar masses have all been calculated on the basis of 'tree approximation' which again becomes uncertain for large coupling. Our variational method avoids both these problems, since the concept of triviality that we use following Stevenson [3] does not directly depend on the position of Landau pole. Further we determine all masses by variational rather than perturbative methods, which *a priori* does not restrict the coupling to be small.

2. The model

In the NMSSM, the potential of the Higgs sector [11] is

$$\begin{aligned} V = &|hN|^2(\Phi_1^\dagger\Phi_1 + \Phi_2^\dagger\Phi_2) + |h\Phi_1^\dagger\Phi_2 + \lambda N^2|^2 + \tfrac{1}{8}g_1^2(\Phi_1^\dagger\Phi_1 - \Phi_2^\dagger\Phi_2)^2 \\ &+ \tfrac{1}{8}g_2^2[(\Phi_1^\dagger\Phi_1 + \Phi_2^\dagger\Phi_2)^2 - 4(\Phi_1^\dagger\Phi_2)(\Phi_2^\dagger\Phi_1)] + m_1^2\Phi_1^\dagger\Phi_1 + m_2^2\Phi_2^\dagger\Phi_2 \\ &- (m_3^2\Phi_1^\dagger\Phi_2 + \mathrm{h.c.}) + m_4^2N^*N + m_5^2(N^2 + N^{*2}). \end{aligned} \tag{8}$$

Here $\Phi_1 = (\phi_1^\dagger, \phi_1^0)$ and $\Phi_2 = (\phi_2^\dagger, \phi_2^0)$ are two $SU(2) \otimes U(1)$ doublets, N a complex singlet, m's are mass parameters, g's are gauge couplings and h, λ are Higgs couplings. The last five terms represent SUSY-breaking. Equation (8) has two coupling constants h and λ; we will study the strong coupling behaviour when h is very large and hence for simplicity we set $\lambda = 0$. Also we take m_3 to be real and $m_1 = m_2 = m$ for simplicity.

It is more convenient to work with the fields defined by

$$\chi_{1,2} = \frac{1}{\sqrt{2}}(\Phi_1 \pm \Phi_2). \tag{9}$$

Now the Higgs potential reduces to

$$\begin{aligned} V = {} & h^2|N|^2(\chi_1^\dagger\chi_1 + \chi_2^\dagger\chi_2) + \tfrac{1}{4}h^2|\chi_1^\dagger\chi_1 - \chi_2^\dagger\chi_2 + \chi_2^\dagger\chi_1 - \chi_1^\dagger\chi_2|^2 \\ & + (m^2 - m_3^2)\chi_1^\dagger\chi_1 + (m^2 + m_3^2)\chi_2^\dagger\chi_2 + m_4^2 N^* N + m_5^2(N^2 + N^{*2}). \end{aligned} \tag{10}$$

We now assume that the fields $\chi_{1,2}$, where

$$\chi_k \equiv \frac{1}{\sqrt{2}} \begin{pmatrix} \chi_{kR}^c + i\chi_{kI}^c \\ \chi_{kR}^0 + i\chi_{kI}^0 \end{pmatrix}, \quad (k = 1, 2) \tag{11}$$

(the superscripts c and 0 denoting charged and neutral components), break the $SU(2) \otimes U(1)$ symmetry by assuming a non-zero vacuum expectation value (VEV)

$$\langle\chi_1\rangle = \begin{pmatrix} 0 \\ v \end{pmatrix}, \quad \langle\chi_2\rangle = \begin{pmatrix} 0 \\ 0 \end{pmatrix}. \tag{12}$$

All other fields in (10) are assumed to have zero VEV's. Writing $N = 1/\sqrt{2}(N_1 + iN_2)$, there are ten real fields in (10): χ_{1R}^c, χ_{1I}^c, χ_{1R}^0, χ_{1I}^0, χ_{2R}^c, χ_{2I}^c, χ_{2R}^0, χ_{2I}^0, N_1 and N_2, which we denote by η_i ($i = 1$ to 10) respectively and their tree level masses by M_i. Even after χ_1 develops a non-zero VEV, the Higgs potential has a residual symmetry. To see this explicitly we define:

$$\begin{aligned} & \mathbf{G} \equiv (\chi_{1I}^c, -\chi_{1R}^c, \chi_{1I}^0) \equiv (\eta_2, -\eta_1, \eta_4), \\ & \mathbf{H} \equiv (\chi_{2R}^c, \chi_{2I}^c, \chi_{2R}^0) \equiv (\eta_5, \eta_6, \eta_7), \\ & S_1 = \chi_{1R}^0 \equiv \eta_3 \quad \text{and} \quad S_2 = \chi_{2I}^0 \equiv \eta_8. \end{aligned}$$

Now shifting the fields by their VEV's, Higgs potential can be written as

$$\begin{aligned} V = {} & \tfrac{1}{4}h^2(N_1^2 + N_2^2)[\mathbf{G}^2 + (S_1 + v)^2 + \mathbf{H}^2 + S_2^2] \\ & + \tfrac{1}{16}h^2[\mathbf{G}^2 + (S_1 + v)^2 - \mathbf{H}^2 - S_2^2]^2 + \tfrac{1}{4}h^2[\mathbf{G} \cdot \mathbf{H} - (S_1 + v)S_2]^2 \\ & + \tfrac{1}{2}(m^2 - m_3^2)[\mathbf{G}^2 + (S_1 + v)^2] + \tfrac{1}{2}(m^2 + m_3^2)(\mathbf{H}^2 + S_2^2) \\ & + \tfrac{1}{2}(m_4^2 + 2m_5^2)N_1^2 + \tfrac{1}{2}(m_4^2 - 2m_5^2)N_2^2. \end{aligned}$$

Under a $SU(2)$ rotation wherein **G** and **H** are triplets, and (S_1, S_2, N_1, N_2) all singlets, V is invariant. We expect then $M_1 = M_2 = M_4$ and $M_5 = M_6 = M_7$ on account of this symmetry. We note that this symmetry is present in a two-doublet model for the special choice of our parameters. Thus in the two-doublet model discussed in § 2 of ref. [12], setting $v_1 = v_2 = \xi = 0$ and $\lambda_1 = \lambda_4$ makes H_1^0, H_2^0 and H_4^0 degenerate. We will build in this residual symmetry in our variational approach.

In terms of ten real fields the Higgs potential

$$\begin{aligned} V = {} & (m^2 - m_3^2)v^2 + \frac{1}{4}h^2v^4 + \frac{1}{2}(m^2 - m_3^2 + \frac{1}{2}h^2v^2)(\eta_1^2 + \eta_2^2 + \eta_4^2) \\ & + \frac{1}{2}(m^2 - m_3^2 + \frac{3}{2}h^2v^2)\eta_3^2 + \frac{1}{2}(m^2 + m_3^2 - \frac{1}{2}h^2v^2)(\eta_5^2 + \eta_6^2 + \eta_7^2) \\ & + \frac{1}{2}(m^2 + m_3^2 + \frac{1}{2}h^2v^2)\eta_8^2 + \frac{1}{2}(m_4^2 + 2m_5^2 + h^2v^2)\eta_9^2 \end{aligned}$$

$$\begin{aligned}
&+\frac{1}{2}(m_4^2-2m_5^2+h^2v^2)\eta_{10}^2+\frac{1}{16}h^2\sum_{i=1}^{8}\eta_i^4+\frac{1}{4}h^2(\eta_9^2+\eta_{10}^2)\sum_{i=1}^{8}\eta_i^2\\
&+\frac{1}{8}h^2[\eta_1^2(\eta_2^2+\eta_3^2+\eta_4^2-\eta_5^2+\eta_6^2-\eta_7^2-\eta_8^2)\\
&+\eta_2^2(\eta_3^2+\eta_4^2+\eta_5^2-\eta_6^2-\eta_7^2-\eta_8^2)+\eta_3^2(\eta_4^2-\eta_5^2-\eta_6^2-\eta_7^2+\eta_8^2)\\
&+\eta_4^2(-\eta_5^2-\eta_6^2+\eta_7^2-\eta_8^2)+\eta_5^2(\eta_6^2+\eta_7^2+\eta_8^2)\\
&+\eta_6^2(\eta_7^2+\eta_8^2)+\eta_7^2\eta_8^2]+V_{\text{linear}}+V_{\text{cubic}},
\end{aligned}\tag{13}$$

where V_{linear} and V_{cubic} respectively represent the terms linear and cubic in fields. The tree level minima condition is equivalent to equating the term linear in η_3 (i.e. χ_{1R}^0) in (13) to zero,

$$m^2-m_3^2+\tfrac{1}{2}h^2v^2=0. \tag{14}$$

Inspection of the quadratic terms in (13) together with (14) immediately tells us that

$$M_1=M_2=M_4=0, \tag{15}$$

indicating that η_1, η_2 and η_4 are the Goldstones. Furthermore, we have for the charged Higgs triplet

$$M_5^2=M_6^2=M_7^2=m^2+m_3^2-\tfrac{1}{2}h^2v^2, \tag{16}$$

where the degeneracy is as expected. Lastly,

$$M_3^2=m^2-m_3^2+\tfrac{3}{2}h^2v^2, \tag{17}$$

$$M_8^2=m^2+m_3^2+\tfrac{1}{2}h^2v^2, \tag{18}$$

$$M_9^2=m_4^2+2m_5^2+h^2v^2 \tag{19a}$$

and

$$M_{10}^2=m_4^2-2m_5^2+h^2v^2 \tag{19b}$$

are the masses of neutral Higgs. For simplicity we also take $m_5=0$ so that

$$M_9^2=M_{10}^2. \tag{20}$$

3. Gaussian trial wave-functional

In order to obtain information on masses beyond the tree level, we follow a variational method with a Gaussian trial wave-functional. Most generally, this wave functional would be the vacuum state of a set of free fields of masses $\Omega_1,\ldots,\Omega_{10}$ with the Ω's (and v in eq. (12)) representing the variational parameters. However, taking a variational ground state that respects the residual symmetry stated in the last section, we set $\Omega_1=\Omega_2=\Omega_4$ and $\Omega_5=\Omega_6=\Omega_7$. Further imposing the symmetry in (20) we also put $\Omega_9=\Omega_{10}=\Omega_N$. We thus have five independent masses Ω_1, Ω_3, Ω_5, Ω_8 and Ω_N, and of course v, as variational parameters.

Following standard techniques [13], the expectation value of Hamiltonian density $\mathcal{H}$ in our trial vacuum state wave functional is

$$\begin{aligned} V_{\mathrm{G}} =& (m^2 - m_3^2)v^2 + \frac{1}{4}h^2 v^4 + 2\left[\frac{1}{2}(M_N^2 - \Omega_N^2)I_0(\Omega_N^2) + I_1(\Omega_N^2)\right] \\ &+ \sum_{i=1}^{8}\left[\frac{1}{2}(M_i^2 - \Omega_i^2)I_0(\Omega_i^2) + I_1(\Omega_i^2)\right] + \frac{1}{2}h^2 I_0(\Omega_N^2)\sum_{i=1}^{8} I_0(\Omega_i^2) \\ &+ \frac{3}{16}h^2[5I_0^2(\Omega_1^2) + I_0^2(\Omega_3^2) + 5I_0^2(\Omega_5^2) + I_0^2(\Omega_8^2)] \\ &+ \frac{1}{8}h^2[3I_0(\Omega_1^2)(I_0(\Omega_3^2) - I_0(\Omega_5^2) - I_0(\Omega_8^2)) \\ &+ 3I_0(\Omega_5^2)(I_0(\Omega_8^2) - I_0(\Omega_3^2)) + I_0(\Omega_3^2)I_0(\Omega_8^2)]. \end{aligned} \tag{21}$$

Here

$$I_1(\Omega) = \frac{1}{2(2\pi)^4}\int \mathrm{d}^4 k_E \ln(k_E^2 + \Omega^2) + \text{constant} \tag{22a}$$

and

$$I_0(\Omega) = \frac{1}{(2\pi)^4}\int \mathrm{d}^4 k_E \frac{1}{(k_E^2 + \Omega^2)}. \tag{22b}$$

Differentiating (21) with respect to Ω_N^2, Ω_1^2, Ω_3^2, Ω_5^2 and Ω_8^2 gives us five mass equations:

$$\Omega_N^2 = M_N^2 + \tfrac{1}{2}h^2[3I_0(\Omega_1^2) + 3I_0(\Omega_5^2) + I_0(\Omega_3^2) + I_0(\Omega_8^2)], \tag{23a}$$

$$\Omega_1^2 = M_1^2 + \tfrac{1}{4}h^2[4I_0(\Omega_N^2) + 5I_0(\Omega_1^2) + I_0(\Omega_3^2) - I_0(\Omega_5^2) - I_0(\Omega_8^2)], \tag{23b}$$

$$\Omega_3^2 = M_3^2 + \tfrac{1}{4}h^2[4I_0(\Omega_N^2) + 3I_0(\Omega_1^2) + 3I_0(\Omega_3^2) - 3I_0(\Omega_5^2) + I_0(\Omega_8^2)], \tag{23c}$$

$$\Omega_5^2 = M_5^2 + \tfrac{1}{4}h^2[4I_0(\Omega_N^2) - I_0(\Omega_1^2) - I_0(\Omega_3^2) + 5I_0(\Omega_5^2) + I_0(\Omega_8^2)], \tag{23d}$$

$$\Omega_8^2 = M_8^2 + \tfrac{1}{4}h^2[4I_0(\Omega_N^2) - 3I_0(\Omega_1^2) + I_0(\Omega_3^2) + 3I_0(\Omega_5^2) + 3I_0(\Omega_8^2)]. \tag{23e}$$

Using equations (23), V_{G} reduces to

$$\begin{aligned} V_{\mathrm{G}} =& (m^2 - m_3^2)v^2 + \tfrac{1}{4}h^2 v^4 \\ &+ [2I_1(\Omega_N^2) + 3I_1(\Omega_1^2) + I_1(\Omega_3^2) + 3I_1(\Omega_5^2) + I_1(\Omega_8^2)] \\ &- \tfrac{3}{16}h^2[5I_0^2(\Omega_1^2) + I_0^2(\Omega_3^2) + 5I_0^2(\Omega_5^2) + I_0^2(\Omega_8^2)] \\ &- \tfrac{1}{2}h^2 I_0(\Omega_N^2)[3I_0(\Omega_1^2) + I_0(\Omega_3^2) + 3I_0(\Omega_5^2) + I_0(\Omega_8^2)] \\ &- \tfrac{1}{8}h^2[3I_0(\Omega_1^2)(I_0(\Omega_3^2) - I_0(\Omega_5^2) - I_0(\Omega_8^2)) \\ &+ 3I_0(\Omega_5^2)(I_0(\Omega_8^2) - I_0(\Omega_3^2)) + I_0(\Omega_3^2)I_0(\Omega_8^2)]. \end{aligned} \tag{24}$$

Here Ω_i's are to be understood as depending on v through (23). Differentiating V_{G} with respect to v^2, we get

$$\begin{aligned} \frac{\mathrm{d}V_{\mathrm{G}}}{\mathrm{d}v^2} =& m^2 - m_3^2 + \frac{1}{2}h^2 v^2 + \frac{1}{4}h^2 \\ &\times [4I_0(\Omega_N^2) + 3I_0(\Omega_1^2) + 3I_0(\Omega_3^2) - 3I_0(\Omega_5^2) + I_0(\Omega_8^2)]. \end{aligned} \tag{25}$$

Setting $\mathrm{d}V_{\mathrm{G}}/\mathrm{d}v^2$ to zero and using (23c), we get

$$\Omega_3^2 = h^2 v^2. \tag{26}$$

It is clear from (25), that increasing h would increase Ω_3^2 without limits. However, the limit would be set by demanding that stationary solution (25) be stable, i.e. the stability matrix $(\partial^2 V_{\mathrm{G}})$ be positive definite. Stability condition is obtained by considering $(\partial^2 V_{\mathrm{G}})$ to be a function of six variables — five mass parameters (Ω_1^2, Ω_3^2, Ω_5^2, Ω_8^2 and Ω_N^2) and v^2, and demanding all its eigenvalues to be positive. As in the case of standard model [8], we expect that as h increases, this condition would no longer be satisfied beyond a certain maximum value of h.

Our query regarding triviality bounds does not involve the complete numerical solution. Of five independent masses $\Omega_1, \Omega_3, \Omega_5, \Omega_8$ and Ω_N, Ω_1 is the mass of the Goldstone bosons. This in an exact calculation is expected to be zero but in variational methods (see ref. [13] for elaboration), we can get a small but non-vanishing mass. Of the remaining four Higgs masses, we wish to find out whether they can be made arbitrarily heavy relative to v^2 (or M_{W}^2). The only condition we would impose is the same as laid down by Hasenfratz and Nager, namely that for a cut-off theory to make any physical sense, each one of the masses Ω_i must not be close to or greater than the cut-off; we put an upper limit of $\Lambda_{\mathrm{c}}/5$ for definiteness, for all Ω_i's (see ref. [5]).

Our task is then to set Ω_i's at their maximum possible values and determine the value of h for which the eigenvalues of stability matrix go from positive to negative. Since there are only three mass input parameters m, m_3 and m_4, all the five Ω_i's cannot be assigned arbitrary values by suitably choosing m's. Furthermore, only Ω_N^2 involves m_4^2, so that we can set Ω_N as the highest acceptable mass namely $\Lambda_{\mathrm{c}}/5$ right away. Of the remaining four masses, we immediately have the sum rule,

$$\begin{aligned}\Omega_8^2 - \Omega_5^2 &= \Omega_3^2 - \Omega_1^2 \\ &= h^2 v^2 + \frac{h^2}{2}[I_0(\Omega_3^2) - I_0(\Omega_1^2) + I_0(\Omega_8^2) - I_0(\Omega_5^2)].\end{aligned} \tag{27}$$

Also since $I_0(\Omega^2)$ is a decreasing function of Ω^2, we get from (23) and (27)

$$\Omega_8^2 > \Omega_5^2 \quad \text{and} \quad \Omega_3^2 > \Omega_1^2.$$

The first possibility is to set

$$\Omega_8 = \Omega_3 = \Lambda_{\mathrm{c}}/5;$$

Ω_1 is the Goldstone and Ω_5 is then the lightest Higgs mass. However in this case $\Omega_5 = \Omega_1$, and the maximum value of Ω_5 turns out to be lower than in the next sequence of masses.

Next we assume $\Omega_8 = \Lambda_{\mathrm{c}}/5$ and the sequence

$$\Omega_8 > \Omega_5 > \Omega_3 > \Omega_1.$$

In this Ω_3 is the lightest Higgs. From (27), pushing Ω_5 towards Ω_8 will make Ω_3 go towards Ω_1, i.e. will make Ω_3 lighter. We then expect some kind of optimal situation to arise if $\Omega_5 = \Omega_3$. With the values of Ω_3 (obtained from (23)) corresponding for various h, Using this value, then the upper bound on mass of the lightest Higgs $M_{\rm LH} = \Omega_3 = \Omega_5$ is

$$\frac{M_{\rm LH}|_{\rm max}}{M_{\rm W}} = 10.1. \qquad (29)$$

The Goldstone mass Ω_1 for this choice, as we stated before, is not zero but smaller than other masses in the spectrum.

4. Conclusion

We have shown that in a certain range of parameters of the NMSSM, the triviality upper bound on the mass of the lightest Higgs particle is $\sim 10\,M_{\rm W}$. Relaxing restrictions on the parameters can lead to even larger masses for the lightest Higgs. We have however not attempted to determine the absolute bound taking into account the full range of variation of parameters in the NMSSM (including SUSY breaking parameters). This is because our main aim was to show that in the non-minimal version of supersymmetric model, one need not be constrained by the rather strict limits on the Higgs mass that one obtains in the minimal model.

We would also like to comment on the upper bound of about 140 GeV for the lightest Higgs boson mass obtained by several authors [14]. This arises by the requirement that the SUSY theory remain perturbative up to some scale $M_{\rm GUT} \sim 10^{15}$ GeV. This clearly forces the quartic coupling constant to remain small. From a phenomenological point of view where the couplings of the NMSSM model have to be realistic over a huge energy range, such restrictions are eminently reasonable and hence in that respect the bounds obtained by reference [14] are phenomenologically more relevant. We, in our analysis, have not constrained the coupling constant from any such requirement and thus the limits obtained are much higher. Comparing our result with that of Wu [11] who obtained a much lower bound by a factor of four, we find that the criterion used by him to define triviality bound (as explained in the introduction) is different from ours. Also the method of calculating the scalar mass particles is based on tree approximation unlike our non-perturbative variational method which goes beyond the tree approximation. The difference in our numerical bounds we believe can be attributed to these differences in our approaches. Also limits on the Higgs mass above 1 TeV are of little interest. There is no possibility in any near future to detect any signals for such a heavy Higgs. Moreover Higgs particle with masses above 1 TeV with widths comparable to masses will make the mass parameter rather meaningless from an experimental point of view. Further, it is interesting to note that the bound obtained for the lightest Higgs ($\sim 10\,M_{\rm W}$) is of the same order as the bounds in the SM suggesting that in a supersymmetric theory, the Higgs mass bounds have the same features as the regular SM.

References

[1] T P Cheng and L F Li, *Gauge theory of elementary particle physics* (Clarendon Press, Oxford, 1986) pp. 84

[2] R Dashen and H Neuberger, *Phys. Rev. Lett.* **50**, 1897 (1983)

[3] P M Stevenson, *Phys. Rev.* **D32**, 1389 (1985)

[4] For a summary, see K Huang, MIT preprint, CTP # 1631 (1988)

[5] P Hasenfratz and J Nager, *Z. Phys.* **C37**, 477 (1988)
[6] M Luscher and P Weisz, *Nucl. Phys.* **B290**, 25 (1987); **B295**, 65 (1988)
[7] A Hasenfratz *et al*, *Phys. Lett.* **B199**, 531 (1987)
J Kuti, L Lin and Y Shen, *Phys. Rev. Lett.* **61**, 678 (1988)
[8] S R Choudhury and Mamta, *Int. J. Mod. Phys.* **A12**, 1847 (1997)
[9] See e.g. J F Gunion, H E Haber, G Kane and S Dawson, *The Higgs Hunter's Guide* (Addison-Wesley, 1990)
[10] M Quiros, CERN preprint, CERN-TH. 7507/94 (November, 1994)
[11] Y Y Wu, *Phys. Rev.* **D51**, 5276 (1995)
[12] J F Gunion and H E Haber, *Nucl. Phys.* **B272**, 1 (1986)
[13] P M Stevenson, B Allès and R Tarrach, *Phys. Rev.* **D35**, 2407 (1987)
[14] B Ananthanarayan and P Pandita, *Phys. Lett.* **B353**, 566 (1996); *Phys. Lett.* **B371**, 245 (1996)

Measurement and analysis of the excitation function and isomeric cross section ratios for α-induced reaction on Ir, Au, Re and Ta nuclei

M ISMAIL
Variable Energy Cyclotron Centre, I/AF, Bidhan Nagar, Calcutta 700 064, India
Email: ismail@veccal.ernet.in

MS received 3 December 1996; revised 18 June 1997

Abstract. Excitation functions and a few isomeric cross-section ratios for production of (1) ^{192}Au, ^{193}Au, ^{194}Au, ^{195}Au and ^{192}Ir nuclides in α-induced reactions on ^{191,193}Ir, (2) ^{197}Tl, ^{197m}Hg, ^{198m,g}Tl, ^{199}Tl and ^{200}Tl nuclides in α-induced reaction in ^{197}Au and (3) ^{183}Re and ^{184m,g}Re nuclides in α-induced reaction in ^{181}Ta and ^{185}Re are obtained from the measurements of the residual activities by the conventional stacked-foils technique from threshold to 50 MeV. The excitation function and isomeric cross-section ratios for nuclear reaction ^{181}Ta$(\alpha, n)^{184m,g}$Re are compared with the theoretical calculation using the code Stapre which is based on exciton model for pre-equilibrium phase and Hauser–Feshbach formalism taking angular momentum and parity into account for the equilibrium phase of the nuclear reaction. All other experimental excitation functions are compared with the calculations considering equilibrium as well as pre-equilibrium reaction mechanism according to the geometry dependent hybrid (GDH) model and hybrid model of Blann using the code Alice/91. The high energy part of the excitation functions are dominated by pre-equilibrium reaction mechanism whereas the low energy parts are dominated by equilibrium evaporation with its characteristic peak. The GDH model provides a potentially better description of the physical process (i.e., a higher probability for peripheral collisions to undergo precompound decay than for central collisions) compared to hybrid model. However in the energy range of present measurement most of the excitation functions are fitted reasonably well by both GDH model and hybrid model with initial exciton number $N_0 = 4(N_n = 2, N_p = 2, N_h = 0)$. Barring a few reactions we have found the overall agreement between theory and experiment is reasonably good taking the limitations of the theory into account.

Keywords. α-induced reactions on Ir, Au, Re and Ta; stacked foil technique; isotope production; equilibrium and pre-equilibrium decays; Stapre and Alice/91 codes.

PACS No. 25.60

1. Introduction

It is well known that the compound statistical model coupled with the exciton model gives a correct overall description of the excitation functions and particle energy spectra in nuclear reactions at medium energies. However, the calculations partially fail to account for details such as the exact position of the maximum or the slope of the ascending and descending part of the excitation functions. The high energy parts of the excitation functions are dominated by pre-equilibrium reaction mechanism whereas the low energy parts are dominated by evaporation with its characteristic peak. The pre-equilibrium processes have been investigated by several authors [1–6]. Excitation functions for equilibrium and pre-equilibrium reactions have been studied in (α, xn) and (α, pxn) reactions [7–10]. Theoretical calculations for pre-equilibrium process have been carried out in terms of exciton models [1–3]. Several models [1–6, 11–15] have been proposed to explain the emission of energetic light particles by the equilibration process from the nuclear system excited at medium energies. Predictions from these models with regard to excitation functions and the energy spectra of the emitted particles compared well with the existing experimental data. This has prompted a continued interest in these models as tools both to predict cross-sections for a number of nuclear reactions for practical purposes and to test the adequacy of the underlying physics. The isomeric cross-section ratios for a pair of isomeric states are known to depend strongly on the spins of the isomers concerned as well as on the spins of the higher lying levels populating the isomers. Experimental and theoretical studies on the isomeric cross-section ratios specially as function of incident particle energy should therefore lead to useful information on the spin cut off parameter as well as on the level structure of the residual nuclei. The excitation functions and isomeric cross-section studies are significant for the investigation of the mechanism of nuclear reactions. The present work on alpha induced reactions on the target nuclei ^{181}Ta, ^{185}Re, ^{191}Ir and ^{193}Ir is also intended to supply some new data in the alpha energy range from threshold to 50.0 MeV. Since the nuclear reactions $^{197}\mathrm{Au}(\alpha, xnypz\alpha)$ have already been studied extensively by several authors (see [16] and references therein), we have measured the cross-sections and the isomeric cross-section ratios for $^{197}\mathrm{Au}(\alpha, xnypz\alpha)$ reactions so as to standarize our measurements by comparing our measurements with previous measurements. Hence the nuclear reactions $^{197}\mathrm{Au}(\alpha, xnypz\alpha)$ have not been given much importance for theoretical analysis. However the nuclear reaction cross-sections are being presented in this paper only for completeness.

This paper continues a series of reports on gross features of the interactions of intermediate energy light projectile with medium and heavy nuclei. The experiments have been performed at the Variable Energy Cyclotron Centre, Calcutta. Several excitation functions for the reactions $^{191,193}\mathrm{Ir}(\alpha, xn)$ $^{195-x,197-x}\mathrm{Au}$, $^{191}\mathrm{Ir}(\alpha, \alpha n)\,^{192}\mathrm{Ir}$, $^{197}\mathrm{Au}(\alpha, xn)\,^{200-x}\mathrm{Tl}$, $^{197}\mathrm{Au}(\alpha, p3n)\,^{197}\mathrm{Hg}$, $^{185}\mathrm{Re}(\alpha, \alpha n)\,^{184}\mathrm{Re}$ and $^{181}\mathrm{Ta}(\alpha, xn)\,^{185-x}\mathrm{Re}$ measured by the stacked foil technique are presented. The excitation functions of the radioactive products observed in reactions contain some information about the mechanism of the interaction of the α-particles with Ir, Ta Re and Au nuclei. In this work calculations in the framework of the equilibrium statistical model and pre-equilibrium model using the code Alice/91 [17] and Stapre [18] were performed and the results are compared with experimental excitation functions. The Stapre code [18] which is based on exciton model for pre-equilibrium phase and Hauser–Feshbach formalism taking angular momentum and parity into account for the equilibrium phase has been used to calculate isomeric cross-section ratios and the results are compared with the measured isomeric cross-section ratios.

2. Experimental procedure

Excitation functions for alpha induced reactions on ^{181}Ta, ^{191}Ir, ^{193}Ir and ^{197}Au were determined using the absolute yields of characteristic γ-rays pertaining to the decay of each radioactive residual nuclide as usually done in stacked foil technique. The targets were commercially available thin self-supporting foils. The thicknesses of gold foils were 4.837 μm, that of irridium foils 13.021 μm, and tantalum foils were 10.521 μm obtained by weighing. Then the stacks were irradiated in a chamber (as shown in figure 1 of [9]) specially constructed for this purpose having the facility to irradiate up to four stacks one after another. The beam spot on the targets was limited to 5.0 mm in diameter by using a 10.0 cm long aluminum collimator in front of the targets. The Au and Ta stack consisted of about 20 targets whereas Ir stack consisted of about 15 targets. Since the Au foils were very thin, these were interspersed with 23.4 μm thick Al degrader-cum-catcher foils. The stacks were exposed to the unanalysed external beam from the 224 cm variable energy cyclotron in Calcutta. The beam current on the targets was kept below 200 nA. The total α-particle beam was collected and measured using a calibrated ORTEC current integrator. The absolute cross-sections for the reactions $^{197}\mathrm{Au}(\alpha, xnyp\alpha z)$ were also compared with previous measurements [16]. The cross-section for the α-induced reaction on Au are very well known [16]. Comparison of ^{200}Tl, ^{199}Tl and ^{198}Tl production cross-section from previous measurements with our measurements thus provides high reliability to the absolute cross-section measurements. The unanalysed beam energy resolution was $\simeq$ 0.2 MeV. The accuracy in absolute energy is expected to be $\cong$ 2.0 MeV. However from some of the excitation functions for the α-induced reactions on Au the energies were re-calibrated with respect to their thresholds and thereby improving the accuracy in absolute energy to $\cong$ 0.5 MeV.

The mean beam energy at the half-thickness of each target of a stacked foil assembly was calculated from the energy degradation of the initial beam energy according to the given stopping power values for different materials. We have used the stopping powers from the tabulated values of Williamson *et al* [19]. However the tabulated values are in multiple of 2.0 MeV up to 50.0 MeV and in steps of 5.0 MeV thereafter. Therefore interpolation is required at every foil of the stack. To improve the accuracy of interpolation the stopping powers $S(E)$ are fitted by a non-linear least square method to a function of the form:

$$S(E) = \sum_{i=1,4} A_i \cdot E^{i-1} + \sum_{k=1,2} B_k \cdot \exp(-C_k \cdot E), \tag{1}$$

where A_i, B_k and C_k are the constants to be determined from non-linear least square fit. The fit improves the overall accuracy of the stopping power interpolation. The average thicknesses of the target and degrader foils were determined by weighing. Each foil was cut out into a square shape and pasted over an annular Al ring having 30.0 mm as the outer diameter.

The γ-rays emitted by the activated foils were detected either with a Ge(Li) detector or with a HPGe detector (both having 30% efficiency) available at our centre. In most of the cases the γ-rays, used in yield determination as listed in table 1, stand out very prominently in the spectra and does not pose any identification problem. The γ-ray spectra from the Ge(Li) and HPGe detectors were analysed using personal computer based multi channel analyser and were stored on hard disk or floppy diskettes. The Super-32 computer was used to analyse the γ-ray spectra stored on these hard disk and floppy diskettes. One program EXPANL1 was written to select the required peaks from the γ-ray spectra stored on hard disk and floppy diskettes and prepare a data file EXP2DT. Another program ISABELLE written by Kern [20, 21] (modified and renamed as EXPANL2) was

Table 1. Half-lives, γ-energies, branching ratios of the γ-decays and Q-values for α-induced reactions on Ir, Au, Re and Ta.

Nuclide	Half-lives	E_γ (keV)	I_γ(%)	Reaction	Q-values (MeV)
^{92}Au	4.94 h	316.51	58.00	^{191}Ir(α, 3n)	−25.709
				^{193}Ir(α, 5n)	−39.679
^{93}Au	17.65 h	186.17	10.11	^{191}Ir(α, 2n)	−16.944
				^{193}Ir(α, 4n)	−30.914
^{94}Au	38.02 h	328.50	60.00	^{191}Ir(α, n)	−10.084
				^{193}Ir(α, 3n)	−24.054
^{95}Au	186.09 d	98.88	10.90	^{193}Ir(α, 2n)	−15.670
^{92}Ir	73.83 d	316.51	82.81	^{193}Ir(α, 2p3n)	−36.053
				^{193}Ir(α, αn)	−7.757
				^{191}Ir(α, 2pn)	−22.084
^{97}Tl	2.84 h	425.84	12.91	^{197}Au(α, 4n)	−32.606
		152.23	07.21	^{197}Au(α, 4n)	−32.606
^{97m}Hg	23.80 h	133.96	34.00	^{197}Au(α, p3n)	−29.678
^{98g}Tl	5.30 h	411.80	82.10	^{197}Au(α, 3n)	−25.434
^{98m}Tl	1.87 h	282.80	28.00	^{197}Au(α, 3n)	−25.434
^{99}Tl	7.42 h	455.46	12.31	^{197}Au(α, 2n)	−16.813
		208.21	12.21	^{197}Au(α, 2n)	−16.813
^{00}Tl	26.10 h	367.94	87.20	^{197}Au(α, n)	−09.736
^{83}Re	71.20 d	162.33	23.58	^{181}Ta(α, 2n)	−16.340
^{84g}Re	38.00 d	792.07	37.64	^{181}Ta(α, n)	−09.873
^{84m}Re	169.8 d	252.85	10.89	^{181}Ta(α, n)	−09.873
^{84g}Re	38.00 d	792.07	37.64	^{185}Re(α, 2p3n)	−35.975
^{84m}Re	169.8 d	252.85	10.89	^{185}Re(α, 2p3n)	−35.975
				^{185}Re(α, αn)	−07.679

h = hour, d = days, y = year.

used to analyse the peaks stored in the data file EXP2DT. The program ISABELLE fits the γ-ray spectra very well (see figure 2d in [9]). The integration of the analytical function as well as experimental peak was used for yield determination. The γ-ray yield was determined by integrating the experimental peak points and subtracting the calculated background from it.

The efficiency calibrations of the detector were done with a standard ^{152}Eu and ^{133}Ba radioactive source obtained from B.R.I.T. (Department of Atomic Energy) available at our centre. The efficiency of the detector was interpolated to the required energy value from the measured efficiency curve. However to improve the interpolation, the efficiency curve was similarly fitted by a non-linear least square method to a function of the form given in (1). The range of the fit was from 122 keV to 1408 keV. The fit improves the accuracy of interpolation considerably. For γ-ray having energy $E_\gamma < 122$ keV, the efficiency of the detector was extracted by manually plotted efficiency curve using low energy γ-rays from ^{152}Eu and ^{133}Ba calibrated sources.

The nuclear data necessary for the evaluation of the cross-sections are presented in table 1. The half-lives of the radioactive atoms are taken from the chart of nuclides [22], the γ-ray energies and branching ratios are taken from the table of isotopes [22]. In table 1, only those γ-rays are listed which were chosen for the calculation of the cross-sections. Also included in table 1 are reaction Q-values. Q-values were calculated using the atomic mass table of Wapstra and Audi [23].

2.1 *Cross-section determination*

The number of observed decays Z per unit time is related to the total number of decays Z_0 per unit time by

$$Z_0 = Z/[\varepsilon(E_\gamma) * I_\gamma(\mathrm{abs})], \tag{2}$$

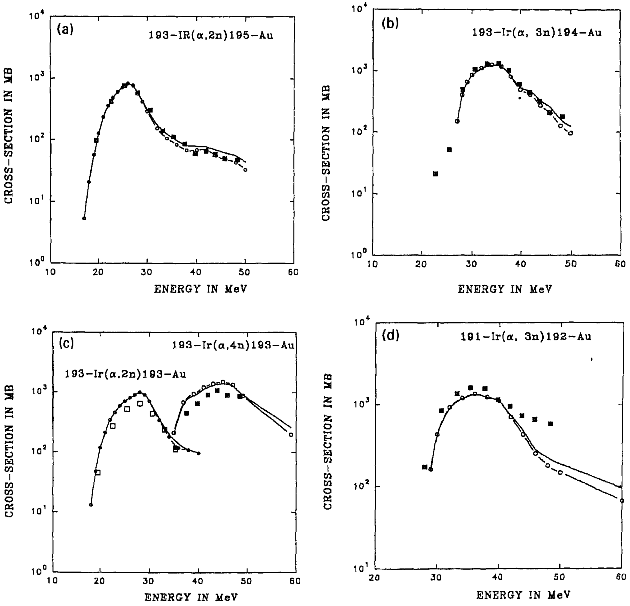

Figure 1a–d. The total residual production cross-section in mb for the reactions **(a)** ^{193}Ir(α, $2n$)^{195}Au (■), **(b)** ^{193}Ir(α, $3n$)^{194}Au (■), **(c)** $^{(193),191}$Ir[α, ($4n$) $2n$]^{193}Au [(■), □] and **(d)** ^{191}Ir(α, $3n$)^{192}Au (■) are plotted as a function of α-particle bombarding energy. The solid line is the geometry dependent hybrid model and the circle-line (–○–) is the hybrid model fits using the code Alice/91 with $N_0 = 4, N_n = 2, N_p = 2$ and $N_h = 0$.

where $\epsilon(E_\gamma)$ is the detector efficiency and I_γ(abs) is the absolute γ-ray abundance per decay. The total number of decays, Z_0, is related to total reaction yield R for simple decays (simple decays correspond to direct production of radio isotopes by the nuclear reactions and we have used only such decays in all the measurements reported here) by the relation

$$R = Z_0 \cdot \exp(\lambda T_2)/[(1-\exp(-\lambda T)) \cdot (1-\exp(-\lambda T_1))/\lambda T_1], \tag{3}$$

where λ is the decay constant, T_1 the irradiation time, T_2 the cooling time after the end of irradiation and the beginning of the measurement, T the counting time and R is related to the cross-section σ by the relation

$$\sigma = R/[(N_A \cdot \delta x) \cdot \mathcal{J}], \tag{4}$$

Table 2. Experimental cross-section for α-induced reaction with ^{191}Ir and ^{193}Ir.

Energy in (MeV)	From ^{191}Ir		
	192-Au (3*n*)	193-Au (2*n*)	194-Au (*n*)
48.4 ±0.9	580.62 ±0.30%		
45.8 ±1.0	656.41 ±0.70%		
43.8 ±1.0	727.27 ±0.80%		
41.9 ±1.0	939.84 ±0.70%		
39.7 ±1.1	1141.51 ±0.40%		
37.6 ±1.1	1562.89 ±0.30%		
35.4 ±1.1	1602.75 ±0.30%	110.9* ±0.80%	
33.1 ±1.2	1349.15 ±0.40%	236.26 ±1.50%	
30.7 ±1.2	841.48 ±0.60%	438.09 ±2.50%	23.3* ±0.15%
28.1 ±1.3	172.789 ±2.10%	640.60 ±1.40%	29.8* ±0.24%
25.4 ±1.4		522.11 ±0.30%	32.7* ±0.80%
22.6 ±1.5		269.65 ±0.30%	35.6 ±1.60%
19.5 ±1.6		45.74 ±0.70%	33.64 ±1.00%
16.1 ±1.8			3.14 ±1.00%

Table 2. *(Continued)*

Energy in (MeV)	Cross-section of the product in milli barns from ^{193}Ir			
	195-Au $(2n)$	192-Ir (αn)	194-Au $(3n)$	193-Au $(4n)$
48.4 ±0.9	47.06 ±8.20%	196.998 ±0.46%	179.462 ±1.30%	854.336 ±2.00%
45.8 ±1.0	49.72 ±5.27%	83.863 ±0.46%	207.039 ±1.10%	899.380 ±3.00%
43.8 ±1.0	57.23 ±5.30%	52.057 ±1.00%	320.463 ±0.90%	1077.775 ±1.00%
41.9 ±1.0	64.28 ±4.00%	37.069 ±0.69%	445.464 ±0.60%	904.602 ±0.80%
39.7 ±1.1	59.18 ±5.00%	28.935 ±1.50%	608.938 ±0.30%	644.735 ±0.60%
37.6 ±1.1	84.80 ±2.60%	25.356 ±1.70%	1028.389 ±0.16%	441.116 ±0.60%
35.4 ±1.1	110.63 ±2.54%	18.491 ±1.75%	1342.906 ±0.08%	118.3* ±1.80%
33.1 ±1.2	139.56 ±2.07%	11.801 ±3.07%	1318.248 ±0.12%	
30.7 ±1.2	303.44 ±0.96%	6.505 ±6.10%	1061.1 ±0.15%	
28.1 ±1.3	580.44 ±0.52%	4.193 ±9.10%	478.3* ±0.24%	
25.4 ±1.4	757.07 ±0.42%	2.053 ±9.90%	17.0* ±0.80%	
22.6 ±1.5	426.80 ±0.93%	1.686 ±10.0%		
19.5 ±1.6	97.49 ±2.73%	1.686 ±10.0%		

where N_A is the number of atoms/cm^3 of the target material, δx is the thickness of the foil (in cm) and $\mathcal{J}$ is the total number of incident particles during the irradiation (calculated from total charge measured by current integrator).

3. Experimental results

In table 2 and figures (1a) to (1d) our experimental results for the production of ^{192}Au, ^{192}Ir, ^{193}Au, ^{194}Au and ^{195}Au radio-nuclides via α-induced reactions on ^{191,193}Ir are summarized and plotted as a function of α-particle bombarding energy. The experimental cross-sections are in millibarns and presented along with the percentage of statistical errors only. Since the radio-nuclides ^{193}Au could be produced by $^{191}\mathrm{Ir}(\alpha, 2n)$ and $^{193}\mathrm{Ir}(\alpha, 4n)$ reactions and the radio-nuclides ^{194}Au could be produced by $^{191}\mathrm{Ir}(\alpha, n)$ and $^{193}\mathrm{Ir}(\alpha, 3n)$ reactions, in the overlapping regions the cross-sections for these reactions are taken as proportional to their theoretical values based on the GDH model calculation [6].

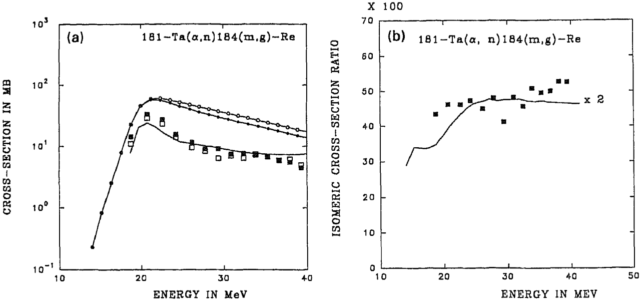

Figure 2. (**a**) The total residual production cross-section in mb for the reaction $^{181}\mathrm{Ta}(\alpha, n)^{184m,g}\mathrm{Re}$ [■ $\Rightarrow g$, □ $\Rightarrow m$] are plotted as a function of α-particle bombarding energy. The solid line is the geometry dependent hybrid model fit using the code Alice/91 with $N_0 = 4, N_n = 2, N_p = 2$ and $N_h = 0$. The -•- and -○- are Stapre code calculation with $FM = 1000.0\,(\mathrm{MeV})^3$ and $FM = 750\,(\mathrm{MeV})^3$ respectively. (**b**) The isomeric cross-section ratios for the isomer pair $^{184m,g}\mathrm{Re}$ are plotted (■) as a function of α-particle bombarding energy. The solid lined curve is Stapre code calculation with $FM = 1000\,(\mathrm{MeV})^3$. The curve with $FM = 750\,(\mathrm{MeV})^3$ is indistinguishable with the plotted solid curve.

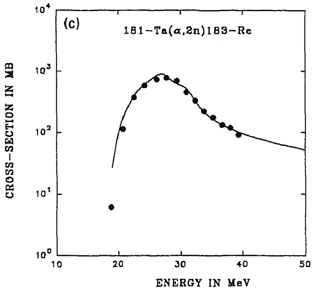

Figure 2c. The total residual production cross-section in mb for the reaction $^{181}\mathrm{Ta}(\alpha, 2n)^{183}\mathrm{Re}$ (•) are plotted as a function of α-particle bombarding energy. The solid line is the geometry dependent hybrid model fit using the code Alice/91 with $N_0 = 4, N_n = 2, N_p = 2$ and $N_h = 0$.

These points are marked with symbols (*) in table 2 and beyond these marked points the contributions of (α, n) and $(\alpha, 2n)$ reactions to $(\alpha, 3n)$ and $(\alpha, 4n)$ reactions respectively are negligible ($< 2\%$). The number of such points for $(\alpha, 2n)$ and $(\alpha, 4n)$ reactions is

Table 3. Experimental cross-section for α-induced reaction with ^{181}Ta.

Energy in (MeV)	Cross-section of the product in milli barns			
	183-Re	184-Re (g)	184-Re (m)	$\sigma_m/(\sigma_g + \sigma_m)$
18.8 ±1.0	6.09 ±1.5%	14.45 ±0.63%	11.07 ±3.0%	0.434
20.7 ±1.0	114.23 ±0.3%	33.50 ±0.69%	28.76 ±2.6%	0.462
22.6 ±0.9	375.89 ±0.09%	27.23 ±0.48%	23.36 ±2.1%	0.462
24.2 ±0.8	581.04 ±0.11%	15.78 ±1.08%	14.17 ±6.3%	0.473
26.2 ±0.8	730.62 ±0.08%	11.62 ±0.11%	9.50 ±7.4%	0.450
27.8 ±0.8	772.58 ±0.05%	9.07 ±0.81%	8.38 ±7.3%	0.480
29.4 ±0.8	698.82 ±0.11%	9.13 ±1.52%	6.41 ±10.0%	0.412
30.9 ±0.8	457.57 ±0.13%	7.54 ±1.69%	7.03 ±9.4%	0.482
32.5 ±0.8	334.07 ±0.15%	7.65 ±1.62%	6.43 ±7.8%	0.457
33.9 ±0.7	224.18 ±0.18%	7.14 ±1.72%	7.36 ±8.7%	0.508
35.3 ±0.7	177.45 ±0.20%	6.87 ±1.73%	6.73 ±7.9%	0.495
36.7 ±0.7	132.90 ±0.24%	5.86 ±1.91%	5.87 ±5.8%	0.500
38.0 ±0.7	118.90 ±0.26%	5.48 ±2.03%	6.11 ±7.3%	0.527
39.3 ±0.7	91.25 ±0.28%	4.47 ±2.20%	4.97 ±9.2%	0.526

Table 4. Experimental cross-section for α-induced reaction with ^{185}Re.

Energy in (MeV)	Cross-section of the product in milli barns		
	184-Re (g)	184-Re (m)	$\sigma_m/(\sigma_g + \sigma_m)$
32.6 ± 2.0	3.83 ± 5.0%	4.07 ± 10.0%	0.515
36.6 ± 2.0	4.29 ± 4.8%	5.28 ± 10.0%	0.552
40.5 ± 2.0	12.11 ± 1.8%	11.67 ± 9.0%	0.491
44.2 ± 1.8	18.33 ± 0.45%	18.73 ± 3.3%	0.505
47.6 ± 1.7	26.15 ± 0.55%	28.00 ± 4.2%	0.517

only one and for (α, n) and $(\alpha, 3n)$ reactions three. Since no data exist in literature for α-induced reactions on ^{191,193}Ir, comparison could not be made with other measurements. In table 3 and figures 2a and 2c the total residual production cross-section in mb for

Table 5. Experimental cross-section for α-induced reaction with ^{197}Au.

Energy in (MeV)	Cross-section of the product in milli barns				
	200-Tl	199-Tl	198-Tl (g)	198-Tl (m)	$\sigma_m/(\sigma_m+\sigma_g)$
52.0 ± 0.3	1.95 ± 1.9%	37.29 ± 3.8%	174.15 ± 0.3%	254.18 ± 8.6%	0.594
50.7 ± 0.3	2.16 ± 1.7%	45.12 ± 3.0%	211.19 ± 0.3%	328.57 ± 7.1%	0.608
49.4 ± 0.3	2.18 ± 1.7%	44.50 ± 3.1%	232.51 ± 0.4%	337.97 ± 5.9%	0.592
48.0 ± 0.3	2.43 ± 1.8%	47.79 ± 2.3%	289.24 ± 0.2%	433.42 ± 3.3%	0.600
46.6 ± 0.3	2.52 ± 1.8%	51.45 ± 1.6%	364.37 ± 0.2%	521.26 ± 2.6%	0.589
45.1 ± 0.3	2.43 ± 1.7%	48.96 ± 1.4%	406.23 ± 0.2%	735.08 ± 2.7%	0.644
43.6 ± 0.3	2.88 ± 1.6%	57.17 ± 0.8%	564.90 ± 0.18%	990.33 ± 1.8%	0.637
42.1 ± 0.3	3.08 ± 1.7%	65.55 ± 1.2%	750.94 ± 0.3%	1230.85 ± 1.4%	0.621
40.6 ± 0.3	3.82 ± 0.5%	82.25 ± 0.8%	959.55 ± 0.2%	1417.20 ± 1.2%	0.596
38.8 ± 0.3	4.40 ± 0.6%	101.29 ± 0.9%	1059.09 ± 0.2%	1518.60 ± 1.0%	0.589
37.2 ± 0.4	4.90 ± 0.6%	129.20 ± 0.56%	1011.62 ± 0.2%	1485.62 ± 1.0%	0.595
35.5 ± 0.4	5.50 ± 0.6%	184.27 ± 0.5%	925.02 ± 0.2%	1266.36 ± 0.8%	0.578
33.7 ± 0.4	7.49 ± 0.5%	317.88 ± 0.3%	783.06 ± 0.3%	1023.21 ± 1.3%	0.567
31.8 ± 0.4	7.03 ± 0.7%	485.13 ± 0.2%	483.44 ± 0.4%	612.74 ± 1.9%	0.559
29.9 ± 0.4	8.28 ± 0.5%	723.71 ± 0.16%	196.75 ± 0.4%	208.55 ± 0.6%	0.515
27.8 ± 0.4	9.32 ± 0.2%	710.79 ± 0.16%	23.65 ± 2.2%	15.44 ± 2.0%	0.390
26.5 ± 0.4	9.61 ± 0.22%	708.60 ± 0.4%			
25.6 ± 0.4	10.58 ± 0.4%	649.12 ± 0.4%			
25.6 ± 0.4	12.53 ± 0.8%	571.78 ± 0.2%			
24.8 ± 0.5	12.10 ± 0.2%	554.83 ± 0.5%			
24.0 ± 0.5	15.19 ± 0.4%	500.91 ± 0.4%			
23.3 ± 0.5	16.86 ± 0.5%	345.53 ± 0.33%			
23.1 ± 0.5	19.90 ± 0.9%	362.57 ± 1.0%			
22.2 ± 0.5	22.32 ± 0.2%	282.92 ± 0.9%			
21.0 ± 0.5	26.88 ± 0.8%	173.76 ± 0.86%			
20.8 ± 0.5	27.84 ± 0.1%	119.30 ± 1.2%			
20.3 ± 0.5	27.84 ± 0.6%	90.50 ± 0.8%			
19.4 ± 0.5	20.82 ± 1.0%	29.79 ± 0.9%			
18.4 ± 0.5	10.73 ± 0.5%	9.41 ± 6.4%			
18.0 ± 0.5	11.78 ± 0.1%	5.57 ± 0.6%			
17.4 ± 0.6	3.29 ± 0.2%	0.38 ± 2.4%			
16.4 ± 0.6	0.54 ± 0.5%				
15.4 ± 0.6	0.06 ± 7.9%				

Energy in (MeV)	Cross section in milli barns	
	197-Tl	197-Hg (m)
52.0 ± 0.3	1160.30 ± 2.0%	68.85 ± 1.2%
50.7 ± 0.3	1242.39 ± 1.7%	65.10 ± 1.3%
49.4 ± 0.3	1242.13 ± 2.0%	61.10 ± 2.0%
48.0 ± 0.3	1176.41 ± 2.1%	57.17 ± 2.0%
46.6 ± 0.3	1016.74 ± 2.1%	54.88 ± 2.2%
45.1 ± 0.3	861.25 ± 2.3%	51.08 ± 2.2%
43.6 ± 0.3	629.96 ± 3.8%	39.11 ± 2.3%
42.1 ± 0.3	386.70 ± 6.6%	25.53 ± 4.4%
40.6 ± 0.3	170.06 ± 8.2%	12.40 ± 5.0%
38.8 ± 0.3		2.93 ± 3.0%
37.2 ± 0.4		1.81 ± 3.9%
35.5 ± 0.4		0.85 ± 6.8%

the reaction ^{181}Ta(α, n)^{184m,g}Re and ^{181}Ta(α, $2n$)^{183}Re are summarized and plotted as a function of α-particle bombarding energy. The experimental cross-sections are in millibarns and presented along with the percentage of statistical errors only. In table 3 and figure 2b the experimental results on the isomeric cross-section ratios for the isomer pair ^{184m,g}Re by the reaction ^{181}Ta(α, n)^{184m,g}Re are given as a function of α-particle bombarding energy. In table 4 the production cross-section as well as the isomeric cross-section ratios for the isomer pair ^{184m,g}Re by the reaction ^{185}Re(α, αn)^{184m,g}Re are presented as a function of α-particle bombarding energy. Since the isomeric cross-section ratios are measured for the first time, no comparison could be made. In table 5 and figures 3a–e the total residual production cross-section in mb for the reactions figure (3a) ^{197}Au(α, n)^{200}Tl, figure (3b) ^{197}Au(α, $2n$)^{199}Tl, figure (3c) ^{197}Au(α, $3n$)^{198m,g}Tl, figure (3d) ^{197}Au(α, $4n$)^{197}Tl and figure (3e) ^{197}Au(α, $p3n$)^{197m}Hg are summarized and plotted as a function of α-particle bombarding energy. The absolute errors which is generally $\cong$ 8% consists of uncertainties due to target foil thickness (±2%), the beam

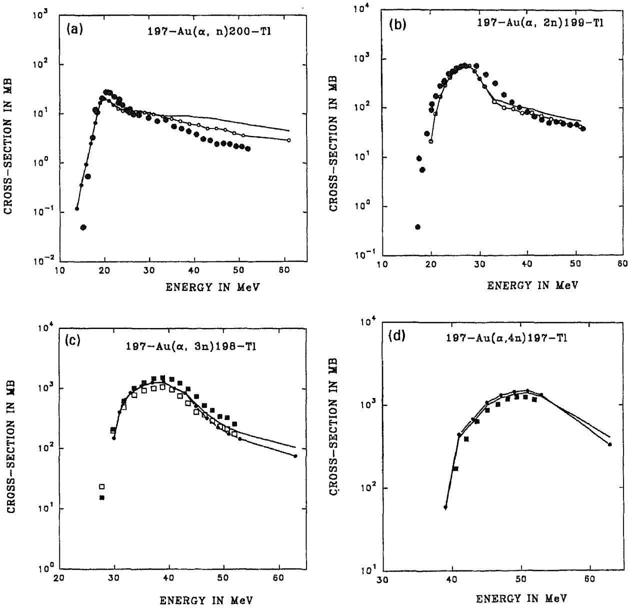

Figure 3(a–d).

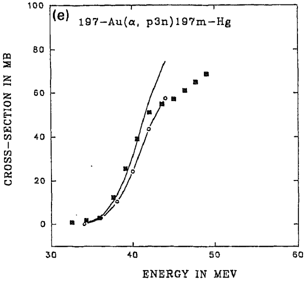

Figure 3a–e. The total residual production cross-section in mb for the reaction **(a)** ^{197}Au(α, n)^{200}Tl (•), **(b)** ^{197}Au(α, $2n$)^{199}Tl (•), **(c)** ^{197}Au(α, $3n$)^{198m,g}Tl (■ ⇒ m-state, □ ⇒ g-state), **(d)** ^{197}Au(α, $4n$)^{197}Tl (■) and **(e)** ^{197}Au(α, $p3n$)^{197m}Hg (■) for m-state) are plotted as a function of α-particle bombarding energy. Solid lines are the geometry dependent hybrid model and the -•- or -○- lines are the hybrid model fits using the code Alice/91 with $N_0 = 4, N_n = 2, N_p = 2$ and $N_h = 0$.

current integration ($\pm 2\%$), the detector efficiency ($\pm 5\%$) and the analysis of the γ-ray spectra (statistical uncertainty) generally ($\leq 2\%$). The uncertainties caused by the large size of the irradiation area and the non-uniformities of the target contribute about 5% to the average error of the cross-section. The uncertainty given for the energy values are those of target thickness only and beam energy resolution was $\cong \pm 200.0$ keV only.

4. Comparison with theoretical predictions

We have investigated the nuclear mechanism of the nuclear reaction induced by α-particles using the computer codes Alice/91 [17] and Stapre [18]. The Alice/91 code [17] describes the process of equilibrium evaporation of particles and γ-rays in terms of the Weisskopf and Ewing model [24] and pre-equilibrium reaction mechanism according to the hybrid and geometry dependent hybrid model [1, 2]. Whereas in the Stapre code [18], the evaporation of particles and γ-rays are treated in the framework of the statistical model with consideration of angular momentum and parity using Hauser–Feshbach formalism [25]. For emission of the first particle pre-equilibrium decay is also taken into account. The pre-equilibrium emission of the particles was treated in the Stapre code [18] in the framework of exciton model [3]. The high energy parts of the excitation functions are dominated by pre-equilibrium reaction mechanism whereas the low energy parts are dominated by evaporation with its characteristic peak.

Most of the nuclear reaction models [1–6, 26, 27] to treat the pre-equilibrium phase of reactions leading to the formation of a compound nucleus are semi-classical in nature and have been used with considerable success in describing experimental data pertaining to the equilibration process, mainly the forward peaked hard component observed in the continuous spectra of light ejectiles and the high energy tails seen in the excitation functions of activation cross-sections. However, most of these models employ one or both of the two basic concepts, the intranuclear cascade model [INC] [4, 5] and Griffin's statistical model of intermediate structure [3] (SMIS). The integral excitation functions of α-induced reactions have been discussed by several authors [7–10] considering models of the compound nucleus as well as pre-equilibrium reactions, as mentioned above. They conclude that the theory of pre-equilibrium reactions is helpful in explaining the mechanism of α-induced reactions. The hybrid model for pre-equilibrium reaction was proposed by Blann [1] which provides in some way a marriage between the simple SMIS model of Griffin [3] and the INC model using the more elaborate master equation approach due to Harp *et al* [4, 5]. However, there were some shortcomings in the hybrid model. It gives incorrect cross-sections and spectral distributions when applied to nucleon induced reactions at medium energies. Comparison with the INC model indicated that in the hybrid model, deficiencies resulted from the failure to take properly the enhanced emission from the nuclear surface. These deficiencies were partly rectified by reformulating the hybrid model as a sum of contributions, one term for each entrance channel impact parameter. In this way the diffuse surface properties sampled by the higher impact parameters were crudely incorporated into the precompound decay formalism in geometry dependent hybrid model (GDH) by Blann [2]. In the present work our excitation functions are calculated on the basis of hybrid model [1] and geometry dependent hybrid model [2] using the program Alice/91 [17] on the ND-500 and Super-32 computer at our centre.

The statistical part of the Alice/91 [17] can account for a large variety of reaction types. The evaporation of neutrons, protons and clusters such as deuteron and α-particles was considered [24]. The binding energies and Q-values used in the present code were based on experimental masses. The Alice/91 code [17] stores experimental masses in a 'data file. Whenever the nuclear masses are not tabulated, these were calculated from the Myers and Swiatecki mass formula [28], liquid drop masses with pairing. We have used the option in the default version of GDH whereby only the first collision is localized according to the impact parameter [29] with all the higher order precompound terms being treated by the hybrid model i.e. using nuclear densities averaged over the nucleus and independent of the impact parameter. This is reasonable because the excitons can sample nearly the entire nuclear volume after a single scattering since the mean free path (mfp) values are $\cong 4.74$ fm. The inverse cross-sections were calculated using the optical model subroutine of Alice/91 [17], where the optical model parameters were those of Becchetti and Greenlees [30]. The Fermi level density used is of the form

$$\rho(u) = (\sqrt{\pi}/12) \cdot (u - \delta)^{-5/4} \cdot a^{-1/4} \cdot \exp[2\sqrt{a(u - \delta)}],$$

where u is residual nucleus excitation, a is the level density parameter taken as $A/9\,\text{MeV}^{-1}$ which is the default option of the code and $\delta = 11/\sqrt{A}\,\text{MeV}$ the pairing energy shift, with either a backshifted or standard pairing shift option. We have used the standard option.

In the *a priori* formulation of the hybrid and geometry dependent hybrid model, the intra-nuclear transition rates are calculated either from the imaginary part of the optical model or from the free nucleon–nucleon scattering cross-section [31]. For particle energies exceeding 55 MeV the optical model parameters of Becchetti and Greenlees [30] used in the code are not applicable and thus at higher energies the calculation of the mean free path for intra-nuclear transitions should be calculated from nucleon–nucleon scattering cross-sections. Since our bombarding energy range was below 55 MeV, we have used only optical model option for calculating the intra-nuclear transition rates.

The Stapre code [18] has been used to calculate the theoretical cross-sections and isomeric cross-section ratios for α-induced reactions taking into account up to six sequential evaporation of particles and γ-rays. Each evaporation step is treated within the framework of the statistical model with consideration of angular momentum and parity using Hauser–Feshbach formalism [25]. For the emission of the first particle pre-equilibrium decay is also taken into account. Direct interactions were not considered.

The parameters used in the code Stapre [18] were generally accepted ones. For calculation of the transmission coefficients of various particles for the code Stapre [18], the default global set of optical model parameters of Alice/91 code [17] was used. The transmission coefficients for γ-rays with transition energy ε_γ are expressed by the γ-ray strength function $f_{\mathrm{XL}}(\varepsilon_\gamma)$ for the multipole radiation of type XL. For the E1 strength function, the Brink–Axel [32] model with global parameters was used and for M1, E2, M2, E3 and M3 radiations, the Weisskopf model [33] was used. For energies, spins and parities of the discrete levels of the residual nuclei, the lowest 15–20 levels in [22] were used. The level density formalism of the back-shifted Fermi gas model expressed by Lang [34] was used for the continuum excitation energy region. The level density parameter $a = A/9$ was used for all nuclei, where A is the mass number of the nucleus. The spin distribution of the level density was characterized by the effective moment of inertia Θ_{eff} or better by its ratio to rigid body moment of inertia Θ_{rig} $(\eta = \Theta_{\mathrm{eff}}/\Theta_{\mathrm{rig}})$. Since isomeric cross-section ratios are expected to depend strongly on the effective moment of inertia, all the calculations were performed for $\eta = 0.5$ and $\eta = 1.0$.

In the Stapre code the pre-equilibrium emission of the particles were treated in the framework of exciton model [3] having the following ingredients. For the initial exciton configurations (p_0h_0) we used $(4,0)$ for α-particles [17]. The transition rates were calculated by the formulae of Williams and Cline model [35]. The average residual two-body matrix element that appears in the transition rates λ_+, λ_0 and λ_- formulae as proposed by Kalbach–Cline [36] is expressed as

$$|M|^2 = FM \cdot A^{-3} \cdot E^{-1}, \tag{5}$$

where E is the excitation energy of the composite system. The quantity FM is a constant with the dimension of (MeV)^3 and generally treated as free parameter so as to get a good fit to the experimental data. The values used for the α-particle induced reactions were in the range $FM = 750\text{–}1000\,\mathrm{MeV}^3$.

In Alice [17] code, we have taken an initial exciton configuration $n_0 = 4$ $(n_n = 2, n_p = 2, n_h = 0)$ which is equivalent to a break-up of the incoming α-particle in the field of the nucleus and the nucleons occupying excited states above the Fermi energy gives a better description of the excitation function compared to other configurations for the α-particle bombarding energies up to 55.0 MeV. Therefore we have mostly used $n_0 = 4$ $(n_n = 2, n_p = 2, n_h = 0)$ configuration in most of our calculations. The total production cross-section in mb for the reactions in figure (1a) $^{193}\mathrm{Ir}(\alpha, 2n)^{195}\mathrm{Au}$ (■), figure (1b) $^{193}\mathrm{Ir}(\alpha, 3n)^{194}\mathrm{Au}$ (■), figure (1c) $^{(193),191}\mathrm{Ir}[\alpha, (4n)2n]^{193}\mathrm{Au}$ [(■), □] and figure (1d) $^{191}\mathrm{Ir}(\alpha, 3n)^{192}\mathrm{Au}$ (■) are plotted as a function of α-particle bombarding energy. The solid line is the geometry dependent hybrid model and the circle-line (–o–) is the hybrid model fits using the code Alice/91 with $N_0 = 4, N_n = 2, N_p = 2$ and $N_h = 0$. In figure 2a the total residual production cross-section in mb for the reaction $^{181}\mathrm{Ta}(\alpha, n)^{184m,g}\mathrm{Re}$ [symbols ■ ⇒ g, □ ⇒ m] are plotted as a function of α-particle bombarding energy. The solid line is the geometry dependent hybrid model fit using the code Alice/91 with $N_0 = 4, N_n = 2, N_p = 2$ and $N_h = 0$. The –•– and –○– lines are Stapre code calculations with $FM = 1000$ (MeV)^3 and $FM = 750$ (MeV)^3 respectively. In figure 2b and table 3 the isomeric cross-sections and their ratios are presented. The isomeric cross-section is practically constant at low bombarding energy with some tendency to increase at higher bombarding energy which means that at higher bombarding energy there is some tendency to populate the isomeric state preferentially. However, at very high excitation energy both the states are populated equally as seen in table 4 for the reactions $^{185}\mathrm{Re}(\alpha, \alpha n)^{184m,g}\mathrm{Re}$. In figure 2c the total residual production cross-sections in mb for the reaction $^{181}\mathrm{Ta}(\alpha, 2n)^{183}\mathrm{Re}$ [• symbols] are plotted as a function of α-particle bombarding energy. The solid line is the geometry dependent hybrid model fit using the code Alice/91 with $N_0 = 4, N_n = 2, N_p = 2$ and $N_h = 0$. In figures 3a–e the total residual production cross-section in mb for the reactions figure (3a) $^{197}\mathrm{Au}(\alpha, n)^{200}\mathrm{Tl}$ (•), figure (3b) $^{197}\mathrm{Au}(\alpha, 2n)^{199}\mathrm{Tl}$ (•), figure (3c) $^{197}\mathrm{Au}(\alpha, 3n)$ $^{198g,m}\mathrm{Tl}$ (■ ⇒ m-state and □ ⇒ g-state), figure (3d) $^{197}\mathrm{Au}(\alpha, 4n)^{197}\mathrm{Tl}$ (■) and figure (3e) $^{197}\mathrm{Au}(\alpha, p3n)$ $^{197m}\mathrm{Hg}$ (■ ⇒ m-state) are plotted as a function of α-particle bombarding energy. The solid lines are the geometry dependent hybrid model and the circle-dashed lines (–○–) are hybrid model fits using the code Alice/91 with $N_0 = 4, N_n = 2, N_p = 2$ and $N_h = 0$.

In the energy range of the measurement both geometry dependent hybrid model and hybrid model fit all the excitation functions reasonably well taking limitations of the calculations into account. Considering the multitudes of uncertainties in pre-equilibrium calculations such as (i) range of equilibrium and pre-equilibrium reaction cross-section involved and (ii) in parameters such as inverse reaction cross-sections and level densities etc. Blann [31] considered that a result which is within a factor of two (i.e. 0.5 to 2.0) of the experimental result in absolute cross-section and which generally has the correct spectral shape and variation of yield with excitation energy is an encouraging result.

5. Conclusion

A consistent set of 18 excitation functions has been measured for α-induced reactions on Ir, Au, Ta and Re targerts. The reliability of the cross-section was checked by comparing our measurements on Au with previous measurements. As in the previous studies, we have also observed that the excitation functions of the reactions induced by α-particles show structure with an initial peak with a slowly decreasing high energy edge becoming a flat plateau. The lower energy peak corresponds to particle emission mainly by evaporation by completely equilibrated compound nucleus. Whereas the low cross-section higher energy flat plateau corresponds to pre-equilibrium emission of nucleons at initial stages of the nuclear reaction. Comparison of the experimental data with hybrid and GDH model calculation shows reasonably good agreement with GDH model fitting high energy shoulder better indicating geometry dependent (surface) effects are important at higher energies only. Therefore, we can conclude that the dominant mechanism for reaction induced by α-particle in the lower energy range of these measurements is fusionevaporation and only at the higher energy the pre-equilibrium emission becomes dominant.

Acknowledgements

The author thanks the operational staff of the cyclotron at VECC, Calcutta for running the cyclotron smoothly during the experiments, and Super-32 computer system of our centre for their assistance at various stages of calculations. He also thanks Dr. M Blann for supplying the Alice/91 code and Dr M Uhl for supplying the Stapre code.

References

[1] M Blann, *Phys. Rev. Lett.* **27**, 337 (1971)
[2] M Blann, *Phys. Rev. Lett.* **28**, 757 (1972)
[3] J J Griffin, *Phys. Rev. Lett.* **17**, 478 (1966)
[4] D G Harp, J M Miller and J B Berne, *Phys. Rev.* **165**, 1166 (1968)
[5] G D Harp and J M Miller, *Phys. Rev.* **C3**, 1847 (1971)
[6] M Blann, *Annu. Rev. Nucl. Sci.* **25**, 123 (1975)
[7] S A Hjorth, H Ryde, K A Hagemann, G Lovhoiden and J C Waddington *Nucl. Phys.* **A144**, 513 (1970)
[8] M Ismail and A S Divatia, *Pramana – J. Phys.* **30**, 193 (1988); B.A.R.C./1366 (1987)
M Ismail, *Pramana – J. Phys.* **32**, 605 (1989) and B.A.R.C/1407 (1988)
[9] M Ismail, *Phys. Rev.* **C41**, 87 (1990)
[10] J Ernst, R Ibowski, H Klampil, H Machner, T Mayer-Kuckuk and R Shanz, *Z. Phys.* **A306**, 301 (1982)
[11] C Kaltach, *Phys. Rev.* **C23**, 124 (1981)
[12] M L Goldberger, *Phys. Rev.* **74**, 1268 (1948)
[13] C J Mathews, B G Glagola, R A Moyle and V E Voila Jr., *Phys. Rev.* **C25**, 2181 (1982)
[14] I Dostrovsky, Z Frankel and G Friedlander, *Phys. Rev.* **116**, 683 (1959); **118**, 781 (1960); **118**, 791 (1960)
[15] F Puhlhofer, *Nucl. Phys.* **A280**, 267 (1977)
[16] Y Nagame, K Sueki, S Baba and H Nakahara *Phys. Rev.* **C41**, 889 (1990)
O A Capurro, M de la Vega Vedoya, C Wasilevsky and S J Nassiff, *J. Radioanalytical Nucl. Chem.* **89/2**, 519 (1985)
A Colboreanu, P Constanin and O Salageon, *Nucl. Phys.* **A383**, 251 (1982)
F Hermes, E W Jasper, H E Kurz, T Mayer-Kuchuk, P F A Goudsmit and H Arnold, *Nucl. Phys.* **A228**, 175 (1974)
F M Lanzafame and M Blann, *Nucl. Phys.* **A142**, 545 (1970)
[17] M Blann, Alice/85/300 *A Evaporation Code*, Lawrence Livermore National Laboratory, University of California Livermore UCID-20169 (1985)
M Blann and H K Vonach, *Phys. Rev.* **C28**, 1475 (1983)
[18] M Uhl and B Stromaier, *Computer code for particle-induced activation cross-section and related quantities*, Institut fur Radiumforchung und Kernphysik Report 76/01, 1976 and Addendum to this report. See also B Stromaier and M Uhl, International Atomic Energy Agency Report IAEA-SMR **43**, 313 (1980)
[19] C F Williamson, J P Boujot and J Picard, CEA-R 3042 (1966)
[20] J Kern, *Isabelle: A fortran non-linear least-square fit code for nuclear spectra* (University of Fribourg, Switzerland, 1970) (unpublished)
[21] J Kern, *Nucl. Inst. Method.* **79**, 233 (1970)
[22] C M Lederer and V S Shirley, *Table of Isotopes*, 7th edition (New York, John Wiley, 1978)
[23] A H Wapstra and G Audi, *Nucl. Phys.* **A432**, 1 (1985)

[24] V F Weisskopf and D H Ewing, *Phys. Rev.* **57**, 472 (1940)

[25] W Hauser and H Feshbach, *Phys. Rev.* **87**, 336 (1952)

[26] E Gadioli, E Gadioli-Erba, L Sajo-Bohus and G Tagliaferri, *Rev. Nuovo Cimento* **6**, 1 (1976)

[27] E Gadioli, E Gadioli-Erba and J J Hogan, *Phys. Rev.* **C16**, 1404 (1977)

[28] W D Mayers and W J Swiatecki, *Nucl. Phys.* **81**, 1 (1966)
W D Mayers and W J Swiatecki, *Ark. Fys.* **36**, 343 (1967)

[29] M Blann and H K Vonach, *Phys. Rev.* **C28**, 1475 (1983)

[30] F D Becchetti and F D Greenlees, *Phys. Rev.* **182**, 1190 (1969)

[31] M Blann, *Nucl. Phys.* **A213**, 570 (1973)

[32] G A Bartholomew *et al, Adv. Nucl. Phys.* (Plenum Press, N.Y., 1973) vol. 7, ch. 4

[33] J M Blatt and V F Weisskopf, *Theoretical Nuclear Physics* (Wiley, New York, 1952) p. 627

[34] D W Lang, *Nucl. Phys.* **77**, 545 (1966)

[35] C K Cline, *Nucl. Phys.* **A195**, 353 (1972)

[36] C Kalbach-Cline, *Nucl. Phys.* **A210**, 590 (1973)

Jeans–Buneman instability in a dusty plasma

B P PANDEY and G S LAKHINA
Indian Institute of Geomagnetism, Dr. Nanabhai Moos Marg, Colaba, Mumbai 400 005, India
E-mail: pandey@iigm0.ernet.in; lakhina@iigm0.ernet.in

MS received 4 August 1997; revised 5 November 1997

Abstract. A self consistent formulation of the Jeans instability of a dusty plasma with proper inclusion of charge dynamics is described. It is shown that charge fluctuations significantly affect the Jeans as well as the Buneman mode. For plasma particles (electrons and ions) in local thermal equilibrium, the Jeans length λ_J is given by $\lambda_J \approx \lambda_g F(R, \epsilon, \beta/\eta)$, where λ_g is the Debye length of the charged grains, R is the square of the ratio of the Jeans to the plasma frequency of the grains, ϵ is the square of the ratio of the Debye length of the grains and the plasma particles and β/η is the ratio of the attachment to the decay frequency of the electronic charges to the grain surface. The functional form of F is given in the text. Numerical investigation of the Jeans–Buneman mode for a two and three component plasma shows that the Jeans mode dominates at $k\lambda_D \ll 1$ (where k is the wave number and λ_D is the Debye length of plasma particles), whereas at $k\lambda_D \gg 1$ only the Buneman mode operates. Charge fluctuations reduce the area of overlap of the two modes. Furthermore, in the absence of gravity, there exists a new, charge fluctuation induced unstable mode in a streaming dusty plasma. Astrophysical applications of the results are discussed.

Keywords. Jeans–Buneman instability; Jeans length; charge fluctuations.

PACS Nos 52.25; 52.35

1. Introduction

Dust grains are present everywhere in the universe. Dark haloes in galaxies [1], infrared emission from circumstellar shells of early as well as late type stars [2,3], spectral features of the emission from active galactic nuclei (AGN) [4], ring and spoke formation in planetary systems [5], structure of cometary tails [6], are all attributed to the presence of micron sized grains. Back on earth, grains are present in uncontrolled (e.g. in the earth's magnetosphere and ionosphere) as well as controlled (e.g. Tokamak plasmas, plasma arcs etc.) environments. The grains are generally composed of graphite, silicate and metallic compounds in cosmic environments. The size distribution of the grain has been investigated by comparing the observed interstellar extinction curve with the theoretical one. The observed extinction curve do not fit to a single size and single composition implying that the sizes, masses and electric charges of the grains vary in a wide range. For example, grain sizes may vary between macroscopic (few cm) and microscopic (10^{-8} cm) scales, masses vary between 10^{-5}–10^{-15} g and electronic charges between $(1 - 10^6)$. Charging of a grain takes place because of the radiative and plasma background in which it is immersed in most of the astrophysical situations. It is quite possible that the sizes and masses of the grains might depend on the same plasma environment, e.g. Coulombic coagulation [7] could lead to bigger and heavier grains while breaking of the massive grains due to Maxwellian stress could be the source of lighter and smaller grains. These charged grains couple with the plasma dynamics through electromagnetic (EM) forces. A dusty/grainy plasma is thus a three component plasma consisting of electrons, ions and charged grains.

Collective behaviour of a dusty plasma has been investigated in considerable detail in the recent past [5, 8–11]. As most of these studies pertain to fixed charge on the grain, waves and instabilities in such a plasma are not very different from that of three component ion-electron plasmas. It is through the inclusion of charge dynamics [12–19] or mass dynamics [20] that new collective features have emerged.

The gravito-electromagnetic coupling of an atomic plasma in local thermal equilibrium was studied in the context of star formation by Eddington [21]. He showed that self-gravity is unimportant for such a plasma as $R = \omega_{\mathrm{J}}^2/\omega_{\mathrm{pg}}^2 \sim 10^{-36}$, where $\omega_{\mathrm{J}} = (4\pi G n_{\mathrm{g}} m_{\mathrm{g}})^{1/2}$ is the Jeans frequency and $\omega_{\mathrm{pg}} = (4\pi n_{\mathrm{g}} Q^2/m_{\mathrm{g}})^{1/2}$ is the plasma frequency of the grain with G as the gravitational constant and $n_{\mathrm{g}}, m_{\mathrm{g}}$ and Q as the number density, mass and charge of the grain respectively. Therefore, the scales at which the two forces operate are widely separated. The formation of large scale structures have entirely been attributed to gravitational condensation of matter whereas the radiation processes are attributed to electromagnetic interactions of the plasma particles. However, for typically cm sized grains ($m_{\mathrm{g}} \sim 10^{-5}$ gm), $R \sim O(1)$ and thus the two scales may overlap. The broad spectrum of observed masses and charges [22, 23] suggests that the dynamics of a dusty plasma can be studied in any of the following regimes: (a) EM $\gg$ GF (gravitational force), (b) EM force $\sim$ GF and (c) EM force $\ll$ GF. The first case corresponds to the plasma processes like radiation, heating etc., the second case is thought to be the cause of Spoke formation in Saturn's ring, thickness of the Jovian rings etc., and the last case corresponds to the formation of stars, clusters etc. [24].

An important distinction should be pointed out between the $R \sim 1$ and $F_{\mathrm{grav}} \sim F_{\mathrm{Em}}$ (F_{grav} and F_{Em} are the gravitational and the electromagnetic force on the grains). Whereas $R \sim 1$ leads to unusual collective behaviour of a self-gravitating dusty plasma due to overlap of two scales, $F_{\mathrm{grav}} \sim F_{\mathrm{Em}}$ implies merely the balance of the two forces whose origin could be quite different. For example in the planetary rings, the self repulsion of the grain is balanced by the gravitational attraction of the planets for micron and submicron sized grains [25].

Recently, the Jeans instability of a dusty plasma has been studied by several authors [26–31]. Time dependent nonlinear solutions of a self-gravitating three component dusty plasma showed [27] that when self-gravity is annuled by the electric polarization of a collapsing plasma i.e., $R \sim 1$, plasma may become gravitationally unstable due to the properties of the background plasma. Therefore, merely balancing the self attraction of the grains with self repulsion is not sufficient for determining the fate of condensation. Avinash and Shukla [29] studied the Jeans instability of a dusty plasma with the inclusion of ion dynamics and found enhanced gravitational condensation of the grains. Later, Pandey and Dwivedi [30] showed that the proper inclusion of ion dynamics does not destabilize the Jeans mode any further but the collapse of the grain follows the same dynamics as the collapse of the neutral matter under gravity. This is attributed to the fact that ions are responding at the free fall time scale of the grains and as a result they shield

All the previous studies, with the exception of the last one, exclude charge dynamics from consideration. However, the grain charge is a dynamical variable and in the present work we investigate the Jeans instability with proper charge dynamics of the grains. We consider an infinite, homogeneous, unmagnetized, nonrotating plasma and, invoking 'Jeans swindle', ignore the zeroth order gravitational field. However, as has been demonstrated [27], the construction of a proper equilibrium does not change the plasma dispersion relation, as one can always consider homogeneity in a limiting sense. We first consider the dusty plasma with electrons and ions in local thermal equilibrium and find that in the presence of charge fluctuations, the Jeans length gets modified, implying that the charge dynamics has a bearing on the gravitational collapse of the matter.

Next, we consider the gravitational instability of a two component dusty plasma with streaming ions. We find that when charge fluctuations are absent, a new gravito-streaming mode may give rise to the accretion of matter, when self gravity is annulled by the thermal pressure and self repulsion of the grain. Inclusion of charge fluctuations modifies both gravitational as well as streaming modes. Also, a new charge fluctuation induced instability in the presence of streaming ions exists in such a plasma. However, the growth rate of this new mode is much smaller than that of the Buneman mode.

Lastly, the dynamics of a three component dusty plasma is analysed. In the presence of streaming ions, the picture is similar to the previous case i.e., the Jeans and the Buneman modes dominate in two different windows with a small overlap of the two. The streaming instability sets in at a smaller wavelength in the presence of charge fluctuation than in the absence of it. The growth rate of the Jeans mode is enhanced in the presence of charge dynamics of the grains. Also, a charge fluctuation induced instability exists in such a plasma with a growth rate much smaller than that of the Buneman mode.

The paper is organized in the following fashion. In §2, basic equations are given and the equilibrium is discussed. Section 3 describes the linearized equations and gives the general dispersion relation. Also, a special case of the dispersion relation is discussed when electrons and ions are in local thermal equilibrium. Section 4 describes the Jeans–Buneman mode for two and three component dusty plasma systems. In §5 a summary of the results is given and possible applications to interstellar media are indicated.

2. Basic equation

A three component dusty plasma consisting of electrons, ions and charged dust grains, is assumed to have grains of equal radius and carrying identical charge due to the collisional attachment of the electrons and ions to the grain surface. Effects of the photoemission, secondary emission etc. is ignored in the present study. It should be mentioned here that this assumption is not entirely satisfactory for the thermal grains. The charging and the discharging of the grain give rise to sink and source terms in the continuity and momentum exchange equations. Owing to the large mass difference between the plasma and the grains, we assume that the gravitational potential is determined mainly equations:

Continuity equations:

$$\frac{\partial n_\alpha}{\partial t} + \nabla\cdot(n_\alpha \mathbf{v}_\alpha) = -\beta_\alpha(n_\alpha - n_{\alpha 0}), \tag{1}$$

$$\frac{\partial n_{\mathrm{g}}}{\partial t} + \nabla\cdot(n_{\mathrm{g}} \mathbf{v}_{\mathrm{g}}) = 0, \tag{2}$$

where $\alpha = e, i$; g = grain. The subscript 0 means equilibrium quantities and $\beta_\alpha = I_\alpha n_{\mathrm{g}}/q_\alpha n_\alpha$ is the attachment frequency of the plasma particles to the grains.

Equations of motion:

$$m_\alpha n_\alpha \frac{\mathrm{d}\mathbf{v}_\alpha}{\mathrm{d}t} = -T_\alpha \nabla n_\alpha - q_\alpha n_\alpha \nabla\phi - m_\alpha n_\alpha \nabla\psi - m_\alpha n_\alpha \beta_\alpha(\mathbf{v}_\alpha - \mathbf{v}_{\mathrm{g}}), \tag{3}$$

$$m_{\mathrm{g}} n_{\mathrm{g}} \frac{\mathrm{d}\mathbf{v}_{\mathrm{g}}}{\mathrm{d}t} = -T_{\mathrm{g}} \nabla n_{\mathrm{g}} - Q n_{\mathrm{g}} \nabla\phi - m_{\mathrm{g}} n_{\mathrm{g}} \nabla\psi. \tag{4}$$

Charge equation:

$$\frac{\mathrm{d}Q}{\mathrm{d}t} = I_e(Q,\phi) + I_i(Q,\phi), \tag{5}$$

where the currents are given by [32, 33]

$$I_e = -\pi a^2 e \sqrt{\frac{8T_e}{\pi m_e}} n_e \exp\left[\frac{e(\phi_{\mathrm{g}} - \phi)}{T_e}\right], \tag{6}$$

$$I_i = \pi a^2 e \sqrt{\frac{8T_i}{\pi m_i}} n_i \left[1 - \frac{e(\phi_{\mathrm{g}} - \phi)}{T_i}\right] \tag{7}$$

and the two Poisson's equation are

$$\nabla^2\phi = 4\pi e[n_e - n_i] - 4\pi Q n_{\mathrm{g}}, \tag{8}$$

$$\nabla^2\psi = 4\pi G n_{\mathrm{g}} m_{\mathrm{g}}, \tag{9}$$

where $\mathrm{d}/\mathrm{d}t = \partial/\partial t + \mathbf{v}\cdot\nabla$ and m, n, v, T, ϕ, ψ denote the mass, number density, velocity, temperature, electrostatic and gravitational potential respectively. The quantity $\phi_{\mathrm{g}} - \phi$ is the potential difference between the grain surface potential and the background plasma potential so that the unperturbed charge Q_0 is given by $Q_0 = C(\phi_{\mathrm{g}} - \phi)$ where C is the capacitance of the grain and is given by [34], $C = a\exp(-a/\lambda_{\mathrm{D}})$ with a as the radius of the grain. The exponential factor reflects the screening of the grain charge by the plasma particles. In equilibrium, electron and ion currents equal each other and thus the grain is at the 'floating potential'. Note that for $n_{e0}/n_{i0} \approx 1$ (a situation relevant to most of the planetary system [10] and interstellar media [9]), $\beta_e = \beta_i$ i.e., electrons and ions get attached to the grain at the same rate after the initial build up of a negative charge on the grain similar to the behaviour of plasma particles near the sheath [35]. The above set of equations (1)–(9) form the basic set of equations for the linear analysis.

and gravitational potential. Whereas the neglect of zeroth order electrostatic potential is guaranteed by the existence of opposite charges, there is no such thing as opposite mass and thus, there is no way to make the gravitational potential disappear in zeroth order. Therefore, the problem of a self gravitating system is in general an eigenvalue problem. However, important physical insight can be gained by invoking 'Jeans Swindle' i.e ignoring the zeroth order potential field of gravity. To reiterate, we consider the linear gravitational instability of an infinite, homogeneous plasma characterized by

$$n_{e0} = n_{i0} + Zn_{\mathrm{g}0}, \quad \psi_0 = \phi_0 = 0, \quad \mathbf{v}_{i0} = V_0\hat{x}, \quad \mathbf{v}_{e0} = \mathbf{v}_{\mathrm{g}0} = 0,$$

where V_0 is the ion streaming velocity and $Z = Q/e$. The linearized set of equations are

$$\frac{\partial n_{\alpha 1}}{\partial t} + \nabla\cdot(n_{\alpha 1}\mathbf{v}_0 + n_{\alpha 0}\mathbf{v}_{\alpha 1}) = -\beta_{\alpha 0}n_{\alpha 1}, \tag{10}$$

$$\frac{\partial n_{\mathrm{g}1}}{\partial t} + n_{\mathrm{g}0}\nabla\cdot\mathbf{v}_{\mathrm{g}1} = 0, \tag{11}$$

where the subscript 1 means perturbed quantities.

$$\begin{aligned} n_{\alpha 0}\left(\frac{\partial \mathbf{v}_{\alpha 1}}{\partial t} + \mathbf{v}_{\alpha 0}\cdot\nabla\mathbf{v}_{\alpha 1}\right) &= -C_\alpha^2\nabla n_{\alpha 1} - \frac{q_\alpha n_{\alpha 0}}{m_\alpha}\nabla\phi_1 - n_{\alpha 0}\nabla\psi_1 \\ &- \beta_{\alpha 0}n_{\alpha 0}(\mathbf{v}_{\alpha 1} - \mathbf{v}_{\mathrm{g}1}) - \beta_{\alpha 1}n_{\alpha 0}\mathbf{v}_{\alpha 0} - \beta_{\alpha 0}n_{\alpha 1}\mathbf{v}_{\alpha 0}, \end{aligned} \tag{12}$$

$$\frac{\partial \mathbf{v}_{\mathrm{g}1}}{\partial t} = -C_{\mathrm{g}}^2\frac{\nabla n_{\mathrm{g}1}}{n_{\mathrm{g}0}} - \frac{Q_0}{m_{\mathrm{g}}}\nabla\phi_1 - \nabla\psi_1, \tag{13}$$

$$\frac{\partial Q_1}{\partial t} + \eta Q_1 = |I_{e0}|\left(\frac{n_{i1}}{n_{i0}} - \frac{n_{e1}}{n_{e0}}\right), \tag{14}$$

where $\eta = (e|I_{e0}|/C)(1/T_e + 1/w_0)$, $w_0 = T_i - e\phi_{f0}$ with T_i as the ion temperature and ϕ_{f0} as the equilibrium floating potential of the grains and $C_\alpha = (T_\alpha/m_\alpha)^{1/2}$ is the thermal velocity of the αth species and $\beta_{\alpha 1}$ is obtained from the definition of β_α by perturbing it around $\beta_{\alpha 0}$. Taking the spatial and temporal dependence of all perturbed quantities as $\exp[-i(\omega t - kx)]$, we get the following relation between fluctuation density and potentials:

$$[\omega^2 + \omega_{\mathrm{J}}^2 - k^2C_{\mathrm{g}}^2]\left(\frac{n_{\mathrm{g}1}}{n_{\mathrm{g}0}}\right) = -k^2\phi_1\left(\frac{Q}{m_{\mathrm{g}}}\right), \tag{15}$$

$$[(\omega + i\beta_e)^2 - k^2C_e^2]\frac{n_{e1}}{n_{e0}} = -k^2\phi_1\left[\left(\frac{e}{m_e}\right) + \frac{\omega_{\mathrm{J}}^2 - i\beta_e\omega}{\omega^2 + \omega_{\mathrm{J}}^2 - k^2C_{\mathrm{g}}^2}\left(\frac{Q}{m_{\mathrm{g}}}\right)\right] \tag{16}$$

and

$$\begin{aligned} &\left[(\bar{\omega} + i\beta_i)^2 - k^2C_i^2 + i\beta_i kV_0 + \chi\beta_i^2\frac{n_i}{Zn_{\mathrm{g}}}\left(\frac{kV_0}{\omega + i\eta}\right)\right]\frac{n_{i1}}{n_{i0}} = k^2\phi_1 \\ &\times\left[\left(\frac{e}{m_i}\right) - \frac{\omega_{\mathrm{J}}^2 - i\beta_i\bar{\omega}}{\omega^2 + \omega_{\mathrm{J}}^2 - k^2C_{\mathrm{g}}^2}\left(\frac{Q}{m_{\mathrm{g}}}\right) - \chi\beta_i^2\frac{n_i}{Zn_{\mathrm{g}}}\left(\frac{kV_0}{\omega + i\eta}\right)\frac{\left[\left(\frac{e}{m_e}\right) + \frac{\omega_{\mathrm{J}}^2 - i\beta_e\omega}{\omega^2 + \omega_{\mathrm{J}}^2 - k^2C_{\mathrm{g}}^2}\left(\frac{Q}{m_{\mathrm{g}}}\right)\right]}{(\omega + i\beta_e)^2 - k^2C_e^2}\right], \end{aligned} \tag{17}$$

where use has been made of $\beta_{i1} = \beta_i((n_{g1}/n_{g0}) - \chi(Q_1/Q))$, $\beta_{e1} = \beta_e((n_{g1}/n_{g0}) + \chi(Q_1/Q))$ with $\chi = 1/((T_i/e\phi_{f0}) - 1)$ [14]. Then plugging equations (15)–(17) in the Poisson's equation leads to the following dispersion relation:

$$1 = \left(1 + \frac{i\beta_e}{\omega + i\eta}\right)A + \left(1 + \frac{i\beta_i}{\omega + i\eta}\right)B + \frac{\omega_{pg}^2}{\omega^2 + \omega_J^2 - k^2C_g^2}, \tag{18}$$

where

$$A = \frac{\omega_{pe}^2 + \frac{n_e}{Zn_g}\frac{\omega_{pg}^2}{\omega^2+\omega_J^2-k^2C_g^2}\left[\omega_J^2 - i\beta_e\omega\right]}{(\omega + i\beta_e)^2 - k^2C_e^2}, \tag{19}$$

$$B = \frac{\omega_{pi}^2 - \frac{n_i}{Zn_g}\frac{\omega_{pg}^2}{\omega^2+\omega_J^2-k^2C_g^2}\left[\omega_J^2 + i\beta_i\bar{\omega}\right] - \chi\beta_i^2\frac{n_i}{Zn_g}\left(\frac{kV_0}{\omega+i\eta}\right)\left[\delta\omega_{pe}^2 + \frac{n_i}{Zn_g}\frac{\omega_{pg}^2}{\omega^2+\omega_J^2-k^2C_g^2}\left(\omega_J^2 - i\beta_e\omega\right)\right]}{\left[(\bar{\omega} + i\beta_i)^2 - k^2C_i^2 + i\beta_i kV_0 + \chi\beta_i^2\frac{n_i}{Zn_g}\left(\frac{kV_0}{\omega+i\eta}\right)\right]}, \tag{20}$$

where $\bar{\omega} = \omega - kV_0$ is the Dopler shifted frequency, $\omega_{p\alpha}^2 = 4\pi n_\alpha {q_\alpha}^2/m_\alpha$ is the plasma frequency of the αth species and $\delta = n_{e0}/n_{i0}$. Subscript 0 has been dropped from the equilibrium quantities. The above dispersion relation in the limit $\omega_{pg} \to 0$, $k\lambda_e \ll 1$, reduces to equation (18) of Bhatt and Pandey [14]. First we analyse the gravitational instability of a dusty plasma when the plasma particles are in thermal equilibrium. For this case the thermal response of the plasma particles is much faster than the grain's response to the perturbations i.e., $kC_g \ll \omega \ll kC_i \le kC_e$ where k is the wave number. Assuming $\beta_e = \beta_i = \beta$ we get the following dispersion relation:

$$\omega^2 = \frac{k^2\lambda_D^2\omega_{pg}^2}{1 + k^2\lambda_D^2 + \frac{i\beta}{\omega+i\eta}} - \omega_J^2 + k^2C_g^2, \tag{21}$$

where $\lambda_D = \lambda_e\lambda_i/[\lambda_e^2 + \lambda_i^2]^{1/2}$ is the effective plasma Debye length with $\lambda_{e,i} = (T_{e,i}/4\pi n_{e,i}e^2)^{1/2}$. The dispersion relation (21) coincides with that of Mohanta *et al* [31] in the absence of an external magnetic field for a cold dust grain. Before undertaking a complete numerical analysis of the above dispersion relation, the effect of the charge fluctuation can be studied by solving equation (21) perturbatively by treating $\eta \sim \beta < \omega$. Then the interesting root is

$$\frac{\omega}{\omega_{pg}} = i\left[R - \left(k^2\lambda_g^2 + \frac{k^2\lambda_D^2}{1 + k^2\lambda_D^2}\right)\right]^{1/2} + \frac{i\beta}{2}\frac{k^2\lambda_D^2}{(1 + k^2\lambda_D^2)^2}\frac{1}{\left[R - \left(k^2\lambda_g^2 + \frac{k^2\lambda_D^2}{1+k^2\lambda_D^2}\right)\right]}, \tag{22}$$

where $\lambda_g^2 = T_g/4\pi n_g Q_0^2$ is the Debye length of the grains. From the above expression it is clear that the attachment of the grains causes enhancement of the gravitational condensation for some $0 < k < k_J$, where k_J is the Jeans wave number at which the right hand side of equation (21) goes to zero in the absence of charge fluctuations, i.e., $\beta = 0$. As the wave number crosses the Jeans wave number, the first term in equation (22)

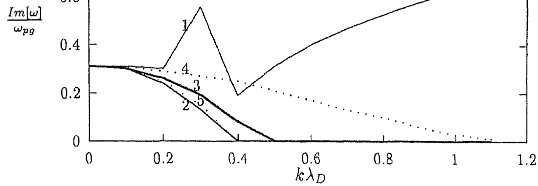

Figure 1. Curve 1 corresponds to the perturbative solution for $\beta/\eta \sim 1$ and $x2 = \beta/\omega_{pg} = 0.1$. Curves 2, 3, 4 and 5 shows the Jeans mode for $x1 = \eta/\omega_{pg} = 0$, $x2 = 0$; $x1 = 0.1$, $x2 = 0.1$ and $x1 = 0.1$, $x2 = 1$ and $x1 = 1$, $x2 = 0.1$ respectively. Here $\epsilon = 10^{-6}$, $R = 0.1$.

becomes real and thus it describes the usual dust acoustic wave [36]. Around $k = k_J$ the perturbative analysis breaks down (see curve 1 of figure 1; the parameters for which the plot is drawn are given below). Qualitatively one can explain these features as follows: Charge fluctuations damp the dust acoustic waves. The rate of damping is maximum at certain values of k and reduces to zero for both higher and lower k values. This will cause the shift in the balance of force in favour of gravity for some range of k. As a result, gravitational instability becomes robust and the Jeans length reduces compared to the fixed charge case.

Next, we analyse equation (21) numerically. We solve equation (21) for $\epsilon = \lambda_g^2/\lambda_D^2 = 10^{-6}, \eta/\omega_{pg} = (0 - 0.1)$ and $\beta/\omega_{pg} \sim (0 - 1), R = 0.1$, numbers representative of the interstellar medium [10]. From figure 1 (curves 2 and 3) we see that in the absence of charge fluctuation, the growth rate goes to zero at smaller $k\lambda_D$ than in the presence of charge fluctuation, implying that the condensation of the grain is facilitated by charge fluctuations. An increase in the attachment frequency ($\beta \gg \eta$) leads to the enhancement of the growth rate (figure 1, curve 4), since attachment of the plasma particles favourably reduces the repulsive potential well of the grain, facilitating the condensation. Similarly, an increase in η implies that more plasma particles are seen in the vicinity of a collapsing grain, repelling the incoming grain in the process (curve 5). Thus, the growth rate decreases. With the increase of R the growth rate will increase, as it is the measure of relative strength of the attraction to the repulsion.

Finally we calculate the Jeans length from equation (21). Jeans length is the critical length at which the instability vanishes. Then solving equation (21) for the marginal stability condition, we get

$$\lambda_J = \lambda_g F\left(R, \epsilon, \frac{\beta}{\eta}\right) \tag{23}$$

and

$$F\left(R,\epsilon,\frac{\beta}{\eta}\right)=\left[\frac{2}{-\epsilon\left(1+\frac{\beta}{\eta}\right)+(R-1)+\left(\left(\epsilon\left(1+\frac{\beta}{\eta}\right)-(R-1)\right)^{2}+4\epsilon R\left(1+\frac{\beta}{\eta}\right)\right)^{1/2}}\right]^{1/2}, \tag{24}$$

where $\epsilon=\lambda_{\mathrm{g}}^{2}/\lambda_{\mathrm{D}}^{2}$. For $R\sim 1$,

$$F\left(R,\epsilon,\frac{\beta}{\eta}\right)\approx\begin{cases}1 & \epsilon\sim 1\\ \left[\frac{1}{\epsilon\left(1+\frac{\beta}{\eta}\right)}\right]^{1/4} & \epsilon\ll 1.\end{cases} \tag{25}$$

From the above limiting expression for F it is clear that when $\epsilon\sim 1$, grain charge fluctuation plays no role in the gravitational collapse and $\lambda_{\mathrm{J}}=\lambda_{\mathrm{g}}$. Therefore, the gravitational condensation of the grain can be halted only by the repulsive electrostatic field for a fixed charge. However when $\epsilon\ll 1$ Jeans length is considerably modified by the charge dynamics of the grain. Depending upon the value of β/η the Jeans length can decrease or increase. For $\epsilon=0.1$ we see from figure 2 that $\lambda_{\mathrm{J}}/\lambda_{\mathrm{g}}$ initially decreases (in comparison with the value of $\lambda_{\mathrm{J}}/\lambda_{\mathrm{g}}$ in the absence of charge fluctuations) and then after $\beta/\eta=5.5$ it shoots up. Therefore, for grainy plasma whose Debye length is much smaller than the Debye length of the plasma particle, charge fluctuations can facilitate or oppose the collapse of the grain by setting up the electrostatic field in phase or out of phase with the gravitational field. Above limiting cases can be applicable to different regions in interplanetary and interstellar media. For example, it is known that dark molecular clouds (DMC) contain grains of different charges depending upon the ambient plasma temperature [37]. If the ambient temperature is between 0–10 K then the grain may have

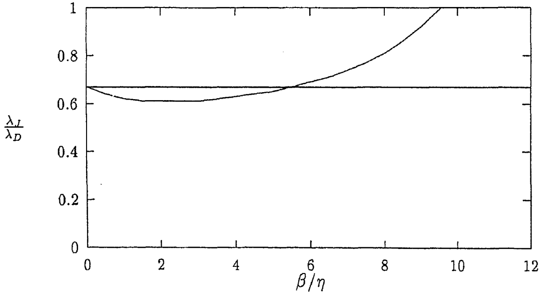

Figure 2. Normalized Jeans length is plotted against β/η for $\epsilon=0.1$ and $R=1$. The horizontal curve is the value of normalized Jeans length in the absence of charge fluctuation.

$-1, -1$ charge whereas for temperature around 100 K a grain may have 10 electronic rges. As ϵ may become $O(1)$ in DMC [9] the first of the two cases may be relevent. above analysis indicates that for grains charge flip-flopping between $-1, 0, +1$, i.e., η or for grains containing 10 or more charges $\beta > \eta$, the charge fluctuation is of no sequence to the gravitational condensation of the grains. In a planetary environment 1 and typically $Q \sim (10^3 - 10^6)e$ [5, 10]. Then the charge fluctuations can cause ease as well as increase in the Jeans length. As a result charge fluctuations can litate or inhibit the condensation of the grains depending on the value of β/η. refore we see that for $\lambda_g \ll \lambda_D$ gravitational condensation of the grain can be facilid or halted by an electrostatic field much beyond the length suggested by the analysis andey *et al* [27]; Pandey and Dwivedi [30] for a fixed charge. The preliminary nature he above results must be noted as they have been carried out for very idealized ations. For a final application of these results to relevant physical problems (viz. star nation, formation of the planetary system etc.), a model calculation must be done.

Jeans–Buneman mode

t, we shall consider a two component dusty plasma with streaming ions. This is an l situation where all the electrons are attached to the grains. This type of plasma may t in some of the regions of dense interstellar clouds, where Zn_g may become nparable to n_i [38]. Dynamics of such a plasma has been considered [39] in the context tearing instability in the Saturnian rings. Then the dispersion relation equation (18) ices to

$$\left[1 - \frac{\omega_{pg}^2}{\omega^2 + \omega_J^2 - k^2C_g^2}\right] D = \left[1 + \frac{i\beta_i}{\omega + i\eta}\right]\left[\omega_{pi}^2 - \frac{\omega_J^2\omega_{pg}^2}{\omega^2 + \omega_J^2 - k^2C_g^2} - \frac{i\beta_i\bar{\omega}\omega_{pg}^2}{\omega^2 + \omega_J^2 - k^2C_g^2}\right], \tag{26}$$

ere

$$D = [(\bar{\omega}^2 + 2i\beta_i\bar{\omega}) - k^2C_i^2 - i\beta_i kV_0].$$

ore numerically solving the above 5th order polynomial, we analyse equation (26) in absence of charge fluctuations. Then the dispersion relation becomes

$$[\omega^2 + \omega_J^2 - k^2C_g^2 - \omega_{pg}^2][(\bar{\omega}^2 - k^2C_i^2 - \omega_{pi}^2)] = \omega_{pg}^2(\omega_{pi}^2 - \omega_J^2), \tag{27}$$

in the absence of gravity we have the usual Buneman mode [40]. Here we look for a de in the vicinity of $kV_0 \approx (k^2C_i^2 + \omega_{pi}^2)^{1/2}$ in the presence of gravity. The unstable ns–Buneman root is

$$\omega \approx \left(\frac{1 + i(3)^{1/2}}{2}\right)\left(\frac{\omega_J^2\omega_{pi}}{2}\right)^{1/3} \tag{28}$$

vided $\omega_J^2 \approx \omega_{pg}^2$. The significance of this mode underlies the fact that even when self action is completely annulled by self repulsion, the Jeans–Buneman mode may trigger

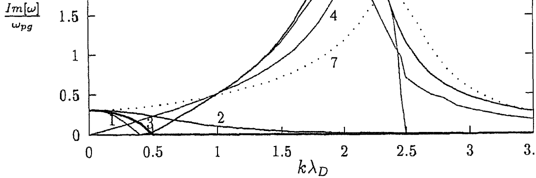

Figure 3. Curves 1, 2 and 3 are the Jeans mode with $x1 = 0, x2 = 0$; $x1 = 0, x2 = 1$ and $x1 = 1, x2 = 1$ respectively for $R = 0.1$. Curves 4, 5 and 6 shows Buneman mode for $\alpha = V_0/C_i = 1.1$, $\epsilon = 10^{-4}$, $R = 0$ with $x1 = 0$, $x2 = 0$; $x1 = 0$, $x2 = 1$ and $x1 = 1, x2 = 1$ respectively and curve 7 shows the Jeans–Buneman mode for $x1 = 1$, $x2 = 1$ with $R = 0.1$, $\alpha = 1.1$.

off a large scale condensation of the grains. The growth rate is given by

$$\Gamma \sim 2.10^{-5}\left[\frac{m_g n_g n_i^{1/2}}{m_i^{1/2}}\right]^{1/3} \quad \text{Hz}, \tag{29}$$

where, n, m are measured in cgs units. The importance of the above mode can be gauged from the following example. It is known that the self-gravitating clouds of masses $10^2 - 10^6 M_\odot$, where $M_\odot$ is the solar mass, contain many dark cores with number densities in excess of $10^4\,\text{cm}^{-3}$ and masses $\leq 10^2 M_0$ [9]. In these dark cores, nearly one per cent of the mass is in dust form. In such cores, typically $n_g \approx 4 \times 10^{-12}(a/10^{-5})n_H$ which for hydrogen density n_H ranging between $(10^3\,\text{cm}^{-3} - 10^7\,\text{cm}^{-3})$ and cm sized grain becomes $(1\,\text{cm}^{-3} - 10^{-4}\,\text{cm}^{-3})$. Calculating ion density from $n_i/n_H \sim 10^{-8}$ $(n_H/10^5\,\text{cm}^{-3})^{-1/2}$, we get $n_i \sim (10^{-2}\,\text{cm}^{-3} - 10^{-4})\,\text{cm}^{-3}$. Assuming ions to be ionized hydrogen we get $\Gamma \sim 10^{-3}$. Thus we see that the Jeans–Buneman mode may play an important role in the formation of large scale structures.

Next, we solve the dispersion relation (26) numerically. We see from figure 3 that at large scale lengths only the Jeans mode operates, whereas at small scale lengths the Buneman mode is excited. There is an overlap of the two modes. The growth rate of the Jeans mode is smaller than that of the streaming mode. Charge fluctuations affect both gravitational and Buneman modes. In the presence of charge fluctuation, the growth rate of the Jeans mode increases and drops to zero at large $k\lambda_D$. The Buneman mode, on the other hand, starts operating at much shorter wavelengths in the presence of charge fluctuations. The area of overlap of the Jeans and Buneman modes shrinks in the presence of charge dynamics. At $k\lambda_D \ll 1$ the gravitational instability dominates over the streaming instability. In the other limit, i.e., $k\lambda_D \gg 1$, it is the streaming instability which destabilizes the grain plasma system. In the very narrow window $k\lambda_D \sim O(1)$, the two

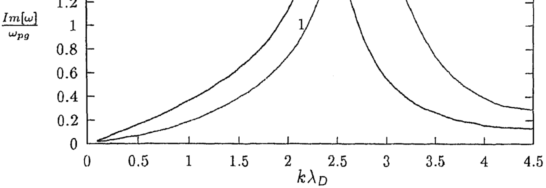

Figure 4. Curves 1, 2 show the charge fluctuation induced unstable mode for $R = 0$, $\alpha = 1.1, \epsilon = 10^{-6}$ with $x1 = 0, x2 = 1$ and $x1 = 1, x2 = 1$ respectively.

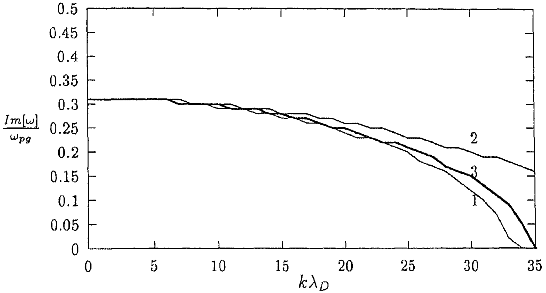

Figure 5. Curves 1, 2 and 3 shows Jeans mode for a three component plasma with $x1 = 0$, $x2 = 0$; $x1 = 0$, $x2 = 1$ and $x1 = 1$, $x2 = 1$ respectively for $R = 0.1$. Here $\epsilon = 10^{-6}$, $\delta = 0.01$, $n_i/Zn_g = 0.99$, $\lambda_i^2/\lambda_e^2 = 10^{-4}$, $\omega_{pe}^2/\omega_{pg}^2 = 10^3$, $\omega_{pi}^2/\omega_{pg}^2 = 10^2$.

les overlap. In the absence of gravity, in addition to the Buneman mode, we find a charge fluctuation induced unstable mode existing in a streaming plasma as shown in re 4. The growth rate of this mode is smaller than that of the Buneman mode. This le appears analogous to the negative energy mode reported earlier by Jana *et al* [13]. sically as $\alpha = V_0/C_i > 1$, the ion wave can be viewed as a negative energy wave n the ion frame, so that dissipative effects associated with nonstreaming grains can rise to its amplification.

lext, we study the stability of a three component plasma. We solve the dispersion tion (18) numerically for Boltzmannian as well as non-Boltzmannian electrons. The usion of electron dynamics does not affect the result significantly and the change in

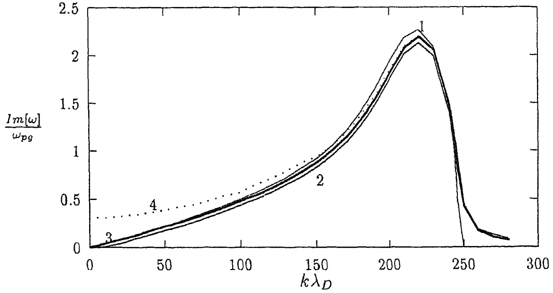

Figure 6. Curves 1, 2 and 3 shows the Buneman mode for $R = 0$ with $x1 = 0, x2 = 0$; $x1 = 0, x2 = 1$ and $x1 = 1, x2 = 1$ respectively. Here $\epsilon = 10^{-6}$, $\delta = 0.01$, $n_i/Zn_g = 0.99$, $\chi = 10^{-6}$, $\lambda_i^2/\lambda_e^2 = 10^{-4}$, $\omega_{pe}^2/\omega_{pg}^2 = 10^3$, $\omega_{pi}^2/\omega_{pg}^2 = 10^2$. Curve 4 depicts Jeans–Buneman mode for $R = 0.1$, $\alpha = 1.1$.

the result is only 1%. In the parameter regime studied by us, last term in the numerator of equation (18) is unimportant. However, there exists the parameter window in which contribution of this term is comparable with the first two terms of the numerator.

In figure 5 we plot the Jeans mode with and without charge fluctuations. As is evident from the figure, the modification due to charge fluctuations in the Jeans mode for a three component plasma is similar to a two component plasma. Figure 6 depicts the Buneman mode and also the Jeans–Buneman mode. The qualitative features are similar to the previous mode. We find that charge fluctuation in the presence of streaming ions also gives rise to negative energy mode. The behaviour of this mode is similar to that described in figure 4 for a two component plasma. We mention here that this result is at variance with the result of Bhatt and Pandey [14] who found perturbatively that the parameter regime for negative energy mode shrinks to zero in a three component plasma when $\delta \approx 1$.

5. Conclusion

We have analysed the Jeans instability of a dusty plasma self consistently by properly considering the charge dynamics. It has been shown that charge fluctuations cause a modification of the Jeans length. The charge fluctuation can facilitate or hinder the condensation of the grains depending upon the value of β/η. Implication of this result on Spoke formation in the Saturn's ring or on the thickness of the Jovian rings may be profound. For example, as the charge fluctuations modifiy the Jeans mode, the lifetime of self-levitation may be finite before the grains finally succumb to their self-gravity. In the absence of charge fluctuations the levitated grains will forever be hanging above the ring plane of the planets. In the interstellar media, even highly charged grains (e.g. $\sim 100e$ in the HII region) will undergo an enhanced condensation due to the dynamic nature of the grain charge. Therefore, our analysis indicates that charge fluctuations might help the gravitational condensation of the charged grains in different cosmic environment.

ınalysis of two and three component dusty plasma do not qualitatively show different aviour. The Buneman and the Jeans modes both act in quite distinct zone with a very row overlap region in the presence of charge fluctuations. For a two component plasma, find an analytical expression for the Jeans–Buneman mode. The growth rate of aming instability is always higher than the Jeans instability. Therefore, the existence of ixed Jeans–Buneman mode will cause faster condensation of the grainy plasma than purely gravitational instability. A new charge fluctuation induced unstable mode is nd from the numerical solution of the dispersion relation. It might be possible that when Buneman mode saturates, the charge fluctuation induced mode will be of significance.

ased on the above analysis one can draw a general picture of the collapse of plasma ter. It might be possible that the collapse of the plasma matter may undergo several ges: Far away from the gravitating centre, gravitational attraction may trigger off a apse. The collapse may continue up to a certain scale length (say) L_1 at which stage sma particles (namely ions) may develop a considerable flow ($\alpha > 1$) which results in enhancement of the collapse rate. In the final stage which will be reached after a ain scale length $L, L \ll L_1$ streaming ions go on accreting to the grains solely due to r flow. Thus, very close to the gravitating centre, its a purely Buneman mode which litates the condensation of the matter.

t is known that massive objects surrounded by a charged plasma cloud (e.g. HII ion) will tend to accrete matter. The resultant flow of the plasma can be of importance stars in close binary systems [32], for compact objects (white dwarfs, neutron stars, ck hole etc.) which have been proposed as the possible energy source for the radiation ning out from a very localized region of the sky [41]. The accretion rate is calculated ely by the gravitational field. However, as one sees from the above analysis, the retion rate will become a function of the scale length. Very close to the gravitating tre the Jeans mode might be superseded by a Buneman mode and one gets an anced growth rate. The presence of a stellar wind in the interstellar medium supports h a picture. However, our analysis is for a very simplified model and thus the results suggestive rather than compelling.

ꓥs a variety of plasmas is found in interstellar media, we believe that our results have ring on star formation, cluster formation etc. Charge fluctuations affect the densation of the grains and thus, it might be possible that the rate of star formation the galaxies are different than the presently predicted rates. Further work in this ection is required.

knowledgement

s work was supported by the Department of Science and Technology, Government of ia through the SERC scheme.

ferences

] E R Wollman, *Astrophys. J.* **392**, 80 (1992)
] V B Il'in and N V Voschennikov, *Astron. Rep.* **37**, 362 (1993)
] B G Anandrao, S R Pottasch and D B Vaidya, *Astron. Astrophys.* **273**, 570 (1993)

[4] H Netzer, *Active Galactic Nuclei*, Saas-Fee Advanced course 20, Lecture Note 1990, Swiss Society for Astrophysics and Astronomy edited by T J-L Courvoisier and M Mayor (Springer-Verlag, Berlin)
[5] C K Goertz, *Rev. Geophys.* **27**, 271 (1989)
[6] O Havnes, *Astron. Astrophys.* **193**, 309 (1988)
[7] M Horyani and C K Goertz, *Astrophys. J.* **361**, 155 (1989)
[8] U de Angelis, *Phys. Scr.* **45**, 465 (1992)
[9] T W Hartquist, O Havnes and G E Morfill, *Fund. Cosmic Plasma* **15**, 167 (1992)
[10] D A Mendis and M Rosenberg, *Ann. Rev. Astron. Astrophys.* **32**, 419 (1994)
[11] F Verheest, *Space Sci. Rev.* (1996) (in press)
[12] R K Varma, P K Shukla and V Krishan, *Phys. Rev.* **E50**, 1422 (1994)
[13] M R Jana, P K Kaw and A Sen, *Phys. Rev.* **E48**, 3930 (1994)
[14] J R Bhatt and B P Pandey, *Phys. Rev.* **E50**, 3980 (1994)
[15] S V Vladmirov, *Phys. Plasmas* **1**, 2762 (1994); *Phys. Rev.* **E50**, 1422 (1994)
[16] F Verheest, *Planet. Space Sci.* **42**, 883 (1994)
[17] R V Reddy, G S Lakhina, F Verheest and P Meuris, *Planet Space Sci.* **44**, 129 (1996)
[18] C B Dwivedi and B P Pandey, *Phys. Plasmas* **2**, 4134 (1995)
[19] F Verheest and P Meuris, *Phys. Lett.* **A198**, 228 (1995)
[20] B P Pandey and C B Dwivedi, *Pramana – J. Phys.* **45**, 255 (1995)
[21] A S Eddington, *Internal Constitution of the Stars* (Cambridge University Press, Cambridge, England, 1926)
[22] T Mukai, *Evolution of interstellar dust and related topics* in Proceedinge of the International School of Physica "Enrico Fermi", Course CI, Verenna, 1986 edited by A Bonetti, J M Greenberg and S Aiellu (North Holland, Amsterdam, 1989) p. 357
[23] S Barbash and R Lundin, *IEEE Trans. Plasma Sci.* **22**, 173 (1994)
[24] J Binney and S Tremaine, *Galactic Dynamics* (Princeton University Press, Princeton, NJ, 1988)
[25] H Alfven and A D Mendis, *Adv. Space Res.* **3**, 95 (1983)
[26] G Gisler, Q R Ahmad and E R Wollman, *IEEE Trans. Plasma Sci.* **20**, 922 (1992)
[27] B P Pandey, K Avinash and C B Dwivedi, *Phys. Rev.* **E49**, 5599 (1994)
[28] R Chhajalani and A Parihar, *Astrophys. J.* **422**, 746 (1994)
[29] K Avinash and P K Shukla, *Phys. Lett.* **A189**, 470 (1994)
[30] B P Pandey and C B Dwivedi, *J. Plasma Phys.* **55**, 395 (1996)
[31] L Mohanta, B J Saikia, B P Pandey and S Bujarbarua, *J. Plasma Phys.* **55**, 401 (1996)
[32] L Spitzer, *Physical Processes in the Interstellar Medium* (John Wiley, New York, 1978)
[33] B T Draine and E E Salpeter, *Astrophys. J.* **15**, 77 (1979)
[34] E C Whipple, T G Northrop and D A Mendis, *J. Geophys. Res.* **90**, 7405 (1985)
[35] V E Golant, A P Zhilinsky and I E Shakharov, *Fundamentals of Plasma Physics* (John Wiley, New York, 1980)
[36] F Melandso, T Aslaksen and O Havnes, *J. Geophys. Res.* **98**, 13315 (1993)
[37] B G Elmgreen, *Astrophys. J.* **232**, 729 (1979)
[38] T Umebayashi and T Nakano, *Publ. Astron. Soc. Jpn.* **32**, 405 (1980)
[39] H L F Houpis and D A Mendis, *The Moon and Planets* **29**, 39 (1983)
[40] O Buneman, *Phys. Rev.* **115**, 503 (1959)
[41] J Frank, A R King and D J Raine, *Accretion power in astrophysics* (Cambridge University Press, Cambridge, 1985)

Regd. No. KRN-A 64

Pramana journal of physics Vol. 50 (No. 2), February 1998

Contents

Relativistic fluid sphere on pseudo-spheroidal space-time . . . . *Ramesh Tikekar and V O Thomas* 95

Causal dissipation in Robertson–Walker cosmological models . . . . *J P Singh, A Prasad and R K Tiwari* 105

Particle production in curved space-time . . . . *N G Sarkar and S Biswas* 109

Finite temperature Cornwall–Jackiw–Tomboulis formalism of Φ^6 theory . . . . . *K P Satheesh and K Babu Joseph* 133

Spin observables of the NN interaction in a relativistic harmonic model with confined gluons and mesons . . . . *K B Vijayakumar and S B Khadkikar* 149

Ratio of the color suppressed decays $\Lambda_b \to \Lambda J/\psi$ and $B^0 \to KJ/\psi$ . . . . *A K Giri and R Mohanta* 155

Triviality bound on lightest Higgs mass in next to minimal supersymmetric model . . . . *S R Choudhury, Mamta and Sukanta Dutta* 163

Measurement and analysis of the excitation function and isomeric cross section ratios for α-induced reaction on Ir, Au, Re and Ta nuclei . . . . *M Ismail* 173

Jeans–Buneman instability in a dusty plasma . . . . *B P Pandey and G S Lakhina* 191

Indexed in CURRENT CONTENTS ISSN 0304–4289

Edited and published by N Mukunda for the Indian Academy of Sciences, Bangalore 560 080.
Typeset and printed at Thomson Press (I) Ltd., Faridabad 121 007.